# MODELING AND CONTROL OF HIGH SPEED MACHINE TOOL FEED DRIVES

by

CHINEDUM OKWUDIRE

B.Sc. (Mechanical Engineering)

Middle East Technical University, Turkey

M.A.Sc. (Mechanical Engineering)

University of British Columbia, Canada

A THESIS SUBMITTED IN PARTIAL FULFILLMENT OF

THE REQUIREMENTS FOR THE DEGREE OF

DOCTOR OF PHILOSOPHY

in

THE FACULTY OF GRADUATE STUDIES

(Mechanical Engineering)

THE UNIVERSITY OF BRITISH COLUMBIA

(Vancouver)

August 2009

# Abstract

Aerospace, die and mold, and automotive industries machine parts at high cutting speeds to reduce production cycle periods. Machine tools which carry out the cutting operations rely on either precision ball screw or linear motor direct drives to accurately position the workpiece relative to the cutting tool. However, the precise positioning capability of the drives is limited by low servo bandwidth and poor disturbance rejection resulting from structural flexibilities in ball screw drives as well as weak dynamic stiffness/robustness in direct drives.

This thesis proposes modeling, parameter identification, control and online parameter estimation techniques which aim at increasing the servo bandwidth and disturbance rejection ability of high speed machine tool feed drives.

A hybrid finite element methodology is used to model the structural dynamics of ball screw drives. As part of the model, two stiffness matrices are developed for connecting the finite element representation of the ball screw to the lumped-mass representation of the nut. The developed model is used to analyze the coupled axial-torsional-lateral vibration behavior of a critical structural mode that limits high bandwidth control of ball screw drives. Moreover, a method for accurately identifying the mass, damping and stiffness matrices representing the open-loop dynamics of ball screw drives is developed. The identified matrices are used to design gain-scheduled sliding mode controllers, combined with minimum tracking error filters, to effectively suppress the critical axial-torsional-lateral mode of ball screw drives thereby achieving high bandwidth control and good disturbance rejection.

For direct-driven machines, a high bandwidth disturbance adaptive sliding mode controller is designed to improve the dynamic stiffness of the drive, compared to similar controller designs, without increasing the controller's complexity. Furthermore, the cutting forces applied to the drive are estimated accurately using a disturbance recovery algorithm and used to improve the dynamic stiffness of low-frequency structural modes of direct-driven machine tools.

Finally, a method for estimating the changing mass of the workpiece during machining operations with cutting forces that are periodic at spindle frequency is introduced.

The techniques presented in this thesis are verified through simulations and/or experiments on single-axis ball screw and linear motor feed drives.

# Table of Contents

# List of Tables

# List of Figures

# Nomenclature

## Symbols

| | |
|---|---|
| $\mathbf{A}$ | State transition matrix |
| $a$ | Element of state transition matrix |
| $\mathbf{B}$ | Input matrix |
| $B_r$ | Equivalent viscous damping of a rigid body |
| $b$ | Element of input matrix; viscous damping of a rigid body |
| $\mathbf{C}$ | Damping matrix |
| $CS$ | Coordinate system |
| $c$ | Damping constant; $y$-intercept of a straight line |
| $d$ | diameter |
| $E$ | Young's modulus of elasticity |
| $\mathbf{e}$ | State tracking error vector |
| $e$ | error |
| $\mathbf{F}$ | Force vector |
| $F$ | Force applied to a point |
| $f$ | Frequency in Hertz |
| $\mathbf{G}$ | Transfer function matrix |
| $G$ | Transfer function; shear modulus of elasticity |
| $\bar{G}$ | Constant in MTEF transfer function |
| $g_1$, $g_2$ | Disturbance adaptation gains |
| $H$ | Height |

| | |
|---|---|
| $\bar{H}$ | Constant in MTEF transfer function |
| $\mathbf{I}$ | Identity matrix |
| $I$ | Moment of inertia |
| $i, j$ | Index counters |
| $J$ | Polar moment of inertia |
| $\bar{J}$ | Constant in MTEF transfer function |
| $\mathbf{K}$ | Stiffness matrix |
| $K$ | Feedback gain |
| $K_p$, $K_v$ | Feedback gains in cascaded controller |
| $k$ | Stiffness of a mechanical component; index counter for time steps |
| $k^s$ | Cross section factor for the Timoshenko beam element |
| $L$ | Length |
| $L_{ij}$ | Constants in MCDADSC error dynamics |
| $\mathbf{M}$ | Mass matrix |
| $M$ | Moment about an axis |
| $M_r$ | Equivalent mass of a rigid-body |
| $m$ | Mass; slope of a straight line |
| $N$ | Number, in terms of counts, of a parameter; constant in MCDADSC error dynamics; shape function of Timoshenko beam element |
| $n$ | Integer |
| $P$ | Point on a body |
| $p$ | Pitch of ball screw; dummy variable; pole of MTEF |
| $Q$ | Constant in sliding surface dynamics |

| | |
|---|---|
| $R$ | Constant in sliding surface dynamics; pitch radius of ball screw; complex modal constant |
| Rot(.) | Rotational operator |
| $\mathbf{r}$ | Position vector from the origin of a CS to a specific location |
| $r$ | Scalar position from the origin of a CS to a specific location; ratio in MTEF design; constant in disturbance transfer function |
| $r^*$ | Special ratio in MTEF design |
| $r_g$ | Gear ratio of ball screw |
| S(.) | Operator which converts a vector to its tensorial form |
| $s$ | Sliding surface; Laplace operator |
| $\mathbf{T}$ | Transformation matrix |
| $T$ | Sampling period (time) |
| $T_i$ | Integration time constant in cascaded controller |
| $\mathbf{U}$ | Mode shape matrix |
| $\mathbf{u}$ | Vector of translational displacements |
| $u$ | Translational displacement |
| $V$ | Volume |
| $v$ | Cumulative geometric error in table position measurements; velocity of table |
| $\mathbf{W}$ | Weighting matrix |
| $W$ | Weighting constant or function; windowing function |
| $X$ | Position of table referenced from a fixed point |
| $\mathbf{x}$ | Vector of displacements |
| $x$ | Displacement; $x$-axis of a CS |

| | |
|---|---|
| $y$ | $y$-axis of a CS |
| $\mathbf{z}$ | State vector |
| $z$ | $z$-axis of a CS; element of state vector; Z-transform operator |
| $\alpha$ | Pitch angle of ball screw; gain in MTEF; real part of complex modal constant |
| $\beta$ | Thread angle of ball screw; imaginary part of complex modal constant |
| $\Delta$ | Dynamics due to parametric uncertainty; uncertainty in parameter |
| $\varepsilon$ | Small positive number |
| $\mathbf{\Phi}$ | Regressor matrix in least-squares parameter estimation |
| $\Phi$ | Constant in Timoshenko beam element formulations |
| $\phi$ | Azimuth angle about ball screw's axis |
| $\mathbf{\Gamma}$ | Vector in least-squares parameter estimation |
| $\Gamma$ | Gain in MCDADSC dynamics |
| $\gamma$ | Gain in MCDADSC dynamics |
| $\kappa$ | Binary switching function in Shape Function-based screw-nut interface stiffness matrix derivation |
| $\lambda$ | Constant in sliding surface dynamics; eigenvalues of sliding surface and disturbance adaptation dynamics |
| $\mathbf{\Theta}$ | Parameter vector in least-squares estimation |
| $\boldsymbol{\theta}$ | Vector of rotational displacements |
| $\theta$ | Rotational/angular displacements; constant in MTEF |
| $\Sigma$ | Forcing function in MCDADSC error dynamics |
| $\sigma$ | Constant in MTEF |
| $\tau$ | Torque applied to motor shaft |

| | |
|---|---|
| $\omega$ | Frequency in [rad/s] |
| $\omega_n$ | Natural frequency in [rad/s] |
| $\xi$ | Non-dimensional distance measured in beam element formulations |
| $\Psi$ | Parameter in MTEF dynamics |
| $\zeta$ | Damping ratio |
| $'$ | Indicates a constant with uncertainty included or a modified constant |
| $\hat{}$ | Indicates an estimated signal |
| $\tilde{}$ | Indicates the error in an estimated signal |

**Subscripts**

| | |
|---|---|
| *Ax* | Indicates a parameter pertaining to the axial direction |
| *avg* | Indicates an averaged parameter |
| *Ball* | Indicates a parameter pertaining to the screw-nut interface balls |
| *BM* | Indicates a parameter pertaining to the Blackman window |
| *BS* | Indicates a parameter pertaining to the ball screw |
| *COM* | Indicates a parameter pertaining to the center of mass |
| *comp* | Indicates a parameter for compensation |
| *d* | Indicates a parameter pertaining to a disturbance |
| *dc* | Indicates a parameter pertaining to the dc component of a signal |
| *dR* | Indicates a parameter pertaining to disturbance recovery |
| *Elm* | Indicates a parameter pertaining to a beam element |
| *end* | Indicates an ending position |
| *e*, *eq* | Indicates the equivalent value of a parameter |

| | |
|---|---|
| *f* | Indicates a parameter pertaining to friction |
| *fft* | Indicates a parameter pertaining to FFT |
| *i*, *j*, *k* | Index counters |
| *L* | Indicates the *L*-configuration or left end of a beam element |
| *M* | Indicates the middle of a beam element |
| *m* | Indicates a parameter pertaining to a machine tool or motor |
| *N*, *Nut* | Indicates a parameter pertaining to the nut |
| *Node* | Indicates a parameter pertaining to a node of a finite element |
| *n* | Indicates a normalized parameter |
| *P* | Indicates a parameter pertaining to a point or the primary sliding surface |
| *p* | Indicates a parameter pertaining to the pitch of a ball screw |
| *R* | Indicates the right end of a beam element or the region of a beam element |
| *r* | Indicates a parameter pertaining to rigid body dynamics or the root of ball screw threads |
| *S* | Indicates a parameter pertaining to the secondary sliding surface or the eigenvalues of the sliding surface |
| *SN* | Indicates a parameter pertaining to the screw-nut interface |
| *sp* | Indicates a parameter pertaining to the spindle |
| *st* | Indicates a starting position |
| *t* | Indicates a parameter pertaining to the table |
| *tcp* | Indicates a parameter pertaining to the TCP |
| *thr* | Indicates a parameter pertaining to the ball screw threads |
| *U* | Indicates the *U*-configuration |
| *v* | Indicates a parameter pertaining to velocity |

| | |
|---|---|
| $x$ | Indicates a parameter pertaining to displacement |
| $x$, $y$, $z$ | Indicates a parameter pertaining to the $x$, $y$ and $z$ directions, respectively |
| $\Delta$ | Indicates a parametric uncertainty |
| $\xi$ | Indicates a parameter pertaining to a location $\xi$ within a beam element |

**Acronyms**

| | |
|---|---|
| ASMC | Adaptive sliding mode controller |
| CAD | Computer-aided design |
| CC | Cascaded controller |
| CNC | Computer numerically controlled |
| COM | Center of mass |
| CS | Coordinate system |
| DADSC | Disturbance adaptive discrete-time sliding mode controller |
| DOF | Degree-of-freedom |
| DR | Disturbance recovery |
| FE | Finite element |
| FEM | Finite element method |
| FFT | Fast Fourier transform |
| FRF | Frequency response function |
| LPV | Linear parameter varying |
| MCDADSC | Mode-compensating DADSC |
| MIMO | Multi input-multi output |
| MTEF | Minimum tracking error filter |

| | |
|---|---|
| NMP | Non-minimum phase |
| OL | Open-loop |
| OLTF | Open-loop transfer function |
| PD | Proportional-Derivative |
| PI | Proportional-Integral |
| PID | Proportional-Integral-Derivative |
| SISO | Single input-single output |
| SMC | Sliding mode controller |
| TCP | Tool center point |
| TF | Transfer function |

# Acknowledgements

I have deeply enjoyed my Ph.D. journey. “How?” you may wonder. I shall attempt to explain:

How many students have a research supervisor who is renowned worldwide but takes the time to express genuine care for each of his students? How many have a supervisor who immediately sees a colleague in them and gives his best to make them the best they can be? How many have supervisors who encourage them to value integrity and honesty in research as well as in day to day activities of life? I do hope there are many, but am so grateful to have such a supervisor in Dr. Altintas.

How many can boast of working in lab filled with top-notch, dedicated and hardworking individuals? How many of those could say that their lab mates are warm, friendly, open and always willing to help? I can definitely say that about the folks at the Manufacturing Automation Laboratory; and I am grateful for who they have become to me.

How many started their degree program having virtually no friend or acquaintance in town? Of those, how many can say that they have had some of their deepest and most meaningful friendships during the course of their studies? So has been my experience and I truly appreciate each of these friends.

How many Ph.D. students have family, who even though are many miles away, feel like they live a few blocks down the road? How many have a mum who herself recently obtained a Ph.D. degree and so fully empathizes with the highs and lows of the journey? How many have siblings who are very accomplished in their own right yet extremely down to earth individuals and wonderful friends? I don’t think I am the only one, but I am so grateful for my wonderful family.

How many have a beautiful, caring and loving wife to come home to every evening? How many can call her their best friend? How many have the coolest in-laws and feel so close to and loved by them? I am not going to guess how many, but I love my wife dearly and appreciate her family so much.

How many have a 10 month old boy who is always eager to welcome them home from school? How many are amazed at how he thinks he is so smart that he insists on typing strange “corrections” into his dad’s Ph.D. thesis? How many have my little “Ziggy”? I know the answer: None.

How many have come know the Almighty as a wonderful Father? How many have grown to love Him dearly and have derived strength from Him in the ups and downs of their Ph.D. journey? How many have Him as a sure hope even when the future is unknown? I pray there are many and I am glad to be in the number.

I have deeply enjoyed my Ph.D. journey – I think that is mildly put.

Dedicated to the loving memory of my dad,

Barrister Gabriel Onyenachim Okwudire (1948-2008),

whose sincere faith in God, passion for life, generous heart and

deep appreciation for excellence have truly inspired me.

# Chapter 1

## Introduction

With the advent of high speed machining, the performance demands placed on machine tools from end users like the die and mold, automotive and aerospace industries have increased tremendously over the years. On one hand, the aerospace industry requires high speed machine tools that enable complex parts to be produced in one piece within the shortest possible time. On the other hand, the die and mold industry demands machine tools that can cut complex 3-D shapes with speed, accuracy and high-quality surface finishes. Similarly, automotive manufacturers need high-precision machines that can perform point-to-point cutting operations in the shortest time possible.

In response to these demands, machine tool manufacturers have pushed the limits of high speed machine tools to a point beyond which these desirable, but otherwise unattainable, goals can be reached. This has come as a result of advances in various areas of machine tool engineering. For instance, the utilization of tooling materials such as carbide, ceramic, polycrystalline diamond, and cubic boron nitride has significantly increased achievable metal removal rates. Likewise, the use of ceramic balls in spindle bearing systems has increased the attainable speeds of machine tool spindles to values exceeding 40,000 [rpm].

To complement the advances in these other areas of machine tool technology, machine tool feed drives have to be capable of achieving high feed rates (over 50 [m/min]) and accelerations exceeding 1 [g] while aiming to attain sub-micron positioning accuracy. Such high performance positioning requirements in turn demand high bandwidth (greater than 100 [Hz]) and good disturbance rejection from closed-loop feed drive controllers. Typically, two types of feed drive design are resorted to in high speed machine tools − indirect or ball screw drives, and direct drives based on linear motor technology.

Ball screw drives provide thrust and linear motion at the machine tool table by transmitting power from a rotary motor through a ball screw mechanism. They are commonly used in machine tools because of their relatively high stiffness to cutting force disturbances and low sensitivity to variations in workpiece inertia as a result of their inherent gear reduction ratio. To be able to meet the speed and accuracy requirements of high speed machine tools, moving parts of ball screw drives are made lighter while furnishing them with high-bandwidth actuators, high-resolution feedback devices and low-friction roller or hydrostatic guideways.

The problem, however, with such high speed ball screw drives is that lightening them may lead to loss of stiffness in some parts of the mechanical structure (particularly the ball screw shaft), while low friction in the guideways reduces the amount of damping in the system. At the same time, higher feed rates and, in particular, higher accelerations lead to a proportional increase in the amount of inertial reactions borne by the drives. These factors put together result in an increase in the oscillatory excitations of the structural components of the drive, thereby making high speed ball screw drives structurally flexible as opposed to being rigid. Moreover, the properties of some of the vibration modes change as the table travels along the ball screw, and also as material is removed from the workpiece during machining operations. The vibration modes of the ball screw are also exposed to dynamic cutting forces which further excite them. These various elements combine to make structural flexibility a major bottleneck in achieving high bandwidth and good disturbance rejection in ball screw-driven machine tools.

The situation is slightly different for direct-driven machine tools. Direct drives supply linear motion and thrust directly to the machine tool table without any need of an intermediary conversion mechanism. Therefore, they have an advantage over ball screw drives because they involve fewer components and are thus less susceptible to the influence of undesirable structural modes. In addition, they can achieve higher speeds and accelerations with minimal backlash and friction, and they have unlimited travel range. Direct drives, however, have some significant drawbacks. The absence of gear reduction between the linear motor and table in direct drives makes them very sensitive to changes in workpiece mass. Furthermore, their dynamic stiffness depends mainly on the controller settings; it has little re-enforcement from the mechanical structure. As a result, the large forces that occur during machining could easily excite the dynamics of the control loop and cause instability in both the controller and the metal cutting process. In order to mitigate the effects of cutting forces and workpiece mass variations on the control of direct-driven machines, they are typically oversized by increasing the mass of the table and the power of the linear motors. This in turn reduces the achievable bandwidth and increases the cost of direct-driven machine tools, both of which are undesirable.

This thesis tackles the aforementioned challenges encountered in controlling high speed machine tool feed drives by proposing modeling, parameter identification/estimation and control techniques that address the specific and mutual problems of ball screw drives and direct drives. It achieves this goal as follows: First, a review of related literature is presented in Chapter Two, thereby providing a backdrop based on the work of other researchers to evaluate the methods put forward in the subsequent chapters. Chapter Three then introduces a finite element model that is used to gain profound insight into the structural behavior of flexible ball screw drives so that controllers that exploit the physical capabilities of the drives can be designed. Furthermore, a method for accurately identifying the structural dynamics information needed for controller design is put forward in the same chapter. In Chapter Four, a mode-compensating controller is designed to actively suppress the most critical resonance mode of ball screw drives, thereby achieving high bandwidth and good disturbance rejection. Chapter Five then moves on to direct drives where a controller is designed to enhance the dynamic stiffness of the control loop against cutting force disturbances. Moreover, the dynamic stiffness of direct-driven machines as a whole is further improved by proposing a method for accurately estimating low-frequency cutting forces and using them to cancel out vibrations between the tool and workpiece. Following this, the influence of changes in workpiece mass on both ball screw and direct drives is investigated in Chapter Six, and a new method for estimating the mass of the workpiece during periodic cutting operations is advanced. In the final chapter, concluding remarks and future research directions are discussed, while supplementary pieces of information pertinent to the content of this thesis are detailed in the ensuing bibliography and appendices.

# Chapter 2

## Literature Review

### 2.1 Overview

This chapter is devoted to reviewing some of the work done by other researchers, which bear relevance to the topics addressed in this thesis. Section 2.2 reviews past research in the area of modeling and identification of ball screw feed drives, including their structural flexibility, while Section 2.3 covers research related to controller design for ball screw drives with structural flexibility. Work done on high bandwidth control and dynamic stiffness enhancement of direct-driven machine tools is presented in Section 2.4, followed by an exploration of research related to online mass identification for high speed feed drives in Section 2.5. A summary of the contents of this chapter is presented in Section 2.5.

### 2.2 Modeling and Identification of Dynamics of Flexible Ball Screw Drives

#### 2.2.1 Modeling

Over the years, a lot of research effort has been put into modeling of ball screw drives including their structural flexibility. Flexible ball screw drive models published in literature range from fairly simple ones consisting of lumped masses connected by springs to more complicated ones entirely built using finite element methods (FEM).

As an example of one of the simpler models, Chen et al [14] represented a ball screw drive using rigid bodies connected by springs. Their model considered the axial and torsional deformations of the ball screw as well as the pitch motion of the table due to the guideway joint. Using their model, they highlighted the important role of guideway deformations in the positioning accuracy of the table. Similar models have been proposed by Kim and Chung [44], Lee et al [46], Poignet et al [60], and Yang and Lin [86].

Van Brussel et al [76] employed FEM to model a three-axis milling machine, including its ball screw drive, resulting in a large model having thousands of degrees of freedom (DOF). Using component mode reduction procedures in two steps, the original finite element model was reduced to a state-space model suitable for control design and simulation. A similar approach was taken by Schafers et al [67] who also created a full FEM model of a milling machine and used it to demonstrate the need for a mechatronics approach for the design and control of high speed machine tools.

There are merits and demerits of the lumped parameter and full FEM (i.e. distributed parameter) approaches to modeling flexible ball screw drives. The lumped parameter models are usually much simpler than the full FEM models because they involve fewer DOF and less redundant information. However, unlike the full FEM models, lumped parameter models are incapable of capturing the variation in drive dynamics as the table moves along the ball screw.

With a view to combining the merits of the aforementioned two methods of modeling flexible ball screw drives, numerous researchers have resorted to hybrid methods which consider the distributed stiffness and inertia of the ball screw while modeling other components of the drive as lumped masses connected by springs. One such approach has been put forward by Pislaru et al [59]. In their model, the distributed-parameter representation of the ball screw consists of a bunch of masses/inertias and springs which correspond to various sections of the ball screw shaft. However, such models cannot capture the changing dynamics of the feed drive system as the nut moves along the ball screw, because the values of the ball screw's parameters are apparently obtained for only one position of the nut. Varanasi and Nayfeh [79] overcome this shortcoming by modeling the ball screw using a uniform beam. The resulting infinite-dimensional model of the ball screw drive system is reduced to a low-order model using a Galerkin's procedure based on shape functions derived from the quasi-static deformation of the system. Their model shows a good prediction of the open-loop transfer function of the drive when compared to experimental results. A similar approach has also been adopted by Whalley et al [84]. As an alternative to using analytical beam formulations, most researchers prefer to employ a hybrid strategy whereby the ball screw is modeled using beam finite elements (e.g. [1][10][29][39][70][88][90]) because it is simpler, more practical and more versatile than using beam equations.

The interface between the ball screw and nut plays an important role in the transmission of motion, vibrations and forces from the ball screw to the table. For this reason, a lot of research effort has been invested into understanding the dynamics of the screw-nut interface ([21][22][50][82]). When modeling ball screw drives using FEM, the screw-nut interface is modeled as a special stiffness matrix which connects the ball screw to the nut. In deriving this special screw-nut interface matrix, most of the researchers mentioned above ([1][10][29] [39][70][79][84]) have considered only the axial and/or torsional deformations of the ballscrew. Zaeh et al [88] go a step further to include the effects of the ball screw's lateral deformations through 3-D transformations of the stiffness of each individual ball. However, their method falls short of determining some cross-coupling terms between deformations in the axial, torsional and lateral directions of the ball screw and nut which are significant to the dynamics of ball screw drives.

This thesis employs a hybrid FEM methodology originally introduced by the author in [54] where the ball screw is modeled as a Timoshenko beam, while the other more rigid components are modeled as lumped masses/inertias connected by springs. Furthermore, it builds upon the work of Zaeh et al [88] by deriving two new screw-nut interface stiffness matrices. One of the matrices is derived based on the assumption that the screw acts as a rigid body within the nut while the other is derived by considering the elastic deformations of the screw within the nut. The former matrix is shown to be better suited for short nuts and rigid ball screws while the latter is developed for longer nuts and more flexible ball screws. Both stiffness matrices are shown to contain additional cross-coupling terms between the deformations in the axial, torsional and lateral directions of the ball screw and nut which are not found in previous models. These additional cross-coupling terms are shown to play a significant role in the dynamics of high speed ball screw drives through simulations and experiments.

### 2.2.2 Parameter Identification

Parameter identification from experimental measurements is often carried out to obtain accurate values for the physical quantities that constitute the analytical models described in the previous section.

Allotta et al [1] used modal updating techniques to identify the position dependent boundary conditions of a ball screw system. They first created a free-free finite element model (i.e. without physical constraints) of the screw. Then, using scalar springs with unknown stiffnesses in different directions, they applied boundary conditions corresponding to the bearings and nut supports. By matching the resonance and anti-resonance frequencies of the modeled and experimentally measured frequency response functions (FRFs) the unknown stiffness coefficients of the constraints were identified using an iterative technique. Lee et al [46] proposed an experimental technique for identifying the parameters of a flexible ball screw drive model based on contour error measurements using a cross grid encoder. They outlined a procedure for tuning the controller parameters in order to reduce the structural vibrations of the machine tool thus improve its overall contouring accuracy by using the model and contour error measurements. A procedure for identifying unknown joint parameters in a servomechanism with multiple joints was proposed by Yang and Lin [86]. The method worked by comparing Bode graphs of the experimental and analytical models to identify the stiffness and damping coefficients. Sensitivity techniques were then applied to reduce the discrepancies between the eigenvalues obtained from analytical and experimental models. The joint parameters of an industrial servomechanism consisting of a motor, a ball screw, some gears and linkages were identified using the method. Kamalzadeh and Erkorkmaz [40] identified the mass, damping and stiffness matrices of a 2-DOF ball screw model by matching the FRF obtained from the model to the FRF measured from the drive. However, their method failed to identify off-diagonal terms in the mass matrix of the drive which are very important for accurate control of flexible ball screw drives.

This thesis presents a simple but effective least squares method for identifying the mass, damping and stiffness matrices of a 2-DOF model of ball screw drives (including the off-diagonal terms in the drive's mass matrix) based on FRF data

## 2.3 Control of Flexible Ball Screw Drives

The influence of structural resonances significantly limits the achievable bandwidth of ball screw drives [61]. Therefore, there is a significant amount of research activity in the area of designing controllers which directly or indirectly address the problem of structural dynamics in ball screw-driven machines.

One technique commonly used to tackle this problem is to pre-filter motion commands before applying them to the servo controller [37][81], or to modify the frequency content of the command and feedback signals using a notch filter set at the resonance frequency of the drive [28][29][54][70][90]. Notch filters prevent the control signal from exciting the problematic modes but cannot stop the table disturbance forces from exciting them. They also tend to have a negative effect on the phase margin of the controlled system. Furthermore, they are not robust to changes in the behavior of the resonance mode due to changing table position or workpiece mass.

Lim et al [48][49] have reported that a torsional displacement feedback control scheme, which is based on an estimation of the torsional displacement of flexible ball screws using known stiffness properties and motor torques, leads to a significant reduction in the positioning error of the table. A similar strategy has also been adopted by Kamalzadeh and Erkorkmaz [41][42] who propose two methods for canceling out axial elastic deformations in ball screw drives. The first method [41] is a feed-forward technique which calculates the motor torque based on the reference commands and the modeled friction behavior of the drive. The second method [42], on the other hand, is a feedback strategy which uses the control voltage applied to the drive to estimate the motor torque. They observe that the first method has better stability margins than the second, albeit less robust to un-modeled disturbances and changes in workpiece inertia. They improve the stability margins of the feedback method by low-pass filtering the control voltage before using it for elastic deformation cancelation.

As an alternative approach, Erkorkmaz and Kamalzadeh [29] have also proposed an active vibration suppression method based on measuring the twist of the ball screw using two rotary encoders placed at either end of the ball screw. Vibration cancelation is achieved by calculating a negative torque proportional to the measured twist of the ball screw and applying it to the drive.

Chen and Tlusty [15] showed by simulation that applying accelerometric feedback combined with a feed-forward compensator on a flexible ball screw drive improved the transient response at the machine tool table, and chatter vibration characteristics between the cutting force and machined part.

Symens et al [72] resorted to gain-scheduling as an alternative to classical fixed-parameter controllers which do not perform well for machine tools with varying structural flexibility. They employed two different scheduling schemes – one ad-hoc and the other analytically derived – on $H_\infty$ controllers designed for various positions of a machine tool with position-dependent structural dynamics. Their experiments yielded good results from the ad-hoc scheme but the analytically derived linear parameter varying (LPV) scheduling gave very poor results because of the inherent conservatism in the LPV method. Zhou et al [91] used simulations to demonstrate the merits of applying an "adaptive" notch filter to table-position-dependent torsional modes of a ball screw drive. They used neural networks to tune the parameters of the notch filter as a function of the table's position. Dumur et al [25] employed an adaptive generalized predictive controller to damp out the structural modes of ball screw drives in the presence of variations of drive inertia, but they did not consider the effects of table position-dependent structural dynamics variations in their controller.

A different approach was taken by Van Brussel et al [76]. They capitalized on the robustness of the $H_\infty$ controller, by performing a design based on the nominal position of the machine tool, while factoring the information regarding the position-dependent variation of the machine dynamics into the uncertainty model of the controller. Their controller, which considered the flexibilities of the machine, was shown to outperform a reference PID controller which was designed based on only rigid-body dynamics, in tracking performance. However, when it came to disturbance rejection, the $H_\infty$ controller was seen to perform poorly. Its disturbance rejection performance was improved by building it around a velocity loop closed with a PI-Controller which added more damping to the system.

Erkorkmaz [28] designed an elaborate adaptive sliding mode controller (ASMC) to actively damp the first torsional mode of a ball screw drive. The controller was shown to improve the high speed tracking and contouring performance of the drive significantly when compared to a similar design which did not consider the flexibility of the drive. Similarly, Kamalzadeh and Erkorkmaz [40] designed a mode-compensating ASMC to actively damp out the first axial-torsional vibration mode of ball screw drives. The effectiveness of their design was improved by using feed-forward action to force the motor to follow a different reference command than the table. While the table was made to follow the desired trajectory, the motor's reference command was made to cancel the deformations of the ball screw arising from inertial forces and/or estimated disturbance forces. Their design, however, did not consider the effects of non-minimum phase zeros on the effectiveness of their mode-compensating ASMC.

The implications of non-minimum phase (NMP) zeros on non-collocated control of flexible systems has been studied extensively by Spector and Flashner [71]. Non-collocated control occurs in plants whose actuator(s) are not coincident with the location(s) of feedback measurement. Spector and Flashner observe that NMP zeros are an inescapable result of the finite propagation speed of elastic deformation waves in flexible structures. From their study they conclude that the transfer functions of non-collocated systems are always NMP beyond some finite frequency and that qualitatively erroneous control signals could result by mis-modeling a NMP system with a minimum phase model. Freudenberg and Looze [32] also indicate that NMP feedback systems are severely limited in their achievable closed-loop performance, particularly in terms of sensitivity and complementary sensitivity. Varanasi and Nayfeh [79], in agreement with the findings of Spector and Flashner [71], observe that the off-diagonal terms in the mass matrix of their 2-DOF ball screw drive model tend to give rise to NMP zeros in the non-collocated dynamics of flexible ball screw drives from motor torque to table position.

The effects of NMP zeros on the feed-forward control of single input-single output (SISO) closed-loop systems was studied extensively by Tomizuka [73] who introduced the zero phase error tracking controller (ZPETC). The ZPETC is a feed-forward controller that cancels out all of the poles and stable zeros of a closed-loop system. The NMP (unstable) zeros, on the other hand, are approximately canceled out in a way that theoretically yields zero phase lag between the command and actual position signals, and a gain that is very close to unity for a wide frequency range. This pioneering work of Tomizuka has been followed by many similar feed-forward SISO control techniques [33][34][74][81], all of which result in non-causal systems.

The problem with feed-forward controllers, however, is that they are unable to detect and take corrective action against deviations arising from external disturbances and/or modeling errors [63]. To exploit the advantages of feed-forward controllers, they should be used together with robust feedback control action. The adaptive sliding mode controller, introduced by Slotine and Li [69], is one of such controllers which combine feed-forward action with robust feedback control. This is one reason why it is often employed for feed drive control [5][28][29][40]. However, the performance of the ASMC is limited because its disturbance adaptation and sliding surface dynamics are coupled. In response to this shortcoming, Won and Hedrick [83] have proposed the disturbance adaptive discrete-time sliding mode controller (DADSC) for SISO systems. They demonstrate the advantages of the DADSC over the ASMC using the speed control of engines.

This thesis addresses the challenge of controlling flexible ball screw drives by proposing mode-compensating DADSCs combined with a feed-forward minimum tracking error filter (MTEF) designed to actively damp the first axial-torsional-lateral mode of ball screw drives. The plant inversion-based MTEF is designed such that it is stable, causal and effective even when the identified open-loop dynamics of the ball screw drive contains NMP zeros. Furthermore, the parameters of the proposed controllers are scheduled in an ad hoc fashion to achieve effective vibration cancelation as the properties of the suppressed mode change as a function of the table position.

## 2.4 Control and Dynamic Stiffness Enhancement of Direct-Driven Machines

Unlike ball screw drives, direct drives are not prone to low-frequency vibration modes, so they are usually modeled simply as a pure mass with some viscous damping [77]. However, as previously mentioned, their direct nature makes them sensitive to cutting force disturbances and workpiece inertia variations which have to be dealt with using the controller [2][77].

Xu and Yao [85] introduce an adaptive robust controller (ARC) for linear motors. The controller has an online parameter adaptation scheme that is utilized to reduce the effects of uncertainties coming from the workpiece inertia, friction, force ripple and amplifier parameters. The uncompensated uncertain non-linearities are then handled by robust control laws thereby achieving high performance. Implementation problems related to the parameter adaptation are mitigated by making the regressor dependent on only the reference trajectory as opposed to the system states. Shieh and Tung [68] design an optimal linear quadratic controller for direct drives which considers the uncertainties due to payload variation and time-varying disturbances. They guarantee robustness by connecting an auxiliary input to the nominal optimal control. In [26], Egami and Tsuchiya regard the influence of parameter variation and disturbance forces of a linear motor system as an equivalent disturbance signal. Compensation action is realized using the estimated value of the equivalent disturbance thereby achieving an improvement of the phase delay of the whole control system and a reduction in the effects of the parameter variation on the performance of the drive.

Renton and Elbestawi [66] propose minimum-time path optimization (MTPO) combined with minimum-time tracking control (MTTC) to improve the performance of direct drives. The MTPO is used to schedule the maximum feed rate along a tool path in such a way as to avoid exceeding the velocity/acceleration limits of each of the machine's axes. The MTTC, on the other hand, attempts to move the drive to the target path (i.e. position and velocity) as quickly as is allowed by the current and voltage limits of the amplifier using feed-forward action. They also suggest the use of a "periodic observer" for estimating and canceling out periodic cutting forces applied to direct drives within the bandwidth of the controller. Similarly, Komada et al [45] propose a disturbance observer for improving acceleration control of direct drives. In order to reduce the effects of noise and quantization errors on the performance of the designed disturbance observer, its poles are scheduled as a linear function of the desired speed of the drive.

Jamaludin et al [36] controlled a two-axis linear motor using the classical cascaded controller. In addition, they modeled the friction on the guides and predicted the remaining un-modeled friction using an observer based on the inverse model of the machine dynamics. They added a repetitive controller to the position control loop, which reduced the effect of periodic cutting forces significantly and led to higher dynamic stiffness on the linear drives. Castaneda-Castillo and Okazaki [13] attempted to achieve cutting force compensation using a model reference control algorithm. They estimated cutting forces in a three-axis milling machine using recursive least-squares by considering them as variations in inertia. However, they were only able to estimate very low frequency loads (i.e. less than 10 [Hz]). Denkena et al [23] experimentally identified the friction, damping and cogging force patterns of a direct drive. They then controlled the drive using a state-space controller with disturbance compensation. Finally, they demonstrated tool breakage monitoring based on cutting forces calculated from the motor current.

Chung et al [18] propose a variable structure controller (i.e. sliding mode controller), for direct drives, with integral action in the sliding surface and disturbance estimation using a load torque observer. The integral action improves robustness to unknown disturbances while the load torque observer reduces unwanted chattering in the sliding mode controller (SMC). Wang et al [80] contend that when a plant controlled by a SMC reaches sliding mode, the closed-loop behavior of the controlled system is independent of the plant dynamics. Therefore, a feed-forward controller designed based on the closed-loop dynamics of a SMC at sliding mode theoretically should be independent of the plant model. However, they observe that the presence of disturbance forces and model uncertainties prevent the controlled system from fully reaching sliding mode. They demonstrate their controller on a linear motor driven-stage

Alter and Tsao [2][3] designed two $H_\infty$ controllers aimed at improving the dynamic stiffness of direct drives. The first was designed to yield a position feedback controller with integral action while the second included optimal force feedback control. Based on experimental results, the first $H_\infty$ controller showed a 26-47 [%], while the second exhibited a 70-100 [%] improvement in dynamic stiffness over a proportional derivative (PD) controller. Choi and Tsao [16] modeled the average cutting force in two-dimensional milling operations as the product of a constant (but uncertain) gain and the velocity of the orthogonal direct-driven axes. They then designed a robust multi input-multi output (MIMO) $H_\infty$ controller for the two axes coupled by the cutting force equation. Simulation and experimental results demonstrated that the MIMO design outperforms an axis-based SISO PID controller design in terms of tracking and contouring performance under cutting conditions.

Van Brussel et al compared a sliding mode controller to a robust $H_\infty$ and pole-placement controller for controlling a direct drive with changing inertia. They observed that the SMC performed better than the other two controllers. By adjusting the weighting factors of the $H_\infty$ controller to match the behavior of the SMC, they were able to achieve good performance with the $H_\infty$. Similar results were also demonstrated in [78]. Jamaludin et al [35] compared a classical cascaded controller to a SMC for a direct drive. They observed that both controllers performed similarly in terms of tracking performance but that the SMC exhibited better dynamic stiffness properties than the classical cascade controller (except at the low frequency range because of a lack of integral action in their SMC). They however did not compare the dynamic stiffness of the two controllers at the most critical point – the resonance frequency of the controlled drive where the drive's flexibility is usually lowest.

Chung et al [17] explain that there are three types of modes (in addition to the controller-induced modes) which contribute to the dynamic stiffness between tool and workpiece in machine tools – spindle modes, tool modes and machine tool structural modes. The tool and spindle modes are usually at relatively high frequencies – typically greater than 400 [Hz]. The structural modes, however, are those low-frequency modes (typically less than 100 [Hz]) which result from motions like the rocking of the machine's column or bed. They demonstrate how the dynamic stiffness of such low-frequency modes could be improved by using a tuned active damping device attached to the machine tool. Similar results are also demonstrated by Brecher et al in [11]. The problem with active damping techniques, however, is that they involve building or purchasing a damping device, carefully searching for the best location to mount it on the machine tool and then tuning it iteratively to achieve the best performance. To mitigate this problem, Zatarain et al [89] use an accelerometer attached to the tool center point (TCP) to measure the vibratory displacements of the tool based on a state-space observer. The estimated displacements are then fed back to the controller and used to improve the dynamic stiffness of the drive between the tool and workpiece by up to 70 [%]. However, attaching an accelerometer to a rotating tool is a challenging task practically.

This thesis proposes a two-pronged approach for dynamic stiffness enhancement of direct-driven machine tools. First, it designs a rigid body dynamics-based DADSC to achieve high bandwidth and dynamic stiffness in the control loop of direct drives, particularly at the resonance frequency of the controlled drive. The decoupling of disturbance estimation and sliding surface dynamics in the DADSC is shown to give it superior dynamic stiffness compared to the ASMC and cascaded controller, while remaining as good as the other two controllers in terms of reference tracking performance and simplicity. It also proposes a technique for further improving the dynamic stiffness between tool and workpiece, in direct-driven machine tools, by canceling out low-frequency vibrations resulting from machine tool structural modes. The technique is based on accurately estimating the cutting force disturbances applied to the drive, using true disturbance force recovery, and then utilizing the estimated (recovered) forces to predict the relative displacement between tool and workpiece based on the measured or modeled transfer function of the machine.

## 2.5 Online Mass Estimation for High Speed Feed Drives

The variation of workpiece mass during cutting operations changes the behavior of structural modes in flexible ball screw drives thereby reducing the effectiveness of mode-compensation techniques in suppressing them. It also leads to a loss of bandwidth in both direct drives and ball screw drives. Online workpiece mass estimation is instrumental in mitigating the adverse effects of workpiece mass change on the dynamics of high speed feed drives [61].

Liu et al [51] design three different adaptive controllers with online mass estimation – a backstepping adaptive controller, a self-tuning adaptive controller, and a model reference adaptive controller – for a linear motor direct drive. Using the designed controllers, they experimentally demonstrate satisfactory performance in transient response, load disturbance rejection capability and tracking ability even when the inertia of the drive is increased up to ten times. Qian et al [65] propose a method based on neural networks for estimating the varying workpiece mass of direct drives. The estimated mass is used to switch between three controllers designed in order to achieve robust control in presence of workpiece mass variation. Hirovonen et al [38] design an adaptive nonlinear backstepping controller for a direct drive. They assume that the direct drive is used to move a flexible workpiece with an unknown mass and stiffness, both of which are estimated by the controller. They also note that the parameter estimates of the controller do not converge to their true values even though the stability of the controller is guaranteed by a Lyapunov function.

Butler et al [12] control a direct-drive using a model reference adaptive approach. The inertia of the actual drive is estimated using recursive least squares and used to update the reference model. This adaptive control scheme is shown to perform better than a fixed PID controller, designed for the same drive, in terms of tracking performance. Similarly, Dessaint et al [24] use recursive least squares to estimate the inertia and damping parameters of a linear drive controlled by a PID regulator with an additional feed-forward loop. They use the identified parameters to adjust the parameters of the feed-forward loop of the controller.

In terms of ball screw drive control, Dumur et al [25] used an adaptive generalized predictive controller (GPC) to damp out the structural modes of flexible ball screw drives in the presence of variations of drive inertia. Online parameter estimation was carried out using a recursive least squares technique with conditional updating. Simulation results demonstrated significant advantages of using the adaptive GPC over the fixed GPC in terms of reference tracking performance.

A major drawback of the online mass estimation techniques described above is that they do not consider the effects of cutting force disturbances on the accuracy of parameter estimation. In reality, however, the mass change is usually accompanied by large dynamic forces which greatly affect the effectiveness of mass estimation techniques. This challenge is addressed by Lee et al [47] who carry out simultaneous disturbance torque and inertia estimation using a full order observer and a reduced-order extended Luenberger observer (ROELO). They use the ROELO to estimate the inertia of the drive, based on the disturbance torque values estimated at the previous time step using the full order observer, by assuming that the disturbance torque remains constant. The full order observer is then updated with the identified inertia value by assuming that it too remains constant over the time step. This method is only suitable for quasi-static disturbance forces and mass variations at low rates, which is not the case in most high speed machining operations. Similarly, Awaya et al [9] use a disturbance observer for inertia estimation as well as for disturbance compensation in a ball screw-driven machine. However, they again assume that the disturbance force is constant and that the reference commands are periodic, both of which are unrealistic assumptions in most machining operations.

Some of the control methods described earlier (e.g. [13][26][85]) also attempt to estimate both workpiece mass and disturbance forces simultaneously. However, as Erkormaz [28] explains, persistence of excitation is necessary for the parameters of adaptive controllers to converge. Persistence of excitation is hardly achieved in feed drives because of the smoothness of the reference commands applied to them [28].

In response to the practical difficulty of accurately estimating workpiece mass in the presence of cutting force disturbances, Renton and Elbestawi [66] suggest that the mass of the workpiece be estimated during rapid traverse motions when the disturbance force is zero. However, in many cutting operations, such interruptions in cutting may scarcely occur.

This thesis exploits the periodicity of certain cutting operations and the low-frequency properties of ball screw and direct drives to introduce a method which estimates the varying workpiece mass using "zero-force pockets" that occur in the frequency spectrum of unknown periodic signals. As a result, accurate online mass estimation can be achieved without interrupting the cutting operation.

### 2.6 Summary

In this chapter, literature related to modeling and control of flexible ball screw drives, control and dynamic stiffness enhancement of direct-driven machines, and online workpiece mass estimation for both types of high speed feed drives have been highlighted. The motivation for research into these areas, and the various solutions put forward by other researchers have been discussed so as to place the work that follows in perspective, and provide a background for further research into these topics.

# Chapter 3

## Modeling and Identification of the Dynamics of Flexible Ball Screw Drives

### 3.1 Overview

Designing effective controllers for high speed ball screw drives requires a good understanding and accurate characterization of the structural dynamics of the ball screw mechanism, and its potential interaction with the controller dynamics of the drive. To achieve this purpose, this chapter presents a two-pronged approach consisting of analytical modeling using finite element methods, and parameter identification based on experimentally measured data. The finite element model is used to get a global picture and gain theoretical understanding of ball screw drive structural dynamics, particularly the complex transmission of motion and vibrations at the screw-nut interface. The experimental parameter identification is then used to obtain a more compact and accurate representation of the dynamics needed for controller design.

The content of this chapter is arranged as follows. Section 3.2 gives a brief introduction to ball screw mechanisms and then presents an overall picture of the finite element modeling technique employed in this thesis. Detailed modeling of the screw-nut interface connection is then laid out in Section 3.3. In Section 3.4, the developed model is implemented on a single-axis ball screw test bed and the resulting open-loop dynamics are analyzed using simulations and then corroborated experimentally. A method for accurately extracting the mass, damping and stiffness matrices of the drive from experimental measurements is presented in Section 3.5, and concluding remarks are given in the last section.

### 3.2 Modeling of Drive Components

A typical drive consists of a ball screw which is attached to the motor shaft through a coupling as shown in Figure 3.1. The screw is constrained axially and radially by a thrust bearing at the motor side. The screw is either unsupported, if it is short, or supported by a radial bearing to provide axial freedom in order to allow for its thermal expansion. Pre-tensioned ball screws also exist for which the distal end of the screw is supported axially in order to keep it in tension. This way, stresses resulting from thermal growth are reduced. The rotary motion of the screw is converted into a translation at the nut, which is connected to the table supported by the guideways at two parallel sides.

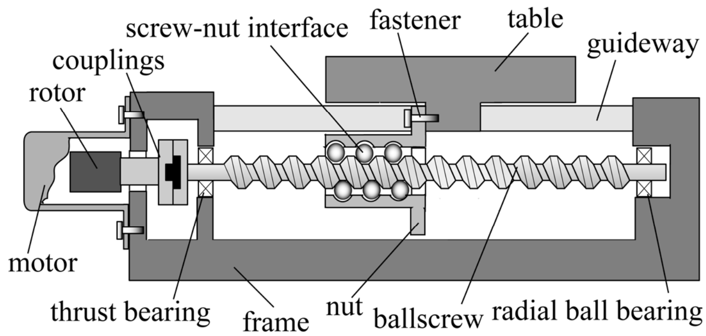


**Figure 3.1: Mechanical Components of a Ball Screw Feed Drive**

### 3.2.1 Ball Screw

The threads of the ball screw do not make any substantial contribution to its stiffness however they contribute to its inertia as presented in [70]. Therefore, instead of modeling it using three dimensional elements, the ball screw is usually modeled accurately using beam elements [10][29][39][70][79][84][88]. Timoshenko beam elements are used because they consider shear effects in lateral deformation formulations, and give a more accurate prediction of high-frequency natural modes, when compared to Euler-Bernoulli beams [52], especially when the beam is short. The root diameter ($d_r$) is used to derive the stiffness matrix, while an equivalent diameter ($d_e$) is used to calculate the mass matrix at the threaded section of the screw. The equivalent diameter is obtained by equating the mass of a cylinder having a diameter ($d_e$) to the mass of the threaded section including the threads:

$$d_e = \sqrt{\frac{4\left(\frac{\pi d_r^2}{4} L + V_{thr}\right)}{\pi L}} \tag{3.1}$$

where $L$ represents the length of the threaded section and $V_{thr}$ is the total volume of the threads which can be estimated from their geometry. Each beam element has six degrees of freedom (DOF) on each of its two nodes; three translations ($u_x$, $u_y$, $u_z$) and three rotations ($\theta_x$,

$\theta_y$, $\theta_z$) as shown in Figure 3.2. The expressions for the element stiffness and mass matrices of a Timoshenko beam can be found in literature [64][87].

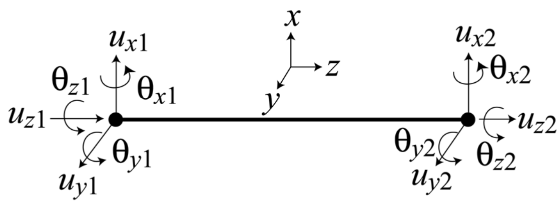


**Figure 3.2: Timoshenko Beam Element**

### 3.2.2 Rigid Components

Components like the rotor, nut, table and frame are relatively more rigid than the ball screw and joint interfaces, hence they are approximated by lumped inertia properties defined at their centers of mass. The mass matrix (Eq.(3.2)) of rigid components consists of a translating mass ($m$) and nine rotary inertias ($I_{xx}$, $I_{yy}$, $I_{zz}$, $I_{xy}$, $I_{yx}$, $I_{xz}$, $I_{zx}$, $I_{yz}$, $I_{zy}$), and in the most general case is given by:

$$\mathbf{M} = \begin{bmatrix} m & 0 & 0 & 0 & 0 & 0 \\ 0 & m & 0 & 0 & 0 & 0 \\ 0 & 0 & m & 0 & 0 & 0 \\ 0 & 0 & 0 & I_{xx} & I_{xy} & I_{xz} \\ 0 & 0 & 0 & I_{yx} & I_{yy} & I_{yz} \\ 0 & 0 & 0 & I_{zx} & I_{zy} & I_{zz} \end{bmatrix} \tag{3.2}$$

In cases where information in the form of displacements and forces are desired at other locations of the component, a rigid-body transformation matrix ($\mathbf{T}_{P\text{-}COM}$) is used to map the information at the center of mass (COM) to the desired location, $P$, as:

$$\begin{Bmatrix} \mathbf{u} \\ \boldsymbol{\theta} \end{Bmatrix}_P = \underbrace{\begin{bmatrix} \mathbf{I}_{3\times3} & -\mathrm{S}(\mathbf{r}) \\ \mathbf{0}_{3\times3} & \mathbf{I}_{3\times3} \end{bmatrix}}_{\mathbf{T}_{P\text{-}COM}} \begin{Bmatrix} \mathbf{u} \\ \boldsymbol{\theta} \end{Bmatrix}_{COM} \tag{3.3}$$

where $\mathbf{u}$ and $\boldsymbol{\theta}$ are the displacement and rotation vectors at a given location, expressed as $\mathbf{u} = \{u_x\ u_y\ u_z\}^T$ and $\boldsymbol{\theta} = \{\theta_x\ \theta_y\ \theta_z\}^T$, respectively (see Figure 3.2). $\mathbf{r}$ is the position vector from the

COM to point $P$ given by $\mathbf{r} = \{r_x\ r_y\ r_z\}^T$ while S($\mathbf{r}$) is the tensorial representation of $\mathbf{r}$ given by:

$$\mathrm{S}(\mathbf{r}) = \begin{bmatrix} 0 & -r_z & r_y \\ r_z & 0 & -r_x \\ -r_y & r_x & 0 \end{bmatrix} \tag{3.4}$$

Eq.(3.4) assumes that the table and nut undergo small rotations, since their rigid-body motions are translations along the feed axis. The generalized force vector, $\mathbf{F}_P = \{F_x\ F_y\ F_z\ M_x\ M_y\ M_z\}^T$, consisting of forces and moments applied at point $P$, is transformed from the point $P$ to the COM by the transpose of the transformation matrix, $\mathbf{T}_{P\text{-}COM}$ as:

$$\mathbf{F}_{COM} = \mathbf{T}_{P-COM}^T \mathbf{F}_P \tag{3.5}$$

### 3.2.3 Joint Interfaces

Couplings, bearings, fasteners and guideways are modeled as linear spring elements in the directions of compliance as shown in Table 3.1. If the joint modeled as a spring element possesses considerable inertia, the inertia is lumped at both ends of the spring and attached to the adjoining components. This is the case, for instance, in jaw couplings where the inertia of the jaws is lumped to the components joint by the coupling.

## 3.3 Screw-Nut Interface

One aspect of ball screw drives that requires a great deal of attention when modeling is the interface between the ball screw and nut. This is because it plays an important role in the transmission of motion, vibrations and forces from the ball screw to the table. As explained in Chapter 2, current models of the screw-nut interface consider only the axial and/or torsional deflections of the ball screw while assuming that the lateral deformations of the ball screw are decoupled from its torsional and axial deformations so cannot be transmitted through the screw-nut interface to the table. In a previous work [54], the author presented the theoretical framework for a comprehensive model which includes axial, torsional and lateral dynamics of the ball screw in the formulations of a new screw-nut interface model. This original model was however tentative and largely unverified experimentally. Here, the author revisits the originally proposed screw-nut interface model and produces a more definitive model which better describes the interaction between axial, torsional and lateral dynamics at the screw-nut interface.

| Joint | Model (Constraint) |
|---|---|
| Torsional Coupling | Torsional spring (in $\theta_z$ direction) - see Figure 3.2 for coordinate axes |
| Thrust Bearing | Axial spring (in $z$-direction), lateral springs (in the $x$ and $y$-directions) and rotational springs (in $\theta_x$ and $\theta_y$ directions) |
| Radial Bearing | Lateral springs (in the $x$ and $y$-directions) |
| Fasteners | Springs in directions of significant compliance |
| Guideway | Lateral springs (in the $x$ and $y$-directions) at each slide located at the corners of the table. |

**Table 3.1: Typical Spring Element Models (Constraints) of Joints in Ball Screw Drives**

### 3.3.1 Modeling of Interface Stiffness

Preloaded balls are inserted between the nut and screw in order to convert the sliding friction present in Acme leadscrews to rolling friction. The preload applied at the screw-nut interface helps to mitigate backlash effects and increase the rigidity of the drive. As a result of the preload, some of the balls in the interface contact the screw's threads on its upper ($U$) side while others make contact on its lower ($L$) side [55].

In modeling the screw-nut interface, the mass of the balls is assumed to be negligible, while all the compliance is assumed to come from their point of contact with the screw and nut. Therefore, the balls are modeled as massless springs having a stiffness $k_{Ball}$ aligned along the common line of contact (contact normal) between screw and nut [88] as depicted in Figure 3.3(a).

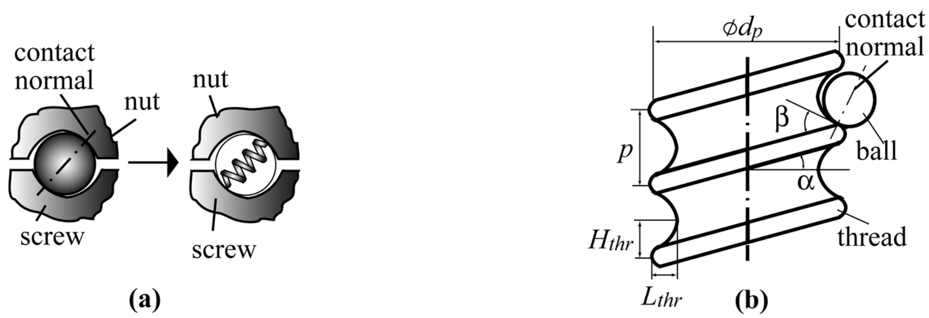


**Figure 3.3: (a) Spring Model of Balls in Screw-Nut Interface (b) Orientation of Contact Normal**

In order to apply the stiffness of each ball to the finite element (FE) beam model of the ball screw and lumped-inertia model of the nut, a two-stage transformation is used. The first stage of the transformation is used to convert $k_{Ball}$ from a local coordinate system, established for each ball, to the global coordinate system defined for the ball screw drive (as shown in Figure 3.2). The second stage of the transformation is developed in order to lump the stiffness of all the balls distributed all around the screw-nut interface such that they can be connected to the nut node, and to one or more nodes on the ball screw. The stiffness matrices for the screw-nut interface are then obtained by applying the two-stage transformation to $k_{Ball}$ as explained in the following subsections.

### 3.3.2 First Stage of Transformation: Local to Global Coordinates

The orientation of the contact normal along which the spring stiffness ($k_{Ball}$) is aligned is described by the angles $\alpha$ and $\beta$ [88] as shown in Figure 3.3(b). The pitch angle ($\alpha$) of the ball screw is given by:

$$\alpha = \tan^{-1}\left(\frac{p}{\pi d_p}\right) \tag{3.6}$$

where $p$ is the pitch and $d_p$ is the pitch diameter of the ball screw. $\beta$ is the mean thread angle at the ball contact point. $H_{thr}$ and $L_{thr}$ are the height and length of the thread, respectively.

In order to simplify the analysis, the ball screw thread is unwrapped and represented as a double-inclined plane, inclined at angles $\alpha$ and $\beta$, as shown in Figure 3.4(a). Two coordinate systems, $CS_{1L}$ and $CS_{2L}$, are attached to the centre of each ball resting on the plane. $CS_{1L}$ is aligned such that its $z$-axis points along the contact line of the ball, normal to the plane (i.e. the direction of $k_{Ball}$), while $CS_{2L}$ is established so that its $z$-axis is parallel to the ball screw's axis (global $z$-axis), and its $y$-axis lies along the radial line from the ball's centre to the axis of the ball screw (see Figure 3.5 for clarity).

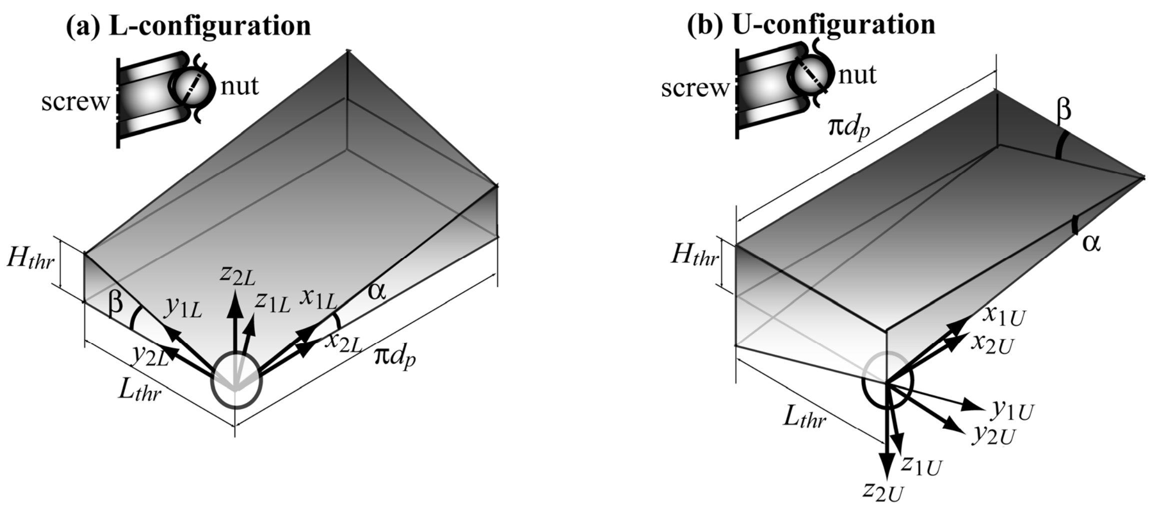


**Figure 3.4: Inclined Plane Representation of Ball Screw Thread**

The coordinates, $CS_{1U}$ and $CS_{2U}$ on Figure 3.4(b) are established following the same logic, except that they represent the case where the ball-contact configuration is reversed as shown in the figure. The subscripts $L$ and $U$ are used to differentiate the ball-contact configurations as "lower" and "upper", respectively.

For the $L$-configuration, the transformation $\mathbf{T}_{2L\text{-}1L}$ that obtains $CS_{2L}$ from $CS_{1L}$ is derived by a current-frame rotation of $-\alpha$ and $\beta$ about the $y$ and $x$-axis, respectively, and modeled as:

$$\mathbf{T}_{2L-1L} = \mathrm{Rot}_y(-\alpha) \cdot \mathrm{Rot}_x(\beta) \tag{3.7}$$

where Rot represents a rotation operator about the axis specified by the accompanying subscript. More details about the Rot operator are given in Appendix A.

The transformation $\mathbf{T}_{2U\text{-}1U}$, which obtains $CS_{2U}$ from $CS_{1U}$ is calculated in a similar fashion, except this time the current-frame rotation is first $\alpha$ about the $y$-axis and then $-\beta$ about the $x$-axis:

$$\mathbf{T}_{2L-1L} = \text{Rot}_y(\alpha) \cdot \text{Rot}_x(-\beta) \tag{3.8}$$

Since the spring deformation always occurs along the $z_1$-axis in both configurations, the transformations $\mathbf{T}_{2L\text{-}z1L}$ and $\mathbf{T}_{2U\text{-}z1U}$ are obtained by post-multiplying $\mathbf{T}_{2L\text{-}1L}$ and $\mathbf{T}_{2U\text{-}1U}$ by a unit vector in the $z_1$-direction, as:

$$\mathbf{T}_{2L-z1L} = \mathbf{T}_{2L-1L} \cdot \{0 \quad 0 \quad 1\}^T; \qquad \mathbf{T}_{2U-z1U} = \mathbf{T}_{2U-1U} \cdot \{0 \quad 0 \quad 1\}^T \tag{3.9}$$

Here $\mathbf{T}_{2L\text{-}z1L}$ is the transformation which obtains $CS_{2L}$ from $z_{1L}$, while $\mathbf{T}_{2U\text{-}z1U}$ is the transformation that obtains $CS_{2U}$ from $z_{1U}$. The same notation is used for all the transformation matrices hereinafter.

Figure 3.5 shows the relationship between the previously described coordinate systems, $CS_{2L}$ and $CS_{2U}$, and a new coordinate system, $CS_4$. $CS_4$ is centered at a specified point $P_4$ along the axis of the screw, and aligned in such a way that its three axes are parallel to the global axes of the ball screw. Another coordinate system $CS_3$ (not shown in the figure) is established such that it has all its axes parallel to $CS_4$ but its origin is located at the centre of each ball. In order words, $CS_3$ is a ball-centered global coordinate system. The transformation, $\mathbf{T}_{3\text{-}2L}$ is simply a rotation about the $z_3$-axis (or $z_4$-axis) by an amount $\phi$. Here the azimuth angle $\phi$ [88] represents the angle measured in the counter-clockwise direction from the $x_3$-axis (or $x_4$-axis) to the $x_{2L}$ or $x_{2U}$-axis. As will be explained later, the angle $\phi$ specifies the location of the centre of each ball along the ball screw thread.

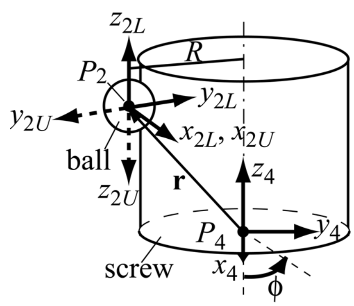


**Figure 3.5: Relationship between Ball Coordinates and Screw Coordinates**

In order to obtain $\mathbf{T}_{3\text{-}2U}$, first the $y_{2U}$ and $z_{2U}$-axes are flipped using a Boolean matrix so that they coincide with their corresponding axes in $CS_{2L}$. This is followed by a rotation about the $z_3$-axis by the angle $\phi$. The transformations are expressed as:

$$\mathbf{T}_{3-2L} = \mathrm{Rot}_z(\phi); \qquad \mathbf{T}_{3-2U} = \mathrm{Rot}_z(\phi)\cdot\begin{bmatrix} 1 & 0 & 0 \\ 0 & -1 & 0 \\ 0 & 0 & -1 \end{bmatrix} \tag{3.10}$$

The transformation from each local coordinate system to the global coordinate system for the $L$ and $U$-configurations, $\mathbf{T}_{3\text{-}z1L}$ and $\mathbf{T}_{3\text{-}z1U}$, are given by:

$$\mathbf{T}_{3-z1L} = \mathbf{T}_{3-2L}\cdot\mathbf{T}_{2L-z1L}; \qquad \mathbf{T}_{3-z1U} = \mathbf{T}_{3-2U}\cdot\mathbf{T}_{2U-z1U} \tag{3.11}$$

Since these transformation matrices are orthonormal, the inverse transformations, $\mathbf{T}_{z1L\text{-}3}$ and $\mathbf{T}_{z1U\text{-}3}$, are simply given by the transpose of their corresponding forward transformations, $\mathbf{T}_{3\text{-}z1L}$ and $\mathbf{T}_{3\text{-}z1U}$.

### 3.3.3 Second Stage of Transformation: Lumping to Nodes

It is obvious from the previous section that each ball in the screw-nut interface has a unique local-global transformation matrix which depends on its contact configuration ($L$ or $U$) and its azimuth angle $\phi$ (Figure 3.5). However, the nut is modeled as a lumped mass represented by a single node located at its COM, whiles the ball screw, being an FE beam, has discrete nodes along its axis. The aim of the lumping explained in this section is therefore to develop transformation matrices between the ball-centered global coordinate systems for each ball, to node-centered global coordinate systems attached to the nut and ball screw nodes. This way, the ball stiffness matrices distributed all around the contact interface can be connected to the nodes of the nut and ball screw.

In [54] the author proposed two methods for performing this lumping operation – the Rigid Ball Screw method and the Shape Function method. Even though neither of these methods was fully verified experimentally, the preliminary simulation tests carried out in [54] indicated that the Shape Function method yielded unreasonable results. The results from the Rigid Ball Screw method, on the other hand, were more realistic. Necessary theoretical modifications have been made to the Shape Function method and its revised version, together with the original version of the Rigid Ball Screw method, is presented below. A comparison of the performance of two methods is provided in Appendix B.

### (A) Rigid Ball Screw Method

In this method, the region of the drive within the screw-nut interface is assumed to move as a rigid body. In order words, the motion of the screw is assumed to be characterized by a translation ($\mathbf{u}_{BS}$) measured at a point $P$ located within the nut, and a rotation ($\boldsymbol{\theta}_{BS}$), as shown in Figure 3.6. Point $P$ is the origin of the $CS$ coordinate system and represents a node on the ball screw. Since the nut is also modeled as a rigid body, it translates and rotates by amounts, $\mathbf{u}_N$ and $\boldsymbol{\theta}_N$, measured from $P$, respectively. For convenience, $P$ is chosen to coincide with the COM (node) of the nut, since this is where all its inertia properties are lumped. $\mathbf{r}$ is the position vector measured from $P$ to the centre of any of the balls in the interface.

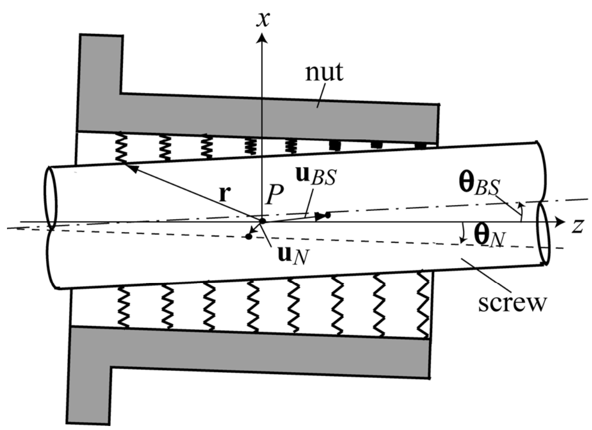


**Figure 3.6: Lumping to Nodes based on Rigid Ball Screw Assumption**

If the coordinate system, $CS_4$, in Figure 3.5, is chosen such that it coincides with $CS$, then the position vector $\mathbf{r}$ for each ball can be expressed as a function of $\phi$ as:

$$\mathbf{r} = \begin{Bmatrix} r_x \\ r_y \\ r_z \end{Bmatrix} = \begin{Bmatrix} R\sin(\phi) \\ -R\cos(\phi) \\ r_g\phi \end{Bmatrix} \tag{3.12}$$

This function is derived from the parametric equation of a helix having a pitch $p$ equal to the pitch of the ball screw. $R$ is the constant radius measured from the axis of the screw to the centre of each ball while $r_g$ is the gear reduction ratio of the ball screw given by:

$$r_g = \frac{p}{2\pi} \tag{3.13}$$

Figure 3.7 shows the relationship among $\mathbf{r}$, $\mathbf{r}_N$ and $\mathbf{r}_{BS}$ for the $L$ and $U$-Configurations. $\mathbf{r}_N$ and $\mathbf{r}_{BS}$ are the position vectors measured from $P$ to the nut-ball and screw-ball contact points, $P_N$ and $P_{BS}$, of each ball, respectively.

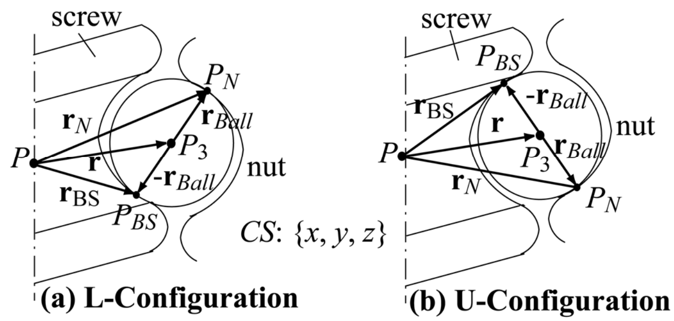


**Figure 3.7: Position Vectors for Ball Contact Points**

If $\mathbf{r}_{Ball}$ is defined as the position vector from the ball's centre, $P_3$, to $P_N$ for the $L$ and $U$-Configurations, then $\mathbf{r}_{BS}$ and $\mathbf{r}_N$ are given by:

$$\mathbf{r}_{BS} = \mathbf{r} - \mathbf{r}_{Ball}; \qquad \mathbf{r}_N = \mathbf{r} + \mathbf{r}_{Ball} \tag{3.14}$$

The vector $\mathbf{r}_{Ball}$ for the $L$ and $U$-Configurations is obtained by transforming the radius of the ball, $R_{Ball}$, to the global coordinates using $\mathbf{T}_{3\text{-}z1L}$ and $\mathbf{T}_{3\text{-}z1U}$, as:

$$\mathbf{r}_{Ball} = \begin{cases} \mathbf{T}_{3-z1L} \cdot R_{Ball} & \text{for the } L\text{-Configuration} \\ \mathbf{T}_{3-z1U} \cdot R_{Ball} & \text{for the } U\text{-Configuration} \end{cases} \tag{3.15}$$

Since the ball screw and nut are considered to be rigid bodies, and the rotations involved in vibratory motions are small, the transformations $\mathbf{T}_{3\text{-}BS}$ and $\mathbf{T}_{3\text{-}N}$ (between the displacements in $CS_3$ and displacements and rotations in $CS$) for the nut and ball screw can then be written as:

$$\mathbf{u}_{3BS} = \underbrace{\begin{bmatrix} \mathbf{I}_{3\times3} & -\mathrm{S}(\mathbf{r}_{BS}) \end{bmatrix}}_{\mathbf{T}_{3\text{-}BS}} \begin{Bmatrix} \mathbf{u}_{BS} \\ \boldsymbol{\theta}_{BS} \end{Bmatrix}; \quad \mathbf{u}_{3N} = \underbrace{\begin{bmatrix} \mathbf{I}_{3\times3} & -\mathrm{S}(\mathbf{r}_N) \end{bmatrix}}_{\mathbf{T}_{3\text{-}N}} \begin{Bmatrix} \mathbf{u}_N \\ \boldsymbol{\theta}_N \end{Bmatrix} \tag{3.16}$$

Here, $\mathbf{u}_{3BS}$ and $\mathbf{u}_{3N}$ are the displacements of $P_{BS}$ and $P_N$ measured in the $CS_3$ coordinate system. S(.) is the operator defined in Eq.(3.4).

Using the transformations, $\mathbf{T}_{3\text{-}BS}$ and $\mathbf{T}_{3\text{-}N}$, displacements at the screw-ball and nut-ball contact points for all balls can be combined into equivalent nodal displacements and rotations at a point $P$ for the ball screw and nut, respectively.

**(B) Shape Function Method**

It was assumed that the section of the ball screw within the screw-nut interface acts as a rigid body in the Rigid Ball Screw method. However, in some cases where the nut is significantly long, for instance in the spacer and offset preload mechanisms [55], this assumption may not be realistic since the ball screw may undergo significant deformations within the screw-nut interface. In such cases, the Shape Function method described in this section provides a more realistic means of lumping the distributed interface stiffness to the ball screw nodes.

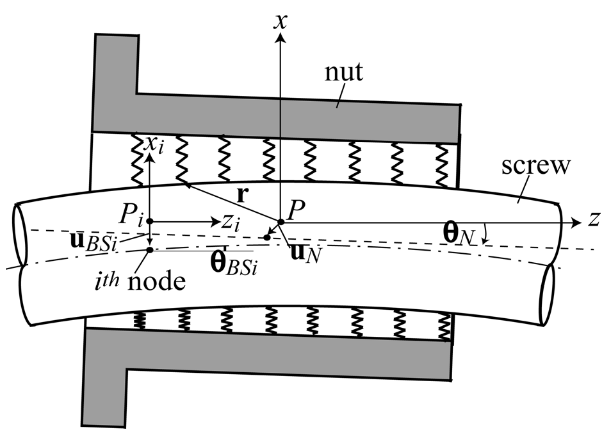


**Figure 3.8: Shape Function Method**

Figure 3.8 gives a pictorial representation of the Shape Function method. As shown, the nut is still assumed to perform a rigid-body translation and rotation, $\mathbf{u}_N$ and $\boldsymbol{\theta}_N$, measured from $P$. However, this time, the deformations of the ball screw at each of its $N_{Node}$ nodes within the screw-nut interface are considered. A new global coordinate system $CS_i$, centered at point $P_i$ (the undeformed location of the $i^{th}$ node of the ball screw) has also been established. Here, $\mathbf{u}_{BSi}$ and $\boldsymbol{\theta}_{BSi}$ are the translational and rotational displacements of the $i^{th}$ node. The goal of the Shape Function method is to lump the global stiffness matrices defined at the center of each ball to each of the $N_{Node}$ nodes of the ball screw within the screw-nut interface.

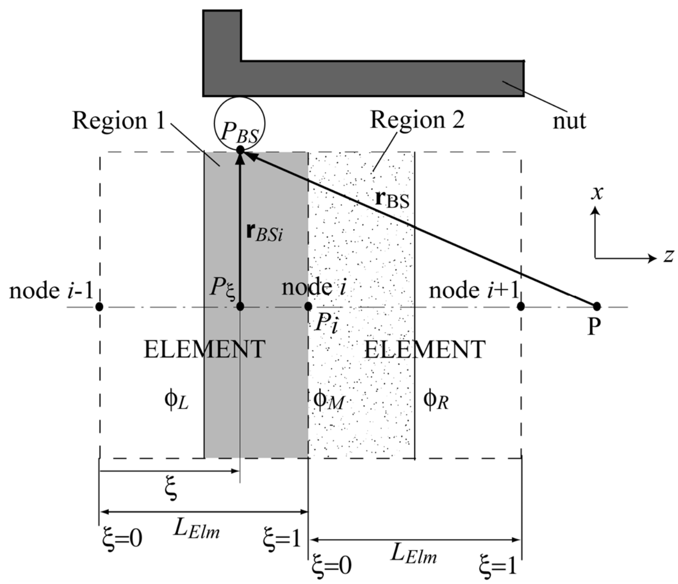


**Figure 3.9: More Details of Shape Function Method**

Figure 3.9 shows a more detailed representation of the method for two adjacent FE beam elements of the ball screw. The coordinate axes have been omitted for clarity. Here, it is assumed, without loss of generality, that the elements within the screw-nut interface have equal lengths, $L_{Elm}$. $\xi$ is the non-dimensional distance measured from the left to the right node of each element such that its value ranges from 0 to 1 for a distance 0 to a distance $L_{Elm}$. The node of interest is labeled as the $i^{th}$ node, while the nodes to its left and right are respectively labeled as the $i$-$1^{th}$ and $i$+$1^{th}$ nodes.

A global coordinate system $CS_\xi$ (not shown in the figure) is established at every point $P_\xi$ along the axis of the ball screw. The displacements $\mathbf{u}_{BS\xi}$ and rotations $\boldsymbol{\theta}_{BS\xi}$ of the ball screw are measured from $CS_\xi$. Furthermore, similar to the coordinate system $CS_i$ established on the $i^{th}$ node, $CS_{i\text{-}1}$ and $CS_{i+1}$ have been established on the $i$-$1^{th}$ and $i$+$1^{th}$ nodes, respectively.

The first step in obtaining the required transformation matrix is to derive a relationship between the displacements ($\mathbf{u}_{3BS}$) at the screw-ball contact point ($P_{BS}$) and the displacements and rotations of the ball screw at each point $P_\xi$ along its axis. This is achieved by assuming that that the cross-section of the ball screw at each $P_\xi$ location translates and rotates as a rigid body about $P_\xi$ by amounts $\mathbf{u}_{BS\xi}$ and $\boldsymbol{\theta}_{BS\xi}$, respectively. This results in the transformation $\mathbf{T}_{3\text{-}BS\xi}$ given by:

$$\mathbf{u}_{3BS} = \underbrace{\left[\mathbf{I}_{3\times3} \quad -\mathrm{S}(\mathbf{r}_{BSi})\right]}_{\mathbf{T}_{3\text{-}BS\xi}} \begin{Bmatrix} \mathbf{u}_{BS\xi} \\ \boldsymbol{\theta}_{BS\xi} \end{Bmatrix} \tag{3.17}$$

The transformation $\mathbf{T}_{3\text{-}N}$ for the nut remains the same as defined in Eq.(3.16). The vector $\mathbf{r}_{BSi}$ in Eq.(3.17) represents the radial position of $P_{BS}$ with respect to $P_\xi$. It is obtained by extracting the $x$ and $y$ components of $\mathbf{r}_{BS}$; i.e.:

$$\mathbf{r}_{BSi} = \begin{bmatrix} 1 & 0 & 0 \\ 0 & 1 & 0 \\ 0 & 0 & 0 \end{bmatrix} \mathbf{r}_{BS} \tag{3.18}$$

$\mathbf{r}_{BS}$ is given in Eq.(3.14).

The next step in the transformation involves deriving a relationship between $CS_\xi$ and the global coordinate systems ($CS_{i-1}$, $CS_i$ and $CS_{i+1}$) attached to the nodes of the ball screw. This is achieved by making use of the shape function matrix for the Timoshenko Beam Element [64][87] given by:

$$\mathbf{T}_{BS\xi\text{-}BSi} = \begin{bmatrix} N_{ux1} & 0 & 0 & 0 & N_{ux2} & 0 & N_{ux3} & 0 & 0 & 0 & N_{ux4} & 0 \\ 0 & N_{uy1} & 0 & N_{uy2} & 0 & 0 & 0 & N_{uy3} & 0 & N_{uy4} & 0 & 0 \\ 0 & 0 & N_{uz1} & 0 & 0 & 0 & 0 & 0 & N_{uz2} & 0 & 0 & 0 \\ 0 & N_{\theta x1} & 0 & N_{\theta x2} & 0 & 0 & 0 & N_{\theta x3} & 0 & N_{\theta x4} & 0 & 0 \\ N_{\theta y1} & 0 & 0 & 0 & N_{\theta y2} & 0 & N_{\theta y3} & 0 & 0 & 0 & N_{\theta y4} & 0 \\ 0 & 0 & 0 & 0 & 0 & N_{\theta z1} & 0 & 0 & 0 & 0 & 0 & N_{\theta z2} \end{bmatrix} \tag{3.19}$$

The elements of the shape function matrix are all functions of $\xi$ and they represent spatial interpolation functions from displacements and rotations at the two nodes of an FE beam element to displacements and rotations anywhere within the element. The expressions for these functions are provided in Appendix A.

The shape function matrix of Eq.(3.19) is defined only within the boundaries of a given element. It cannot be used across element boundaries. Therefore, the region around each node is divided into two, as shown in Figure 3.9. Region 1 is the portion to the left of the $i^{th}$ node up to halfway into the element on its left, while Region 2 is the portion on its right up to halfway into the element on the right. These two regions have to be considered separately in the analysis.

Region 1 is bounded by the azimuth angles $\phi_L$ and $\phi_M$ while Region 2 is bounded by $\phi_M$ and $\phi_R$. Within these bounds, the relationship between $\xi$ and $\phi$ is given by the linear function:

$$\xi = m\phi + c; \qquad m = \frac{1}{\phi_R - \phi_L} \tag{3.20}$$

The constant $c$ depends on the region of interest according the following relationships:

$$c = \begin{cases} 0.5 - m\phi_L & \text{for Region 1} \\ 0.5 - m\phi_R & \text{for Region 2} \end{cases} \tag{3.21}$$

Since the shape function matrix is only valid for the nodes of a particular element, in Region 1, it a transformation from $CS_{i\text{-}1}$ and $CS_i$ to $CS_\xi$ while in Region 2 it is from $CS_i$ and $CS_{i+1}$ to $CS_\xi$. Mathematically this is expressed as:

$$\begin{aligned} \begin{Bmatrix} \mathbf{u}_{BS\xi} \\ \boldsymbol{\theta}_{BS\xi} \end{Bmatrix} &= \mathbf{T}_{BS\xi\text{-}BSi} \begin{Bmatrix} \mathbf{u}_{BSi-1} \\ \boldsymbol{\theta}_{BSi-1} \\ \mathbf{u}_{BSi} \\ \boldsymbol{\theta}_{BSi} \end{Bmatrix} \qquad \text{for Region 1} \\ \begin{Bmatrix} \mathbf{u}_{BS\xi} \\ \boldsymbol{\theta}_{BS\xi} \end{Bmatrix} &= \mathbf{T}_{BS\xi\text{-}BSi} \begin{Bmatrix} \mathbf{u}_{BSi} \\ \boldsymbol{\theta}_{BSi} \\ \mathbf{u}_{BSi+1} \\ \boldsymbol{\theta}_{BSi+1} \end{Bmatrix} \qquad \text{for Region 2} \end{aligned} \tag{3.22}$$

Hence the transformation between $CS_3$ and the node-centered global coordinate systems $CS_{i\text{-}1}$, $CS_i$ and $CS_{i+1}$ for the ball screw is given by:

$$\mathbf{u}_{3BS} = \underbrace{\begin{bmatrix} \mathbf{T}_{3-BS\xi} \cdot \mathbf{T}_{BS\xi-BSi} & \mathbf{0}_{3\times6} \end{bmatrix}}_{\mathbf{T}_{3\text{-}BSi}} \cdot \begin{Bmatrix} \mathbf{u}_{BSi-1} \\ \boldsymbol{\theta}_{BSi-1} \\ \mathbf{u}_{BSi} \\ \boldsymbol{\theta}_{BSi} \\ \mathbf{u}_{BSi+1} \\ \boldsymbol{\theta}_{BSi+1} \end{Bmatrix} \qquad \text{for Region 1}$$

$$\mathbf{u}_{3BS} = \underbrace{\begin{bmatrix} \mathbf{0}_{3\times6} & \mathbf{T}_{3-BS\xi} \cdot \mathbf{T}_{BS\xi-BSi} \end{bmatrix}}_{\mathbf{T}_{3\text{-}BSi}} \cdot \begin{Bmatrix} \mathbf{u}_{BSi-1} \\ \boldsymbol{\theta}_{BSi-1} \\ \mathbf{u}_{BSi} \\ \boldsymbol{\theta}_{BSi} \\ \mathbf{u}_{BSi+1} \\ \boldsymbol{\theta}_{BSi+1} \end{Bmatrix} \qquad \text{for Region 2} \tag{3.23}$$

Though these transformations are functions of both $\phi$ and $\xi$, they can easily be transformed into functions of $\phi$ using the linear relationship between $\xi$ and $\phi$ derived in Eq.(3.20).

### 3.3.4 Derivation of Stiffness Matrix

After the necessary transformations between the ball-centered local coordinate system $z_1$ aligned in the direction of $k_{Ball}$, and the node-centered global coordinate systems have been obtained, the derivation of the interface stiffness matrix is obtained as follows.

The stiffness matrix in the $k_{Ball}$ direction between the screw-ball and nut-ball contact points, $P_{BS}$ and $P_N$ (see Figure 3.7) is given by:

$$\mathbf{K}_{Ball} = k_{Ball} \cdot \begin{bmatrix} 1 & -1 \\ -1 & 1 \end{bmatrix} \tag{3.24}$$

Based on the Rigid Ball Screw method, the transformation matrix between the displacements at $P_{BS}$ and $P_N$ in the $z_1$ coordinate direction, and the displacements and rotations at the screw's node and nut's node is expressed for the $L$-Configuration as:

$$\mathbf{T}_{z1L-BS} = \mathbf{T}_{z1L-3} \cdot \mathbf{T}_{3-BS}; \quad \mathbf{T}_{z1L-N} = \mathbf{T}_{z1L-3} \cdot \mathbf{T}_{3-N} \tag{3.25}$$

Similarly, for the $U$-Configuration, the transformations are given by:

$$\mathbf{T}_{z1U-BS} = \mathbf{T}_{z1U-3} \cdot \mathbf{T}_{3-BS}; \quad \mathbf{T}_{z1U-N} = \mathbf{T}_{z1U-3} \cdot \mathbf{T}_{3-N} \tag{3.26}$$

As explained in Section 3.3.3, in the calculation of the $\mathbf{r}_{Ball}$ used in $\mathbf{T}_{3\text{-}BS}$ and $\mathbf{T}_{3\text{-}N}$, the contact configuration of the ball must also be taken into account.

The combined transformation matrix for the ball screw and nut is given by the block diagonal matrix, $\mathbf{T}_{z1L\text{-}BSN}$, for the $L$-Configuration and $\mathbf{T}_{z1U\text{-}BSN}$ for the $U$-Configuration. Mathematically, this is expressed as:

$$\mathbf{T}_{z1L-BSN} = \begin{bmatrix} \mathbf{T}_{z1L-BS} & \mathbf{0}_{1\times6} \\ \mathbf{0}_{1\times6} & \mathbf{T}_{z1L-N} \end{bmatrix}; \quad \mathbf{T}_{z1U-BSN} = \begin{bmatrix} \mathbf{T}_{z1U-BS} & \mathbf{0}_{1\times6} \\ \mathbf{0}_{1\times6} & \mathbf{T}_{z1U-N} \end{bmatrix} \tag{3.27}$$

The screw-nut interface stiffness matrices for each ball as a function of the azimuth angle $\phi$ are calculated by transforming $\mathbf{K}_{Ball}$. These matrices $\mathbf{K}_L$ and $\mathbf{K}_U$, for the $L$ and $U$-Configurations, respectively, are given by:

$$\mathbf{K}_L = \mathbf{T}^T_{z1L-BSN} \cdot \mathbf{K}_{Ball} \cdot \mathbf{T}_{z1L-BSN}; \quad \mathbf{K}_U = \mathbf{T}^T_{z1U-BSN} \cdot \mathbf{K}_{Ball} \cdot \mathbf{T}_{z1U-BSN} \tag{3.28}$$

Since these stiffness matrices have all been transformed into the same coordinate systems for all the balls, they can be combined by averaging each matrix over the whole motion range for the ball concerned, and then adding them all algebraically.

$$\mathbf{K}_{SN} = \sum_{k=1}^{N_{Ball}} \left( \frac{1}{\phi_{k,end} - \phi_{k,st}} \int_{\phi_{k,st}}^{\phi_{k,end}} \mathbf{K}_{L/U}(\phi) d\phi \right) \tag{3.29}$$

where $\mathbf{K}_{SN}$ is the interface stiffness matrix and $N_{Ball}$ is the total number of balls in the interface, while $\phi_{k,st}$ and $\phi_{k,end}$ are the azimuth angles of $k^{th}$ ball at the beginning and end of its motion range. The notation $\mathbf{K}_{L/U}$ is used to indicate a choice between $\mathbf{K}_L$ and $\mathbf{K}_U$ depending on the contact configuration of the $k^{th}$ ball.

For the Shape Function method, the derivation follows the same sequence described for the Rigid Ball Screw method above. To avoid repetition here, the derivations will be shown for only the $L$-configuration. For the $U$-Configuration, all that needs to be changed are the subscripts from $L$ to $U$.

The transformation between the displacements at the contact points $P_N$ and $P_{BS}$ expressed for the Rigid Body method in Eq.(3.25) becomes:

$$\mathbf{T}_{z1L-BSi} = \mathbf{T}_{z1L-3} \cdot \mathbf{T}_{3-BSi}; \quad \mathbf{T}_{z1L-N} = \mathbf{T}_{z1L-3} \cdot \mathbf{T}_{3-N} \tag{3.30}$$

for the Shape Function method. Notice that the transformation for the nut remains the same. This is because the nut is still assumed to be a rigid-body in the Shape Function method.

The block diagonal matrix for the combined transformation in this case is given by:

$$\mathbf{T}_{z1L-BSiN} = \begin{bmatrix} \mathbf{T}_{z1L-BSi} & \mathbf{0}_{1\times 6} \\ \mathbf{0}_{1\times 18} & \mathbf{T}_{z1L-N} \end{bmatrix} \tag{3.31}$$

Using this, the $i^{th}$-node interface stiffness for each ball is obtained as:

$$\mathbf{K}_{Li} = \mathbf{T}_{z1L-BSiN}^{T} \cdot \mathbf{K}_{Ball} \cdot \mathbf{T}_{z1L-BSiN} \tag{3.32}$$

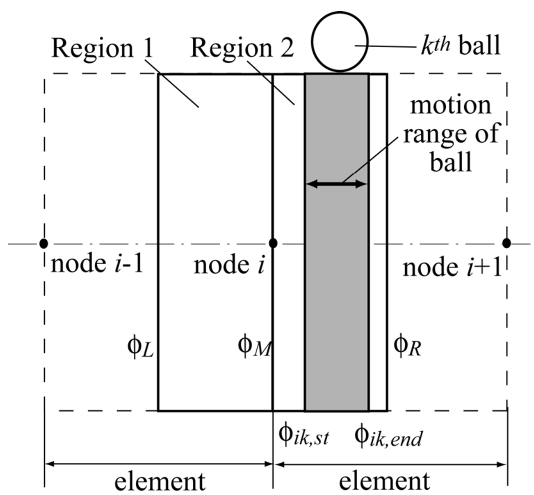


**Figure 3.10: Integration Limits for Region 1 and Region 2**

If $\phi_{ki,st}$ and $\phi_{ki,end}$ are used to represent the azimuth angles at the beginning and end of the motion path of the $k^{th}$ ball within the region around the $i^{th}$ node (Figure 3.10) then the stiffness matrix for the $i^{th}$ node is obtained as:

$$\mathbf{K}_{SNi} = \sum_{k=1}^{N_{Balli}} \left( \frac{1}{\phi_{ik,end} - \phi_{ik,st}} \left( \begin{array}{l} \kappa_1 \left( \int_{\phi_{ik,st}}^{\phi_{ik,end}} \mathbf{K}_{Li/UiR2}(\phi) d\phi \right) + \kappa_2 \left( \int_{\phi_{ik,st}}^{\phi_{ik,end}} \mathbf{K}_{Li/UiR1}(\phi) d\phi \right) + \ldots \\ \kappa_3 \left( \int_{\phi_{ik,st}}^{\phi_M} \mathbf{K}_{Li/UiR1}(\phi) d\phi + \int_{\phi_M}^{\phi_{ik,end}} \mathbf{K}_{Li/UiR2}(\phi) d\phi \right) \end{array} \right) \right) \tag{3.33}$$

Here, $K_{SNi}$ is the interface stiffness connecting the $i$-$1^{th}$, $i^{th}$ and $i$+$1^{th}$ nodes on the ball screw to the nut node while $N_{Balli}$ is the number of balls in the region around the $i^{th}$ node. Again, the subscript $Li/Ui$ in $\mathbf{K}_{Li/UiR1}$ and $\mathbf{K}_{Li/UiR2}$ indicates a choice between the $L$ and $U$ configurations depending on the nature of the ball's contact. The additional subscripts $R_1$ and $R_2$ indicate whether the stiffness matrix is derived based on the transformations for Region 1 or Region 2. $\kappa_1$, $\kappa_2$ and $\kappa_3$ are binary switching functions defined as:

$$\kappa_1 = \begin{cases} 1 & \text{if } \phi_M \le \phi_{ik,st} < \phi_{ik,end} \le \phi_R \\ 0 & \text{otherwise} \end{cases}; \quad \kappa_2 = \begin{cases} 1 & \text{if } \phi_L \le \phi_{ik,st} < \phi_{ik,end} \le \phi_M \\ 0 & \text{otherwise} \end{cases}$$
$$\kappa_3 = \begin{cases} 1 & \text{if } \phi_L \le \phi_{ik,st} < \phi_{ik,end} \le \phi_R \\ 0 & \text{otherwise} \end{cases} \tag{3.34}$$

Each of the $N_{Node}$ nodes within the screw-nut interface has its own $K_{SNi}$ matrix and each matrix is derived following the steps explained above.

As can be seen, the Rigid Ball Screw method requires fewer computations than the Shape Function method. It is therefore necessary to know when the Rigid Ball Screw method is a preferable choice over the Shape Function Method. The case study in Appendix B shows that the Rigid Ball Screw method gives similar simulation results as the Shape Function method for short nuts. However, as the length of the nut increases, the predictions of the two models become markedly different. Therefore, by way of recommendation, it is better to consider using the Rigid Body method for short nuts and more rigid ball screws and to use the Shape Function method for long nuts and less rigid ball screws.

### 3.3.5 Determination of Ball Stiffness

The ball stiffness $k_{Ball}$ is not usually provided in manufacturers' catalogs. However, a value is often provided for the axial stiffness of the screw-nut interface, $k_{Ax}$. This value can be used to calculate $k_{Ball}$ by noting that, based on the geometrical transformations described above, the direct stiffness in the axial direction always turns out to be:

$$k_{Ax} = k_{Ball} N_{Ball} \cos^2 \alpha \cos^2 \beta \tag{3.35}$$

Consequently, given $\alpha$, $\beta$ and $N_{Ball}$, $k_{Ball}$ can easily be calculated from $k_{Ax}$.

### 3.3.6 Characteristics of Stiffness Matrix

The general structure of the first six rows and columns of the interface stiffness matrix, $\mathbf{K}_{SN}$, is given in Eq.(3.36). As seen from the matrix, in addition to the direct stiffness terms (on the main diagonal) and the cross-coupling term between the axial and torsional directions ($k_{z,\theta z}$), the proposed model also contains cross-coupling terms between the two lateral planes ($k_{x,\theta x}$ and $k_{y,\theta y}$) and between the lateral, torsional and axial directions ($k_{x,z}$, $k_{x,\theta z}$, $k_{z,\theta x}$, $k_{\theta x,\theta z}$) which are not found in other models (e.g. [88]). The implication of these extra cross-coupling terms is that, for instance, a torque applied to the motor can create torsional, axial and lateral displacements on the ball screw which can then affect the positioning of the table and fatigue life of the ball screw.

$$\mathbf{K}_{SN1-6,1-6} = \begin{bmatrix} k_{x,x} & & & & & \\ 0 & k_{y,y} & & & \text{Sym} & \\ k_{x,z} & 0 & k_{z,z} & & & \\ k_{x,\theta x} & 0 & k_{z,\theta x} & k_{\theta x,\theta x} & & \\ 0 & k_{y,\theta y} & 0 & 0 & k_{\theta y,\theta y} & \\ k_{x,\theta z} & 0 & k_{z,\theta z} & k_{\theta x,\theta z} & 0 & k_{\theta z,\theta z} \end{bmatrix} \tag{3.36}$$

In the original model presented in [54], the $k_{x,\theta z}$ and the $k_{x,z}$ terms of $\mathbf{K}_{SN1\text{-}6,1\text{-}6}$ were indicated as equal to zero. But a careful analysis of the theoretical formulations revealed that these terms are zero only for special combinations of the geometric parameters of the model. In the general case, however, these terms are non-zero as indicated in the updated model of Eq.(3.36).

It is also worth mentioning here that the same characteristics discussed above for $\mathbf{K}_{SN}$ are exhibited by $\mathbf{K}_{SNi}$. Therefore, $\mathbf{K}_{SNi}$ has not been given any special consideration in this subsection.

## 3.4 Analysis of Open-Loop Dynamics of a Single-Axis Ball Screw Drive Test Bed

The finite element modeling technique presented in Sections 3.2 and 3.3 is used to model a single-axis ball screw drive test bed and relevant information about the open-loop dynamics of the drive is extracted. Experimental measurements of the same open-loop dynamics are also acquired from the drive. By comparing and contrasting the simulated and measured results, a clearer understanding and a more accurate characterization of the drive's dynamics are obtained.

### 3.4.1 Description of Single-Axis Ball Screw Drive Test Bed

The single-axis ball screw drive test bed (hereinafter referred to as *test bed*) used for model verification and analysis purposes is shown in Figure 3.11(a). It consists of a 20 [mm] diameter ball screw constrained axially on the end closer to the motor (proximal end) by a thrust bearing. The end farther from the motor (distal end) is constrained using a radial ball bearing. It is driven by a brushless DC motor connected to the ball screw via a bellow-type coupling. Position measurement is obtained via three high-resolution encoders – two rotary encoders (each with 0.1 [μm] resolution) at either end of the ball screw and a linear encoder (with 0.05 [μm] resolution) mounted to the table. It is also furnished with a tachometer attached to its distal end. The test bed can achieve velocities of up to 27 [m/min] and accelerations reaching 1 [g] over a stroke of about 360 [mm].

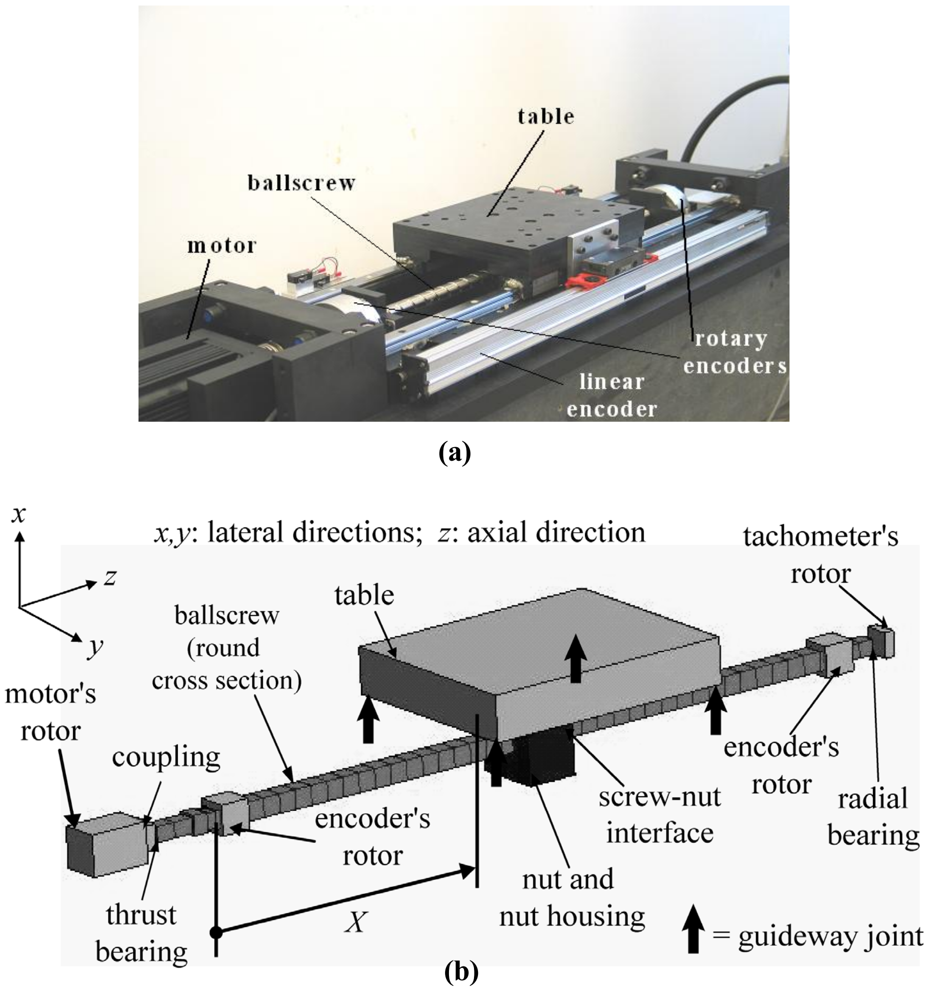


**Figure 3.11: (a) Test Bed – Single-Axis Ball Screw Drive (b) Schematic Representation of Test Bed Model**

Figure 3.11(b) shows a schematic representation of the model of the test bed built using the technique described in Sections 3.2 and 3.3. The screw-nut interface is modeled using the Rigid Ball Screw method because the nut is short (i.e. $L_{Nut}$=30 [mm]). The parameters used in the model are either obtained from the manufacturers' catalogs, approximated from prior knowledge or calculated from computer-aided design (CAD) models of the drive components as listed in Table 3.2 and Table 3.3.

| Parameter | Value |
|---|---|
| Table mass [kg] | 20 |
| Diameter and pitch of ball screw [mm] | 20 |
| Inertia of motor's rotor [kgm$^2$] | 9.65x10$^{-5}$ |
| Inertia of encoder's rotor [kgm$^2$] | 8.5x10$^{-5}$ |
| Torsional stiffness of coupling [Nm/rad] | 6500 |
| Lateral stiffness of guideway joints [N/m] | 1.86x10$^8$ |
| Vertical stiffness of guideway joints [N/m] | 1.37x10$^8$ |
| Axial stiffness of thrust bearing [N/m] | 1.13x10$^8$ |
| Radial Stiffness of thrust bearing [N/m] | 1.0x10$^8$ |
| Rotational stiffness of thrust bearing [Nm/rad] | 6000 |
| Radial stiffness of radial ball bearing [N/m] | 5.0x10$^7$ |

**Table 3.2: General Parameters of the Single-Axis Ball Screw Drive Test Bed**

| Screw-Nut Interface Parameter | Value |
|---|---|
| $k_{Ax}$ [N/m] | 1.37x10$^8$ |
| $\alpha$ [degrees] | 17.7 |
| $\beta$ [degrees] | 75 |
| $N_{Ball}$ | 7 |
| $R_{Ball}$ [mm] | 3.969 |
| $R$ [mm] | 10 |
| $\phi_{k,st}$ [degrees] | -270 |
| $\phi_{k,end}$ [degrees] | 270 |

**Table 3.3: Screw-Nut Interface Parameters of Test Bed**

### 3.4.2 Measurement/Simulation of Open-Loop Frequency Response Functions

Three characteristic frequency response functions (FRF) are measured from the test bed with the position and velocity closed-loop controllers turned off. The first is the FRF between a torque applied to the motor through the amplifier and the angular displacements measured from the motor shaft. This FRF represents the open-loop (OL) dynamics of the drive when position measurements are taken from the encoder mounted on the motor shaft. The second FRF is measured between the applied motor torque and the axial displacement of the table. It shows the OL dynamics of the drive when position measurements are taken from the linear encoder mounted on the table. The third FRF, representing the OL disturbance dynamics of the drive, is measured between an impact force applied at the table (in the direction of motion of the table) and axial displacement measurements obtained from the table. The impact force was generated using an instrumented modal testing hammer. To investigate the variation in dynamics as the table moves along the ball screw, each of these FRFs are measured at three distinct positions of the table within its travel range (i.e. $X$ = 30 [mm] to $X$ = 390 [mm] in Figure 3.11(b)):

a) Position 1: Table closest to the motor (i.e. around $X$ = 30 [mm])
b) Position 2: Table at the middle of its travel range (i.e. around $X$ = 210 [mm])
c) Position 3: Table farthest away from the motor (i.e. around $X$ = 390 [mm])

The bandwidth of the drive's amplifier is 950 [Hz], therefore a frequency range of up to 1000 [Hz] is considered as the frequency range of interest for all of the measurements taken. Beyond this frequency range, the motor torque generated through the amplifier is severely attenuated and the measurements are corrupted.

The same FRFs measured from the test bed are also simulated using the model described in Sections 3.2 and 3.3 and the results are compared in Figures 3.12 to 3.14 and in Table 3.4.

| Position | Mode 1 [Hz] | | | Mode 2 [Hz] | | | Mode 3 [Hz] | | |
|---|---|---|---|---|---|---|---|---|---|
| | Sim. | Mea. | Err [%] | Sim. | Mea. | Err [%] | Sim. | Mea. | Err [%] |
| **Pos. 1** | 292 | 237 | 23.2 | 624 | 610 | 2.3 | 816 | 738 | 10.6 |
| **Pos. 2** | 267 | 228 | 17.1 | 629 | 613 | 2.6 | 813 | 728 | 11.7 |
| **Pos. 3** | 250 | 218 | 14.6 | 636 | 619 | 2.7 | 812 | 725 | 12.0 |

**Table 3.4: Comparison of Measured and Simulated Natural Frequencies of the Three Modes in the Open-Loop Dynamics of the Test Bed**

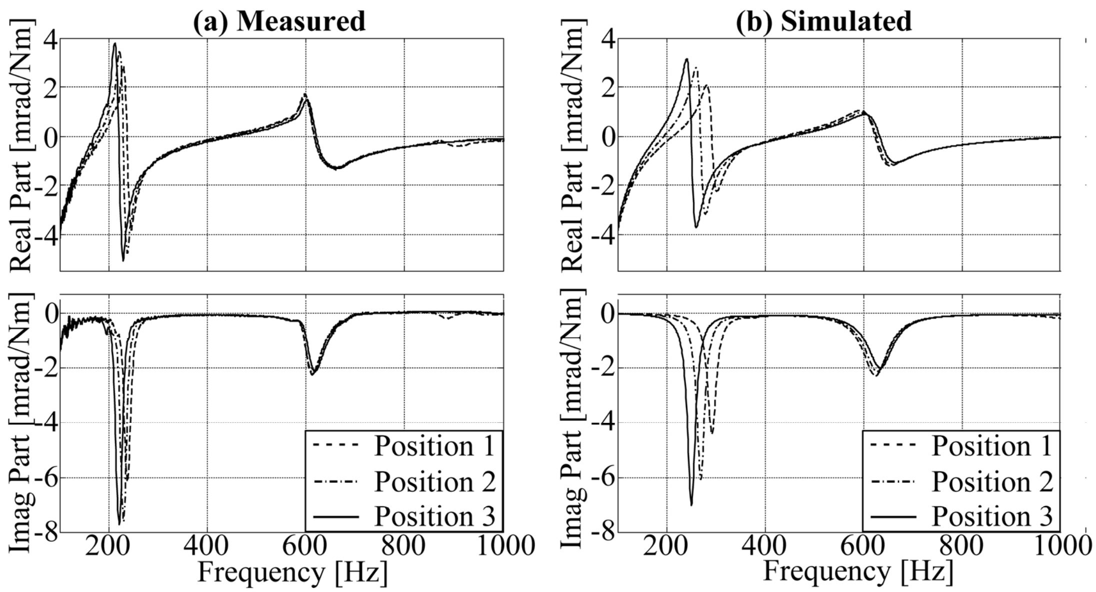


**Figure 3.12: (a) Measured (b) Simulated FRF between a Torque Applied to the Motor and the Angular Displacement of the Motor at Three Positions of the Table within its Travel Range**

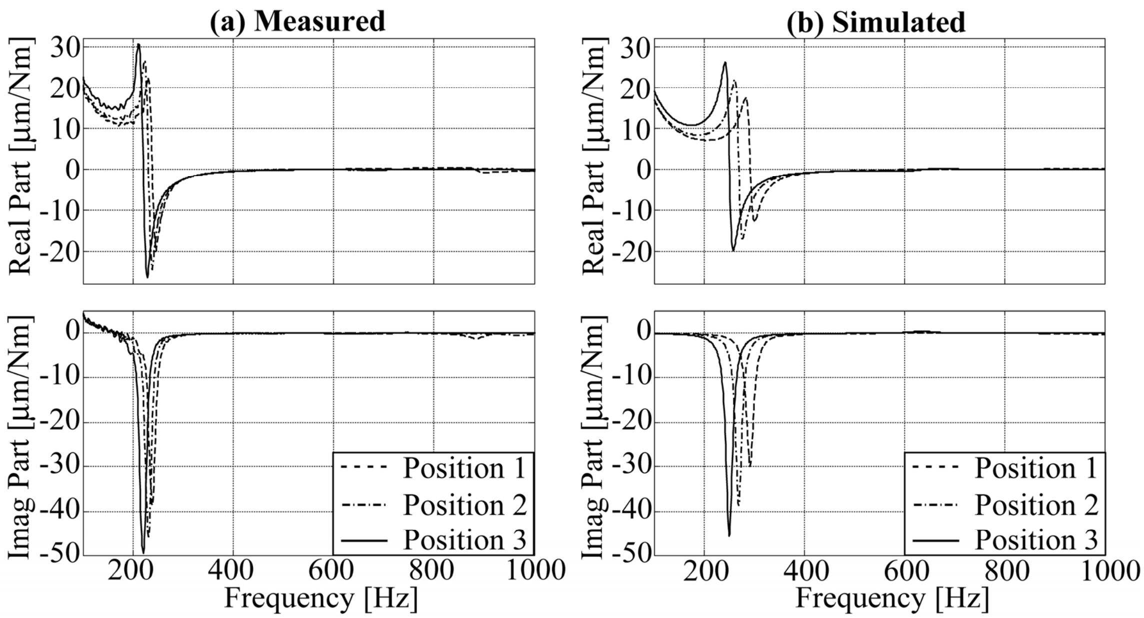


**Figure 3.13: (a) Measured (b) Simulated FRF between a Torque Applied to the Motor and the Axial Displacement of the Table at Three Positions of the Table within its Travel Range**

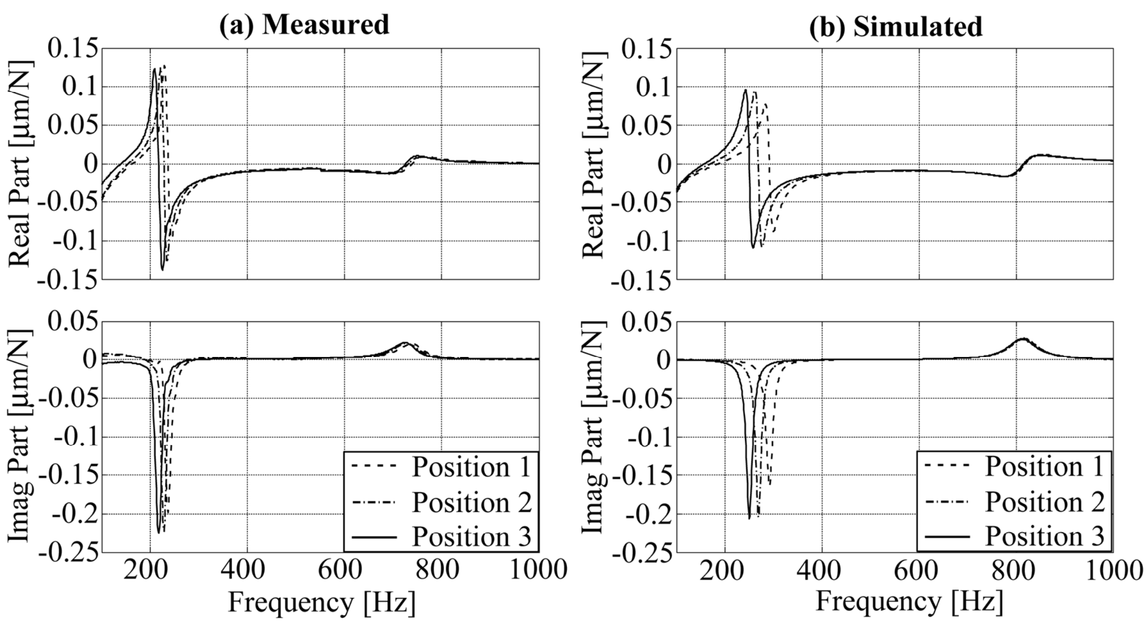


**Figure 3.14: (a) Measured (b) Simulated FRF between a Force Applied to the Table in the Axial Direction and the Axial Displacement of the Table at Three Positions of the Table within its Travel Range**

From the simulated FRFs (Figure 3.12(b) to Figure 3.14(b)) it is seen that the model captures the qualitative behavior of all three modes correctly. It is able to accurately predict the relative amplitudes and natural frequencies of the modes and the way they vary as the table travels along the ball screw. However, it shows some errors in predicting the exact natural frequencies of the modes (shown in Table 3.4) as well as the exact amplitudes of the modes (as seen from the figures). These prediction errors are mainly due to the inaccuracies in the joint stiffness values obtained from manufacturers' catalogs [29][79]. As explained in Varanasi et al [79], the accuracy of the model can be improved by measuring the bearing/housing stiffness experimentally. But even with the experimentally tuned parameters, the prediction errors do not vanish, they only reduce. Since the aim of the finite element analysis performed in this thesis is not to replace the experimental measurements but to complement them, it is sufficient that the model provide a reasonable idea of the behavior of the actual system. Therefore, no extra effort has been put into measuring each of the joint stiffnesses experimentally. Instead, a method for accurately extracting the mass, damping and stiffness matrices of the drive from experimental measurements is put forward in Section 3.5.

### 3.4.3 Analysis of Mode Shapes using Simulation Model

In order to gain better insight into the behavior of the aforementioned modes, it is useful to study their mode shapes. However, it is impractical to experimentally measure the full mode shapes of the ball screw assembly. This is partly because the table moves along the screw and covers a large portion of it thereby reducing the number of available measurement/excitation locations. More importantly, the complex nature of the ball screw's vibrations (i.e. involving stretching, twisting and bending along its entire length) makes it difficult to get a good idea of the mode shapes of the ball screw based on a few measurement/excitation locations/directions. However, since the mode shapes are indicators of the qualitative behavior of the modes, the finite element model is instrumental in understanding the behavior of these modes.

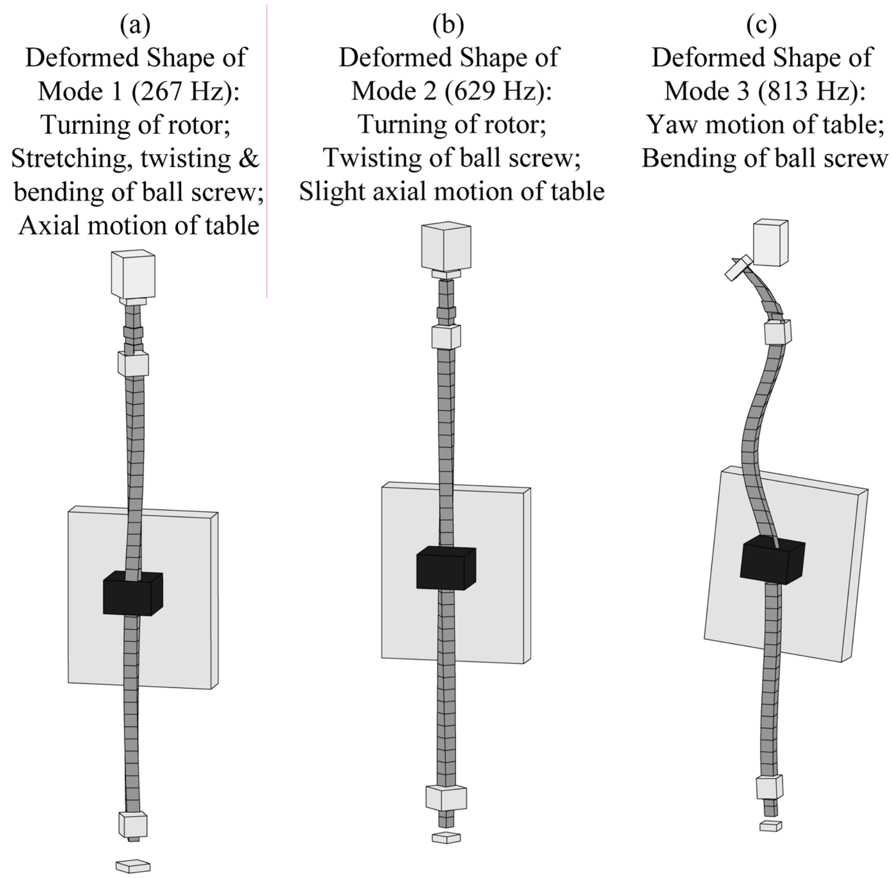


**Figure 3.15: Simulated Deformed Shapes of the Three Modes of the Test Bed with Table at the Middle of its Travel Range (i.e. Position 2)**

Figure 3.15 shows the simulated mode shapes of all three modes of the test bed at a sample position of the table (i.e. at Position 2 with the table located at the middle of its travel range). Using the information gleaned from these simulated mode shapes coupled with observations from measured/simulated FRFs, a detailed analysis of the three modes is presented here.

**Mode 1: Mode Simulated around 267 Hz (Measured around 228 Hz)**

This particular mode is well known to occur in ball screw drives, as observed by other researchers as well [28][29][40][54][70][79]. In their studies they describe this mode as a coupled axial-torsional mode of the ball screw which causes axial displacements (vibrations) of the table. They have not reported any lateral vibration effects in the behavior of this mode.

However, as shown in Figure 3.15(a), the proposed finite element model reveals that Mode 1 is characterized by rotation of the motor's rotor together with coupled axial, torsional and lateral deformations of the ball screw. As a result of these motions, axial displacements at the table occur. This additional lateral vibration component predicted by the proposed model is as a result of characteristics of the screw-nut interface stiffness matrix derived in Section 3.3. As discussed in Section 3.3.6, the proposed screw-nut interface stiffness matrix contains extra cross-coupling (CC) terms ($k_{x,\theta x}$, $k_{y,\theta y}$, $k_{x,z}$, $k_{x,\theta z}$, $k_{z,\theta x}$ and $k_{\theta x,\theta z}$) which couple the axial, torsional and lateral vibrations of the ball screw shaft. The influence of these extra cross-coupling terms on Mode 1 can be seen by comparing the mode shape obtained with the proposed model, which contains the aforementioned cross-coupling terms, to that obtained with the cross-coupling terms removed (i.e. $k_{x,\theta x}= k_{y,\theta y}= k_{x,z}= k_{x,\theta z}= k_{z,\theta x}= k_{\theta x,\theta z}=0$).

Figure 3.16 shows a comparison of the (slightly exaggerated) shape of Mode 1 with and without the extra cross-coupling terms. As seen, when the cross-coupling terms are removed, the lateral deformation of the mode disappears and the ball screw's vibrations become purely axial-torsional as observed by other researchers.

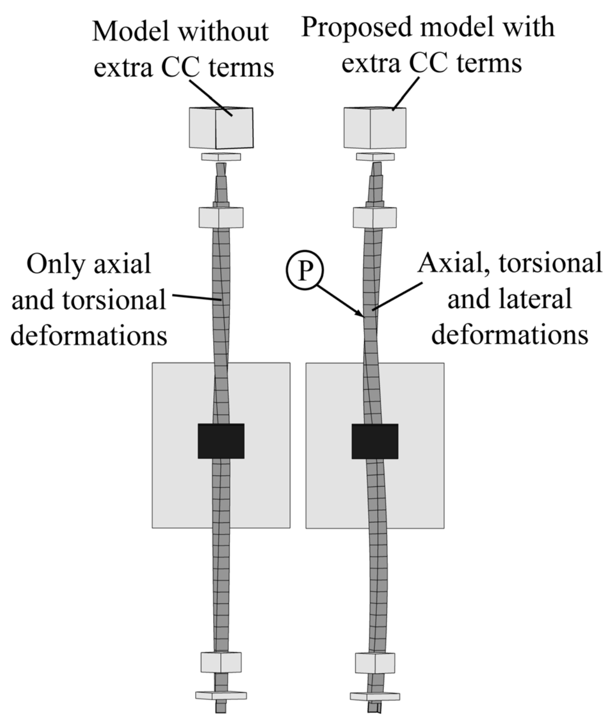


**Figure 3.16: Comparison of Shape of Mode 1 Generated using Proposed Model with Extra Cross-Coupling (CC) Terms and Model without Extra CC Terms**

To further investigate this effect, a simulated FRF is generated by applying a torque to the motor and obtaining the lateral displacement of the ball screw at the point marked as "P" in Figure 3.16. As shown in Figure 3.17(a), the proposed model predicts that the torsional excitation of the motor excites the lateral vibrations of three modes – Mode 1 (at 267 [Hz]) and two other modes – Mode A at 338 [Hz] and Mode B at 401 [Hz]. However, the model without the cross-coupling terms indicates that none of these modes vibrate in the lateral direction as a result of a torsional excitation of the motor. According to the model without the cross-coupling terms, Mode 1 is a purely axial-torsional mode which is completely decoupled from the other two modes which are purely lateral modes. The measured FRF (Figure 3.17(b)) between a torque applied to the motor and lateral displacement of the actual ball screw at point "P" confirms the prediction of the proposed model, indicating that there is a coupling between axial/torsional and lateral vibrations in these modes. The simulated shapes of the other two modes, using the proposed model, are shown in Figure 3.18. They both involve the turning of the motor (due to the coupling joint between the motor and the ball screw shaft) and lateral vibrations of the screw; no significant axial vibrations of the table occur as a result of them.

**(a) Simulated**

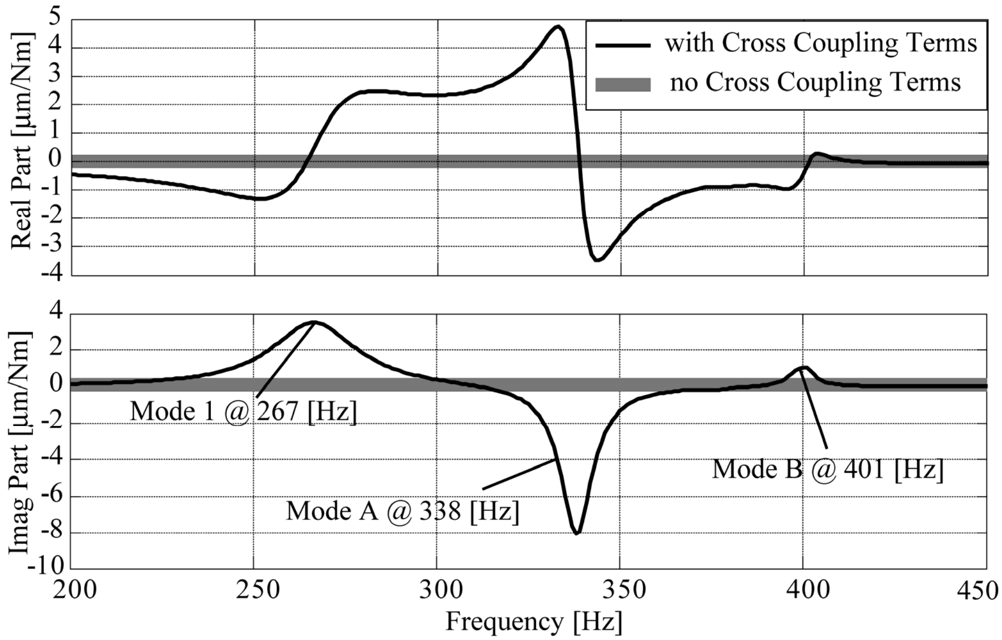


**(b) Measured**

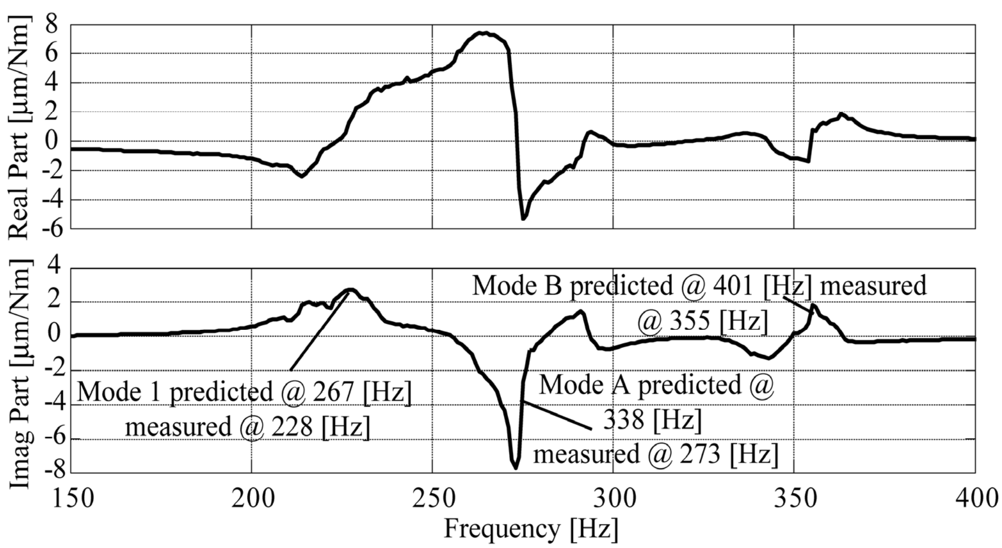


**Figure 3.17: (a) Simulated (b) Measured FRF between Torque Applied to Motor and Lateral Displacement of Point "P" (see Figure 3.16) on Ball Screw. FRFs are obtained with Table at Position 2**

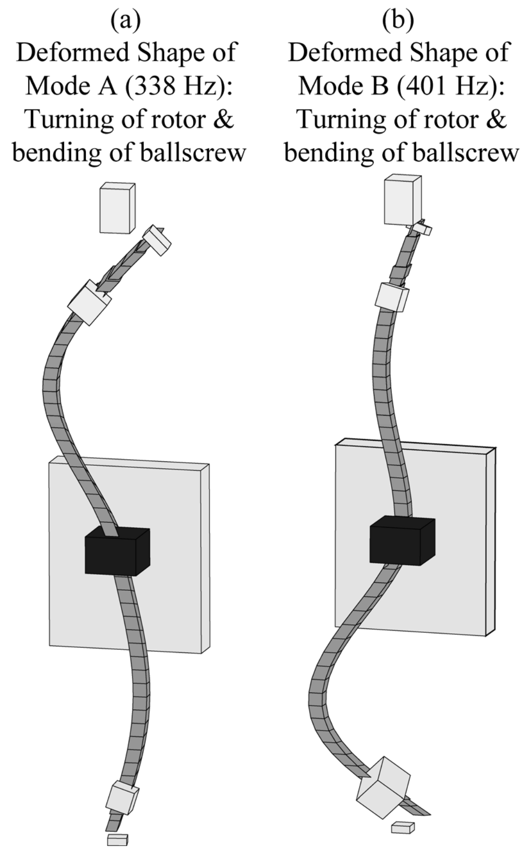


**Figure 3.18: Simulated Deformed Shapes of Mode A and Mode B with Table at the Middle of its Travel Range (i.e. Position 2)**

From the preceding investigations, it is evident that the ball screw stretches, twists and bends when a torque is applied to the motor around the natural frequency of Mode 1. But from the controller design stand point, it is of interest to know if the bending of the ball screw actually influences the positioning of the table. To explore this possibility, the FRF of Figure 3.13 (between the motor torque and axial displacement of the table) is simulated and measured at various positions ($X$) of the table along the ball screw. The positions of the table are referenced from the beginning of the threaded section of the ball screw as shown in Figure 3.11(b). The natural frequencies, vibration amplitudes and the table's normalized modal displacements are measured and simulated at these different positions. In the simulated plot (Figure 3.19(a)), when the cross-coupling terms are neglected, the table position is affected only by the torsional-axial vibrations of the ball screw. The torsional-axial vibrations of Mode 1 exhibit decreasing modal stiffness as the table moves away from the motor. Consequently, the natural frequency of Mode 1 decreases steadily as the table moves away from the motor while the table's vibration amplitude follows the reverse pattern. However, when the cross-coupling terms are considered, as also indicated by the experiments, the lateral vibrations create two sudden drops in amplitude at locations around $X$ = 150 [mm] and $X$ = 300 [mm]. It is also observed that the lateral vibrations do not alter the natural frequency variation in any significant way but it affects the modal displacement of the table considerably.

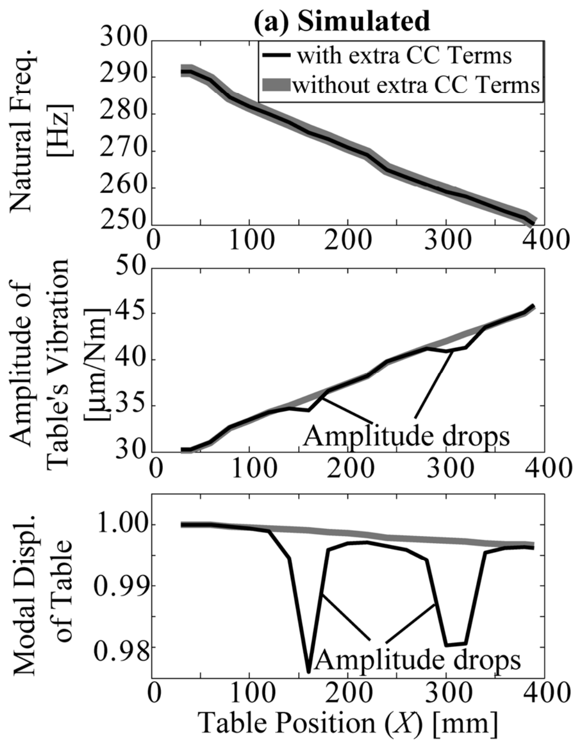


**Figure 3.19: (a) Simulated (b) Measured Variation of Natural Frequency, Vibration Amplitude and Table's (Normalized) Modal Displacement due to Mode 1 as Table moves within its Travel Range. Simulations are performed with and without the extra Cross-Coupling (CC) Terms**

This phenomenon can be understood by studying the simulated interaction between Mode 1 and the other two lateral modes (i.e. Mode A and Mode B) as the table moves along the ball screw. It is observed that when the table is at the proximal end (i.e. at $X$ = 30 [mm]), Mode A starts out at 175 [Hz] while Mode B starts at 545 [Hz]. As the table moves towards the distal end (i.e. $X$ = 390 [mm]), the natural frequency of Mode A increases steadily while that of Mode B decreases. Finally, when the table reaches the distal end, Mode A's natural frequency becomes 512 [Hz] while Mode B's becomes 199 [Hz]. The table locations $X$ = 160

[mm] and $X$ = 300 [mm] respectively correspond to the points where natural frequency of Mode A and Mode B coincide with Mode 1's natural frequency during the course of the motion. Interestingly, these are also the points in Figure 3.19(a) where the simulated table displacement amplitude exhibits sudden drops. Figure 3.20(a) and (b) show the mode shapes of Mode 1 at $X$ = 160 [mm] and $X$ = 300 [mm]. It is observed that at these locations, the lateral deformation of the ball screw is very pronounced due to the influence of Modes A and B. The interference resulting from the interaction between Modes A and B with Mode 1 is the reason for the observed drops in the table's vibration amplitude and modal displacement in Mode 1.

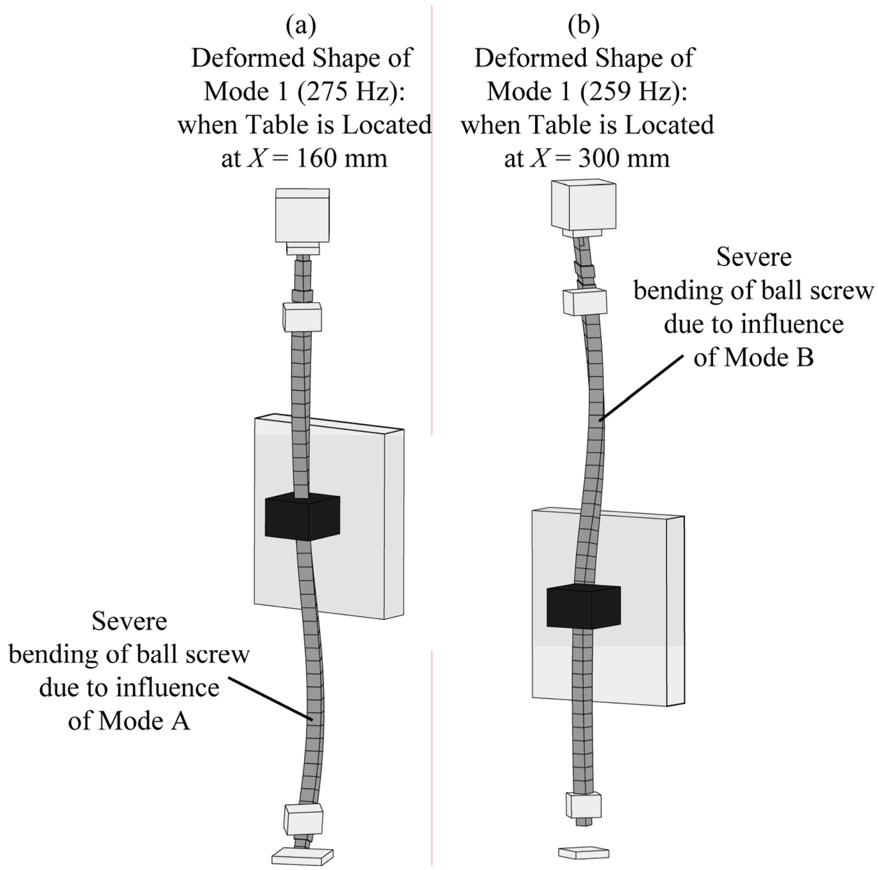


**Figure 3.20: Simulated Deformed Shapes of Mode 1 with Table at (a) X = 160 [mm] and (b) X = 300 [mm] Showing Influence of Mode A and Mode B on Bending of Screw**

**Mode 2: Mode Simulated around 629 Hz (Measured around 613 Hz)**

As shown in Figure 3.15(b), Mode 2 is characterized by the turning of motor (about the torsional coupling joint) and twisting of the ball screw resulting in very little axial displacement of the table. This simulated shape is in good agreement with the observations of other researchers [28][29][54][70]. It also justifies why this mode features prominently in the measured/simulated FRF between a torque applied to the motor and the motor's rotary displacement (i.e. Figure 3.12) but it does not show up in any significant way in the other two FRFs where excitations are applied to and/or displacements measured from the table.

**Mode 3: Mode Simulated around 813 Hz (Measured around 728 Hz)**

The simulated mode shape shown in Figure 3.15(c) reveals that Mode 3 involves the yaw motion of the table (as a result of the guideway joints) together with the bending of the ball screw. No turning of the rotor occurs in this mode, which is why it does not appear in either of the measured/simulated FRFs involving a torque applied at the motor (i.e. Figures 3.12 and 3.13). However, as a result of the yaw motion of the table, Mode 3 is excited when a force is applied to the table and measurements taken from the table as in the case of Figure 3.14. The measured shape of the table (Figure 3.21) also confirms this simulated yaw motion of the table. Mode shapes resulting from the guideway joints have been reported in [14].

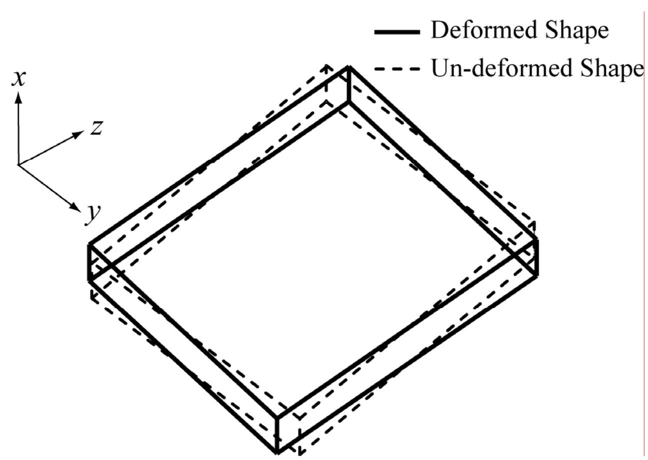


**Figure 3.21: Measured Shape of Table due to Mode 3**

### 3.4.4 Implication of Ball Screw Drive Modes on Controller Design

So far, the modes commonly observed in ball screw drives have been identified and analyzed. For the purpose of this thesis, it is now important to determine if and how these modes influence high speed controller design for ball screw drives.

Starting with Mode 3, it is observed from the mode shape of Figure 3.15(c) and the FRFs of Figure 3.13 that it is not controllable using the actuation torque from the motor because there is no rotation of the motor (rotor) when it is excited. However, since it originates from the guideway joint, it can be dealt with easily by stiffening the guideways. For instance, based on simulations, increasing the guideway stiffness by using a medium preloaded linear guide set instead of a lightly preloaded set, the resonance frequency of the Mode 3 is increased by 33 [%]. In this way, it can be pushed out of the frequency range of interest. It is therefore considered to be the least critical mode with respect to controller design since it can be dealt with by making simple improvements to the mechanical design [54][67].

Mode 2, which is due to the torsional vibration of ball screw shaft, is controllable from the motor, at the expense of exciting it by the control signals. However, it cannot be excited by table disturbance forces and it does not affect the table's position in any significant way. The excitation of this mode by the motor torque command can be prevented by placing a notch filter in the control loop [28][29][54][70]. This is possible because it does not have a wide variation in frequency as the table position changes. Therefore, a notch filter can be tuned to effectively prevent its influence on the feedback control system.

Mode 1 is also controllable from the motor, so it can be excited by control signals. However, it can also be excited by table disturbance forces and it has a wide variation in resonance frequency as a function of table position. These factors make it a poor candidate for notch filters. Increasing the stiffness of the ball screw by increasing its diameter is also not a good choice since it results in a much larger increase in the drive's inertia which is undesirable. Attempts have been made to add damping to this mode passively using a visco-elastic damper attached to the distal end of the ball screw [79]. However, this method is not always effective because of the complex shape of Mode 1 which continually changes depending on the position of the table. Furthermore, incorporating a passive damper into the mechanical design often involves costly and cumbersome modifications to the ball screw drive.

Considering the foregoing discussion, coupled with the fact that Mode 1 is usually the lowest mode in the open-loop dynamics of ball screw drives [28][29][40][54][70][79], it is decidedly the most critical mode in terms of controller design. Consequently, it is selected as the candidate for accurate parameter identification in the next section and active vibration compensation in the next chapter.

### 3.5 Identification of Ball Screw Drive Parameters Needed for Controller Design

While theoretical models are helpful in understanding the qualitative behavior of the open-loop structural dynamics of ball screw drives they are not accurate enough to provide the quantitative information needed for controller design. In this section, a simple ball screw drive model which captures the dynamics of Mode 1 together with the rigid body dynamics of the drive is presented. Then a method for accurately identifying the parameters of the model from experimental data is put forward. Finally, the parameters of the test bed described in Section 3.4.1 are identified and the results discussed.

#### 3.5.1 Drive's Model

A model which captures the dynamics of Mode 1 together with the rigid body dynamics of ball screw drives was proposed by Varanasi and Nayfeh [79]. In their model they represented the ball screw by a uniform beam and the other drive components by rigid bodies connected by springs. They then transformed the infinite-dimensional beam model into a two degree-of-freedom (DOF) discrete system using Galerkin's reduction procedure. The resultant two DOF model is expressed by:

$$\mathbf{M}\ddot{\mathbf{x}} + \mathbf{C}\dot{\mathbf{x}} + \mathbf{K}\mathbf{x} = \mathbf{F} \tag{3.37}$$

where **M**, **C** and **K** are mass, viscous damping and stiffness matrices defined as:

$$\mathbf{M} = \begin{bmatrix} m_{11} & m_{12} \\ m_{12} & m_{22} \end{bmatrix}; \quad \mathbf{C} = \begin{bmatrix} c_{11} & c_{12} \\ c_{12} & c_{22} \end{bmatrix}; \quad \mathbf{K} = \begin{bmatrix} k & -k \\ -k & k \end{bmatrix} \tag{3.38}$$

while **x** and **F** are the displacement and force vectors given by:

$$\mathbf{x} = \begin{Bmatrix} x_1 \\ x_2 \end{Bmatrix}; \quad \mathbf{F} = \begin{Bmatrix} F_1 \\ F_2 \end{Bmatrix} \tag{3.39}$$

As shown in Figure 3.22, $x_1$ is the linear displacement of the table while $x_2$ is the equivalent linear displacement caused by the angular displacement of the motor ($\theta_2$). $F_1$ is the resultant force applied to the table and $F_2$ is the equivalent force due to the resultant torque applied to the motor shaft ($\tau_2$) with the following conversions:

$$x_2 = \theta_2 r_g; \quad F_2 = \frac{\tau_2}{r_g} \tag{3.40}$$

$r_g$ is the constant defined in Eq.(3.13).

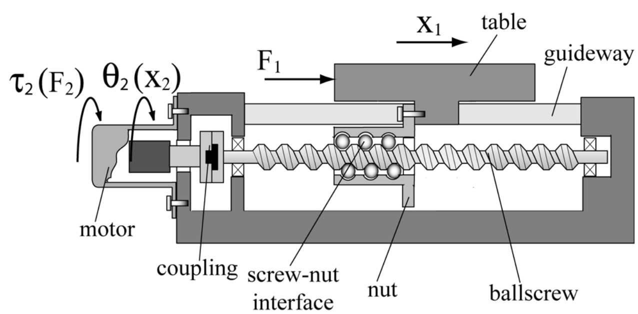


**Figure 3.22: Schematic of a Ball Screw Drive Showing the Displacements and Forces of Eq.(3.39)**

The mass matrix, **M**, has non-zero off-diagonal terms ($m_{12}$) which originate from the distributed inertia of the ball screw. They are very significant because they could introduce a non-minimum phase zero into the open-loop transfer function (OLTF) of the drive (from motor torque to table position) [79]. A non-minimum phase zero in the OLTF of the drive influences the controller dynamics significantly and reduces the attainable closed-loop performance of the drive as is illustrated in the next chapter.

Except the damping and some bearing stiffness constants, Varanasi and Nayfeh [79] obtained the parameters of the matrices of Eq.(3.37) from mathematical models and catalog values of each drive component. As explained in Section 3.4.2, this approach is often not accurate enough for control purposes on an existing machine. Furthermore, their model did not consider the lateral deformation effects of the ball screw. As a result, errors are introduced to the individual elements of the mass, damping and stiffness matrices of

Eq.(3.37). However, the structure of these matrices is not affected by the aforementioned shortcomings. Therefore, Eq.(3.37) serves as a simple ball screw drive model whose parameters are accurately identified using the methods presented in the following subsections.

### 3.5.2 Identification of Model Parameters – General Method

When the three characteristic open-loop (OL) frequency response functions (FRF) described in Section 3.4.2 are measurable from the drive, they can be used to extract the mass, damping and stiffness matrices of Eq.(3.37). To do this, Eq.(3.37) is transformed to frequency domain as:

$$\mathbf{G}(\omega)(-\omega^2\mathbf{M} + j\omega\mathbf{C} + \mathbf{K}) = \mathbf{I} \tag{3.41}$$

where **I** is the identity matrix and $\mathbf{G}(\omega)$ is the transfer function matrix defined as:

$$\mathbf{G}(\omega) = \begin{bmatrix} G_{11}(\omega) & G_{12}(\omega) \\ G_{12}(\omega) & G_{22}(\omega) \end{bmatrix}; G_{11}(\omega) = \left.\frac{x_1(\omega)}{F_1(\omega)}\right|_{F_2(\omega)=0}; G_{22}(\omega) = \left.\frac{x_2(\omega)}{F_2(\omega)}\right|_{F_1(\omega)=0};\ G_{12}(\omega) = \left.\frac{x_1(\omega)}{F_2(\omega)}\right|_{F_1(\omega)=0} = \left.\frac{x_2(\omega)}{F_1(\omega)}\right|_{F_2(\omega)=0} \tag{3.42}$$

In other words, $G_{11}(\omega)$ represents the FRF of Figure 3.14, while $G_{12}(\omega)$ and $G_{22}(\omega)$ represent the FRFs of Figures 3.13 and 3.12 scaled by $r_g$ and $r_g^2$, respectively.

Expanding Eq.(3.41) gives:

$$\begin{aligned}
-m_{11}\omega^2 G_{11}(\omega) - m_{12}\omega^2 G_{12}(\omega) + c_{11} j\omega G_{11}(\omega) + c_{12} j\omega G_{12}(\omega) + k\left(G_{11}(\omega) - G_{12}(\omega)\right) &= 1 \\
-m_{12}\omega^2 G_{11}(\omega) - m_{22}\omega^2 G_{12}(\omega) + c_{12} j\omega G_{11}(\omega) + c_{22} j\omega G_{12}(\omega) + k\left(G_{12}(\omega) - G_{11}(\omega)\right) &= 0 \\
-m_{11}\omega^2 G_{12}(\omega) - m_{12}\omega^2 G_{22}(\omega) + c_{11} j\omega G_{12}(\omega) + c_{12} j\omega G_{22}(\omega) + k\left(G_{12}(\omega) - G_{22}(\omega)\right) &= 0 \\
-m_{12}\omega^2 G_{12}(\omega) - m_{22}\omega^2 G_{22}(\omega) + c_{12} j\omega G_{12}(\omega) + c_{22} j\omega G_{22}(\omega) + k\left(G_{22}(\omega) - G_{12}(\omega)\right) &= 1
\end{aligned} \tag{3.43}$$

In many cases, the low frequency data of measured FRFs is not very accurate because of the influence of non-linear Coulomb friction and the poor characteristics of some sensors in the lower frequency band. This problem tends to affect the quality of the rigid-body dynamics information which dominates the lower frequencies of the measured FRFs. To mitigate this problem, the rigid-body dynamics (i.e. the equivalent mass $M_r$ and viscous damping factor $B_r$) are estimated accurately in time-domain [27][28]. This identified $M_r$ and $B_r$ can then be used as a constraint for Eq.(3.43) by noting that during rigid-body motions, $x_1 = x_2$. Substituting this condition in Eq.(3.37) results in:

$$m_{11} + m_{22} - 2m_{12} = M_r;\ \ c_{11} + c_{22} - 2c_{12} = B_r \tag{3.44}$$

By separating the real and imaginary parts of Eq.(3.43) and then adding on the constraint of Eq.(3.44), the unknown physical parameters of the drive can be evaluated by applying the least squares technique on the measured FRFs using the expression:

$$\mathbf{\Theta} = (\mathbf{\Phi}^{\mathbf{T}}\mathbf{W}\mathbf{\Phi})^{-1}\mathbf{\Phi}^{\mathbf{T}}\mathbf{W}\mathbf{\Gamma} \tag{3.45}$$

where $\mathbf{\Theta}$, $\mathbf{\Gamma}$ and $\mathbf{\Phi}$ are given by:

$$\mathbf{\Theta} = \{m_{11} \quad m_{12} \quad m_{22} \quad c_{11} \quad c_{12} \quad c_{22} \quad k\}^T$$

$$\mathbf{\Gamma} = \{\mathbf{1}_{1\times N} \quad \mathbf{0}_{1\times N} \quad \mathbf{0}_{1\times N} \quad \mathbf{1}_{1\times N} \quad \mathbf{0}_{1\times N} \quad \mathbf{0}_{1\times N} \quad \mathbf{0}_{1\times N} \quad \mathbf{0}_{1\times N} \quad M_r \quad B_r\}^T$$

$$\mathbf{\Phi} = \begin{bmatrix}
-\omega^2 \operatorname{Re} G_{11} & -\omega^2 \operatorname{Re} G_{12} & \mathbf{0}_{1\times N} & -\omega \operatorname{Im} G_{11} & -\omega \operatorname{Im} G_{12} & \mathbf{0}_{1\times N} & \operatorname{Re} G_{11} - \operatorname{Re} G_{12} \\
\mathbf{0}_{1\times N} & -\omega^2 \operatorname{Re} G_{11} & -\omega^2 \operatorname{Re} G_{12} & \mathbf{0}_{1\times N} & -\omega \operatorname{Im} G_{11} & -\omega \operatorname{Im} G_{12} & \operatorname{Re} G_{12} - \operatorname{Re} G_{11} \\
-\omega^2 \operatorname{Re} G_{12} & -\omega^2 \operatorname{Re} G_{22} & \mathbf{0}_{1\times N} & -\omega \operatorname{Im} G_{12} & -\omega \operatorname{Im} G_{22} & \mathbf{0}_{1\times N} & \operatorname{Re} G_{12} - \operatorname{Re} G_{22} \\
\mathbf{0}_{1\times N} & -\omega^2 \operatorname{Re} G_{12} & -\omega^2 \operatorname{Re} G_{22} & \mathbf{0}_{1\times N} & -\omega \operatorname{Im} G_{12} & -\omega \operatorname{Im} G_{22} & \operatorname{Re} G_{22} - \operatorname{Re} G_{12} \\
-\omega^2 \operatorname{Im} G_{11} & -\omega^2 \operatorname{Im} G_{12} & \mathbf{0}_{1\times N} & \omega \operatorname{Re} G_{11} & \omega \operatorname{Re} G_{12} & \mathbf{0}_{1\times N} & \operatorname{Im} G_{11} - \operatorname{Im} G_{12} \\
\mathbf{0}_{1\times N} & -\omega^2 \operatorname{Im} G_{11} & -\omega^2 \operatorname{Im} G_{12} & \mathbf{0}_{1\times N} & \omega \operatorname{Re} G_{11} & \omega \operatorname{Re} G_{12} & \operatorname{Im} G_{12} - \operatorname{Im} G_{11} \\
-\omega^2 \operatorname{Im} G_{12} & -\omega^2 \operatorname{Im} G_{22} & \mathbf{0}_{1\times N} & \omega \operatorname{Re} G_{12} & \omega \operatorname{Re} G_{22} & \mathbf{0}_{1\times N} & \operatorname{Im} G_{12} - \operatorname{Im} G_{22} \\
\mathbf{0}_{1\times N} & -\omega^2 \operatorname{Im} G_{12} & -\omega^2 \operatorname{Im} G_{22} & \mathbf{0}_{1\times N} & \omega \operatorname{Re} G_{12} & \omega \operatorname{Re} G_{22} & \operatorname{Im} G_{22} - \operatorname{Im} G_{12} \\
1 & 2 & 1 & 0 & 0 & 0 & 0 \\
0 & 0 & 0 & 1 & 2 & 1 & 0
\end{bmatrix} \tag{3.46}$$

and $N$ is the number of frequencies spanning the entire spectrum containing the natural modes of interest in the measured FRFs. $\mathbf{W}$ in Eq.(3.45) is a diagonal weighting matrix that is used to place more emphasis on the frequency bands that contain the mode of interest (i.e. Mode 1).

### 3.5.3 Identification of Model Parameters – Simplified Method

The general identification method presented in the previous section is very useful because it extracts the parameters of the drive from the "raw" FRFs measured directly from the drive. However, it suffers from two main problems. First of all, it is quite sensitive to the quality of the measured data. For instance, if the noise level in the measurements is high around the frequencies of interest, the accuracy of the results could be severely affected. Secondly, if the frequency range used for the least squares estimation is large, **Φ** in Eq.(3.45) becomes a very large matrix (i.e. 8*N*+2x7). Consequently, computational problems could arise due to insufficient memory space for storing and manipulating the matrices during the solution.

The first problem can be solved by first using a curve fitting method [4][30] to identify the modal parameters of Mode 1. Then using the identified modal parameters to synthesize the drive's FRFs in a "cleaner" way as:

$$G_{ij}(\omega) = \frac{1}{-\omega^2 M_r + j\omega B_r} + \frac{\alpha_{ij} + j\omega\beta_{ij}}{-\omega^2 + j\omega 2\zeta\omega_n + \omega_n^2}; \quad i = 1; j = 1..2 \tag{3.47}$$

where $\omega_n$ and $\zeta$ are respectively the natural frequency and modal damping ratio of Mode 1, and $R_{ij} = \alpha_{ij} + j\omega\beta_{ij}$ is the complex modal constant of Mode 1 for each of the FRFs. Using the synthesized FRFs instead of the "raw" FRFs eliminates the adverse effects of noise and other distortions on the quality of the least squares estimates.

Usually, in mechanical structures, the modal damping ratio ($\zeta$) is very low (typically less than 3 [%]). This also means that for most cases, the complex modal constant $R_{ij}$ is "almost real". In other words, $\beta_{ij}$ is negligible. Under this circumstance, the system acts as if it is undamped and the mode shapes of the drive are orthogonal to its mass and stiffness matrices [4][30]. This means that if the mode shape matrix **U** is mass-normalized, then the **M** and **K** matrices of Eq.(3.38) can be approximated by:

$$\mathbf{M} = \mathbf{U}^{-T}\mathbf{U}^{-1};\ \mathbf{K} = \mathbf{U}^{-T}\mathbf{K}_q\mathbf{U}^{-1};\ \mathbf{K}_q = \begin{bmatrix} 0 & 0 \\ 0 & \omega_n^2 \end{bmatrix};\ \mathbf{U} = \begin{bmatrix} \sqrt{M_r^{-1}} & \sqrt{R_{11}} \\ \sqrt{M_r^{-1}} & \sqrt{R_{22}} \end{bmatrix} \tag{3.48}$$

If the viscous damping constant $B_r$ is negligible, the damping matrix becomes proportional to the stiffness matrix and so it can also be approximated in a similar way; i.e.:

$$\mathbf{C} = \mathbf{U}^{-T}\mathbf{C}_q\mathbf{U}^{-1};\ \mathbf{C}_q = \begin{bmatrix} 0 & 0 \\ 0 & 2\zeta\omega_n \end{bmatrix} \tag{3.49}$$

However, in most ball screw drives, $B_r$ is not negligible. Therefore, Eq.(3.49) does not hold true. Consequently, to calculate the damping matrix **C**, the information from Eq.(3.48) is incorporated into Eq.(3.46) leading to a computationally cheaper set of matrices:

$$\mathbf{\Theta} = \{c_{11} \quad c_{12} \quad c_{22}\}^T$$

$$\mathbf{\Gamma} = \ldots \quad \mathbf{\Phi} = \ldots$$

$$\begin{Bmatrix}
\mathbf{1}_{1\times N} + m_{11}\omega^2 \operatorname{Re}G_{11} + m_{12}\omega^2 \operatorname{Re}G_{12} - k(\operatorname{Re}G_{11} - \operatorname{Re}G_{12}) \\
\mathbf{0}_{1\times N} + m_{12}\omega^2 \operatorname{Re}G_{11} + m_{22}\omega^2 \operatorname{Re}G_{12} - k(\operatorname{Re}G_{12} - \operatorname{Re}G_{11}) \\
\mathbf{0}_{1\times N} + m_{11}\omega^2 \operatorname{Re}G_{12} + m_{12}\omega^2 \operatorname{Re}G_{22} - k(\operatorname{Re}G_{12} - \operatorname{Re}G_{22}) \\
\mathbf{1}_{1\times N} + m_{12}\omega^2 \operatorname{Re}G_{12} + m_{22}\omega^2 \operatorname{Re}G_{22} - k(\operatorname{Re}G_{22} - \operatorname{Re}G_{12}) \\
\mathbf{0}_{1\times N} + m_{11}\omega^2 \operatorname{Im}G_{11} + m_{12}\omega^2 \operatorname{Im}G_{12} - k(\operatorname{Im}G_{11} - \operatorname{Im}G_{12}) \\
\mathbf{0}_{1\times N} + m_{12}\omega^2 \operatorname{Im}G_{11} + m_{22}\omega^2 \operatorname{Im}G_{12} - k(\operatorname{Im}G_{12} - \operatorname{Im}G_{11}) \\
\mathbf{0}_{1\times N} + m_{11}\omega^2 \operatorname{Im}G_{12} + m_{12}\omega^2 \operatorname{Im}G_{22} - k(\operatorname{Im}G_{12} - \operatorname{Im}G_{22}) \\
\mathbf{0}_{1\times N} + m_{12}\omega^2 \operatorname{Im}G_{12} + m_{22}\omega^2 \operatorname{Im}G_{22} - k(\operatorname{Im}G_{22} - \operatorname{Im}G_{12}) \\
B_r
\end{Bmatrix}
\quad
\begin{bmatrix}
-\omega\operatorname{Im}G_{11} & -\omega\operatorname{Im}G_{12} & \mathbf{0}_{1\times N} \\
\mathbf{0}_{1\times N} & -\omega\operatorname{Im}G_{11} & -\omega\operatorname{Im}G_{12} \\
-\omega\operatorname{Im}G_{12} & -\omega\operatorname{Im}G_{22} & \mathbf{0}_{1\times N} \\
\mathbf{0}_{1\times N} & -\omega\operatorname{Im}G_{12} & -\omega\operatorname{Im}G_{22} \\
\omega\operatorname{Re}G_{11} & \omega\operatorname{Re}G_{12} & \mathbf{0}_{1\times N} \\
\mathbf{0}_{1\times N} & \omega\operatorname{Re}G_{11} & \omega\operatorname{Re}G_{12} \\
\omega\operatorname{Re}G_{12} & \omega\operatorname{Re}G_{22} & \mathbf{0}_{1\times N} \\
\mathbf{0}_{1\times N} & \omega\operatorname{Re}G_{12} & \omega\operatorname{Re}G_{22} \\
1 & 2 & 1
\end{bmatrix} \tag{3.50}$$

which are solved using the same Least Squares equation expressed in (3.45).

Another advantage of the simplified method is that if the mode shapes are assumed to be real, then the following relationships exist among the modal constants in Eq.(3.47) [4][30]:

$$\alpha_{12} = \sqrt{\alpha_{11}\alpha_{22}} \tag{3.51}$$

If the modal parameters are extracted from any two of the three open-loop FRFs (i.e. $G_{11}$, $G_{12}$ and $G_{22}$), the third one can be synthesized by combining Eq.(3.47) and Eq.(3.51). In other words, only two FRFs need to be measured from the drive in order to accurately identify the mass, damping and stiffness matrices of the drive.

### 3.5.4 Numerical Examples

Two numerical examples are presented here to compare the performance of the general method to the simplified approach for under different damping conditions.

**Example 1: Parameter Identification with Weakly-Damped Mode 1**

The mass, damping and stiffness matrices to be identified are given as:

$$\mathbf{M}=\begin{bmatrix}25.00 & -2.00\\ -2.00 & 50.00\end{bmatrix}\text{kg};\ \mathbf{C}=\begin{bmatrix}1400 & -1000\\ -1000 & 1600\end{bmatrix}\text{kg/s};\ \mathbf{K}=3.500\times10^{7}\begin{bmatrix}1 & -1\\ -1 & 1\end{bmatrix}\text{N/m} \tag{3.52}$$

Based on these matrices, the natural frequency and damping ratio of Mode 1 are 225 [Hz] and 2.5 [%], respectively, while its mode shape vector is $[0.9018\ -0.4321+0.0015j]^T$. Using the general method, the mass, damping and stiffness matrices are identified without error. The simplified method however identifies them as:

$$\mathbf{M}=\begin{bmatrix}24.999 & -2.000\\ -2.000 & 50.001\end{bmatrix}\text{kg};\mathbf{C}=\begin{bmatrix}1400 & -1000\\ -1000 & 1600\end{bmatrix}\text{kg/s};\mathbf{K}=3.500\times10^{7}\begin{bmatrix}1 & -1\\ -1 & 1\end{bmatrix}\text{N/m} \tag{3.53}$$

As seen, the identification errors are negligible.

**Example 2: Parameter Identification with Heavily-Damped Mode 1**

The mass and stiffness matrices to be identified are exactly the same as those in Eq.(3.52) while the damping matrix is modified slightly. The new damping matrix is:

$$\mathbf{C}=\begin{bmatrix}11000 & -10000\\ -10000 & 10000\end{bmatrix}\text{kg/s}; \tag{3.54}$$

Based on this new damping matrix, the damping ratio of Mode 1 increases to 20 [%] while its mode shape vector becomes more complex $[0.9028\ -0.4300+0.01302j]^T$. Again, using the general method, the mass, damping and stiffness matrices are identified without error. This time, the matrices identified by the simplified method are:

$$
\mathbf{M} = \begin{bmatrix} 24.935 & -2.036 \\ -2.036 & 50.137 \end{bmatrix} \text{kg}; \mathbf{C} = \begin{bmatrix} 11008 & -10008 \\ -10008 & 10008 \end{bmatrix} \text{kg/s};
$$

$$
\mathbf{K} = 3.499 \times 10^7 \begin{bmatrix} 1 & -1 \\ -1 & 1 \end{bmatrix} \text{N/m} \tag{3.55}
$$

Even though the errors in the identified parameters have increased slightly, the identified matrices are still accurate enough for practical purposes.

These two examples show that the approximations made in the simplified method are very reasonable for practical applications. Therefore, the simplified parameter identification method is used to identify the test bed's parameters in the next subsection.

### 3.5.5 Experimental Results

Application of the simplified identification method requires the rigid-body parameters (i.e. $M_r$ and $B_r$) to be extracted from time-domain data and then the modal properties of Mode 1 are identified from measured FRFs.

To identify $B_r$, the friction characteristics of the drive are obtained by measuring the equivalent motor force required to move the table at constant velocities. This equivalent motor force is equal to the friction force on the drive (in the absence of any other external forces). The resulting curve is shown in Figure 3.23.

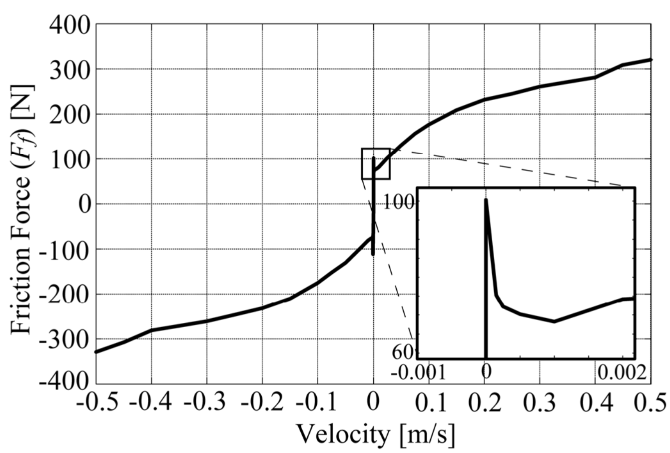


**Figure 3.23: Friction Curve of Ball Screw Test Bed**

The friction curve of Figure 3.23 exhibits some nonlinear behavior, particularly at low velocities. These nonlinearities are associated with the transition from static friction to full viscous friction behavior [28][43]. As a result of this nonlinear behavior, the viscous friction coefficient ($B_r$) is not constant. The customary way of tacking this nonlinear friction behavior is to separate it into linear viscous friction and nonlinear static and Coulomb friction characteristics. The viscous friction is then lumped into a constant value of $B_r$ while the nonlinear friction is compensated for using feed forward friction cancelation schemes [28] [29][43]. For the measured friction curve, however, this separation is not very helpful because even in the high speed region, the friction behavior is not perfectly linear. Therefore, the viscous friction coefficient $B_r$ is set to zero and all of the friction behavior is lumped together as the nonlinear $F_f$ shown in Figure 3.23. Consequently, the equivalent inertia $M_r$ can be identified by noting that during rigid body motions:

$$M_r\ddot{x} = F_2 + F_f \tag{3.56}$$

where $\ddot{x}$ represents the rigid-body acceleration of the drive and $F_2$ is the equivalent force applied by the motor. A least squares technique [27][28] is then used to estimate $M_r$ by applying known values of $F_2$ (Figure 3.24(a)) to the drive and measuring $x$ using the encoder mounted to the motor shaft. The identified friction curve is used to obtain $F_f$ as a function of $\dot{x}$. Figure 3.24(b) compares the measured rigid-body acceleration to the predicted acceleration using the estimate value of $M_r$ = 68.9 [kg]. The results indicate that $M_r$ is estimated accurately.

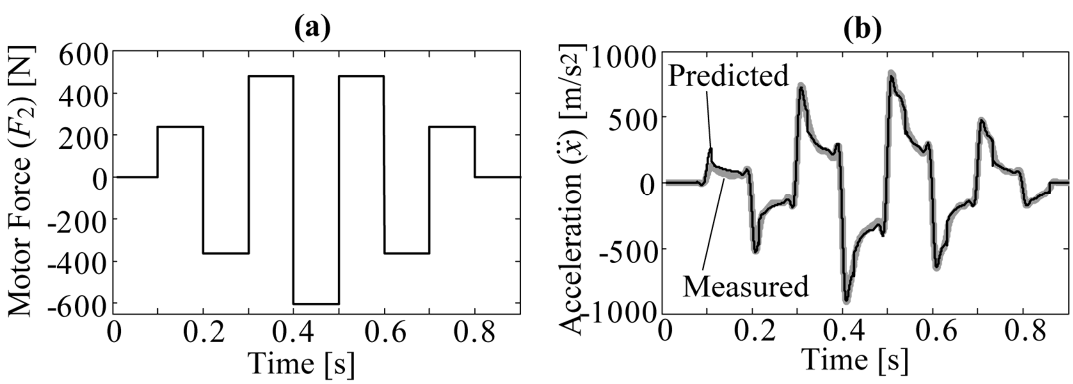


**Figure 3.24: (a) Motor Force Applied to Drive (b) Measured and Predicted Acceleration of Drive based on Identified Mass**

Using the identified rigid body parameters, the simplified parameter identification method (described in Section 3.5.3) is used to extract the drive's mass, damping and stiffness matrices. The identification is carried at 20 [mm] intervals within the travel range of the table (i.e. from $X$ = 30 [mm] to $X$ = 390 [mm]). Figure 3.25 shows the evolution of the identified system matrix coefficients as a function of $X$. It is interesting to note from the plot that the lateral deformation of the table has significant influence on the identified parameters particularly around $X$ = 150 [mm] and $X$ = 300 [mm]. Figure 3.26 shows the measured and predicted FRFs for a sample position of the table ($X$ = 210 [mm]). It can be seen that the predicted and measured FRFs are in very good agreement. The slight discrepancies at the low frequency range are due to the nonlinear damping characteristics that were not included in the model. Furthermore, the slight mismatch in the amplitudes of the predicted and measured FRFs for $G_{11}$ around the resonance frequency is due to the inability of the impact hammer to fully excite the dynamics of the drive. But this inaccuracy in the measured $G_{11}$ does not affect the accuracy of the model because the modal parameters used for the identification are obtained from only $G_{12}$ and $G_{22}$.

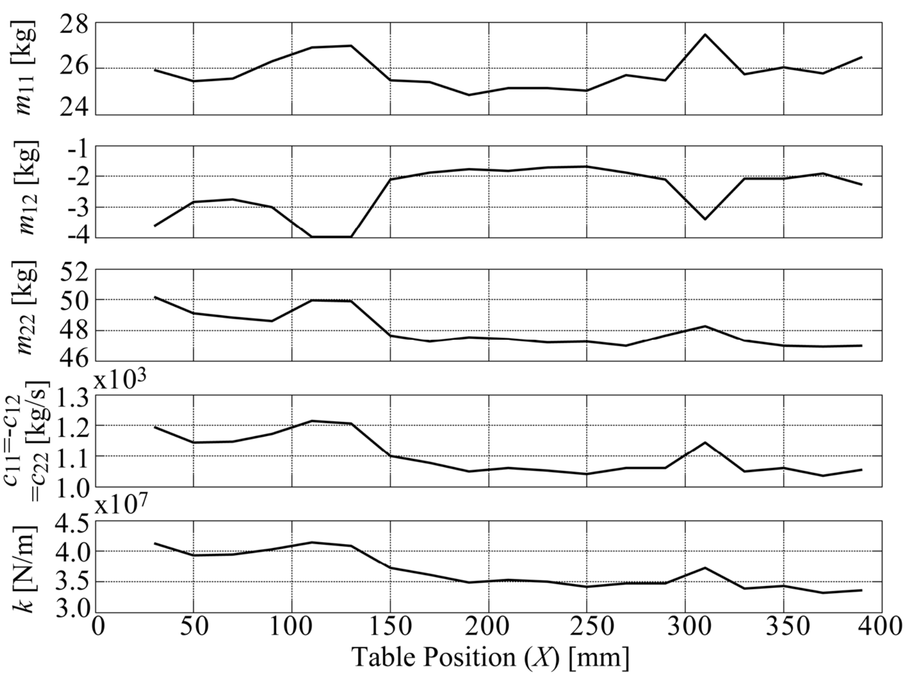


**Figure 3.25: Evolution of Identified System Matrix Coefficients with Table Position**

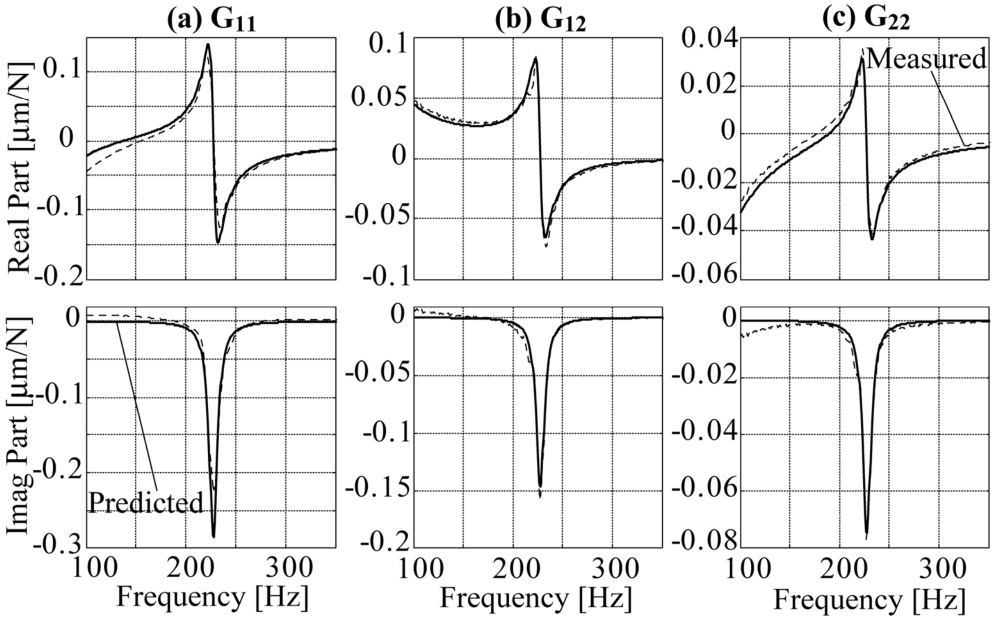


**Figure 3.26: Comparison of Predicted and Measured FRFs based on Identified Parameters for X = 210 [mm]**

### 3.6 Summary

In this chapter, the structural dynamics of ball screw drives has been studied via simulation and experiments in order to better understand how it can potentially influence controller design for ball screw driven machines. The simulations have been carried out by modeling the drive using a hybrid finite element method. A key part of the finite element modeling involves the accurate characterization of the behavior of the screw-nut interface. Two methods for deriving the stiffness matrix of the screw-nut interface have been put forward. One of the methods is more suitable for short nuts while the other is intended for use with longer nuts and more flexible ball screws. Both of these new screw-nut interface stiffness formulations have been shown to possess cross-coupling terms between the axial, torsional and lateral directions that have not been previously reported in literature. As a result of these extra cross-coupling terms, the finite element model is able to give good qualitative insight into the influence of lateral vibrations on the mode shapes of the ball screw drive and the axial positioning of the table.

Furthermore, it has been determined, based on the simulations and experiments conducted, that the first axial-torsional-lateral mode of the ball screw drive potentially wields the most influence on controller design. Therefore, a method for accurately identifying the dynamics of this mode (along with the rigid body dynamics of the drive) has been put forward. The identified dynamics is used in the next chapter to design a controller that achieves good positioning accuracy by actively compensating the vibrations arising from this axial-torsional-lateral mode.

# Chapter 4

# Control of Flexible Ball Screw Drives using a Discrete-Time Sliding Mode Controller

## 4.1 Overview

This chapter presents a controller for achieving minimum tracking error and good disturbance rejection in ball screw drives with structural flexibility. In Section 4.2, the dynamics of ball screw drives, modeled and identified in the previous chapter, is used to design a mode-compensating disturbance adaptive discrete-time sliding mode controller. It is then shown theoretically that, without using minimum tracking error filters, the reference tracking errors of the controlled drive do not go to zero when sliding mode is reached. Therefore, a method for designing stable and robust minimum tracking error filters, irrespective of the identified open-loop behavior of the drive is developed in Section 4.3. The minimum tracking error filters are shown to achieve excellent tracking performance in ideal situations. However, in the presence of varying and/or un-modeled dynamics their performance deteriorates. In Section 4.4, two methods for improving the performance of the minimum tracking error filters in such less-than-ideal situations are presented. Finally, the performance and limitations of the proposed controller are demonstrated, through simulations and experiments, in Section 4.5.

## 4.2 Mode-Compensating Disturbance Adaptive Discrete-time Sliding Mode Controller

Sliding mode controllers are favored in many applications because of their simplicity, high-performance and robustness (e.g. [5][69][75][83]). The disturbance adaptive discrete-time sliding mode controller (DADSC) was proposed by Won and Hedrick [83], in response to drawbacks of other sliding mode controllers [5][69] especially in terms of disturbance estimation and control input saturations. It was designed for controlling single-input-single-output (SISO) systems and was specifically applied in [83] to the speed control of engines.

In order to employ the DADSC for the control of flexible ball screw drives, the original DADSC [83] is reformulated here as a single input-multi output controller designed to achieve structural vibration mode compensation.

### 4.2.1 Sliding Surface Design and Dynamics

The equation of motion of flexible ball screw drives derived in the previous chapter (Eq.(3.37)) is transformed into the following state space form:

$$\begin{Bmatrix} \dot{z}_1 \\ \dot{z}_2 \\ \dot{z}_3 \\ \dot{z}_4 \end{Bmatrix} = \begin{bmatrix} 0 & 0 & 1 & 0 \\ 0 & 0 & 0 & 1 \\ a_{11} & a_{12} & a_{13} & a_{14} \\ a_{21} & a_{22} & a_{23} & a_{24} \end{bmatrix} \begin{Bmatrix} z_1 \\ z_2 \\ z_3 \\ z_4 \end{Bmatrix} + \begin{bmatrix} 0 & 0 \\ 0 & 0 \\ b_{11} & b_{12} \\ b_{21} & b_{22} \end{bmatrix} \begin{Bmatrix} F_1 \\ F_2 \end{Bmatrix} \tag{4.1}$$

where the state vector, **z**, consists of displacements and velocities at the table and motor:

$$\mathbf{z} = \begin{Bmatrix} z_1 & z_2 & z_3 & z_4 \end{Bmatrix}^T = \begin{Bmatrix} x_1 & x_2 & \dot{x}_1 & \dot{x}_2 \end{Bmatrix}^T \tag{4.2}$$

The state matrix parameters are given as:

$$\begin{bmatrix} a_{11} & a_{12} \\ a_{21} & a_{22} \end{bmatrix} = \mathbf{-M^{-1}K}; \begin{bmatrix} a_{13} & a_{14} \\ a_{23} & a_{24} \end{bmatrix} = \mathbf{-M^{-1}C}; \begin{bmatrix} b_{11} & b_{12} \\ b_{21} & b_{22} \end{bmatrix} = \mathbf{M^{-1}} \tag{4.3}$$

The tracking error vector can then be written as:

$$\mathbf{e} = \mathbf{z_r} - \mathbf{z} \tag{4.4}$$

where the error (**e**) and reference ($\mathbf{z_r}$) vectors are given by:

$$\mathbf{e} = \begin{Bmatrix} e_1 & e_2 & e_3 & e_4 \end{Bmatrix}^T ; \mathbf{z_r} = \begin{Bmatrix} z_{1r} & z_{2r} & z_{3r} & z_{4r} \end{Bmatrix}^T \tag{4.5}$$

In Eq.(4.5), $z_{1r}$ and $z_{2r}$ represent the desired displacements while $z_{3r}$ and $z_{4r}$ are the corresponding desired velocities at the table and motor, respectively. Based on these definitions, the error states become:

$$
\begin{aligned}
\dot{e}_1 &= e_3 \\
\dot{e}_2 &= e_4 \\
\dot{e}_3 &= \dot{z}_{3r} - \left(a_{11}z_1 + a_{12}z_2 + a_{13}z_3 + a_{14}z_4 + b_{11}F_1 + b_{12}F_2\right) \\
\dot{e}_4 &= \dot{z}_{4r} - \left(a_{21}z_1 + a_{22}z_2 + a_{23}z_3 + a_{24}z_4 + b_{21}F_1 + b_{22}F_2\right)
\end{aligned}
\tag{4.6}
$$

The discrete-time equivalent of the drive model is derived by employing the backward Euler approximation given as:

$$
\dot{p} = \frac{z-1}{Tz}p \tag{4.7}
$$

where $p$ is a dummy variable and $T$ is the sampling period. Discretizing Eq.(4.6) with Eq.(4.7), the discrete state errors are obtained as:

$$
\begin{aligned}
e_1(k) &= e_1(k-1) + Te_3(k) \\
e_2(k) &= e_2(k-1) + Te_4(k) \\
e_3(k) &= e_3(k-1) + T\left(\dot{z}_{3r}(k) - \left(a_{11}z_1(k) + a_{12}z_2(k) + a_{13}z_3(k) + a_{14}z_4(k) + b_{11}F_1(k) + b_{12}F_2(k)\right)\right) \\
e_4(k) &= e_4(k-1) + T\left(\dot{z}_{4r}(k) - \left(a_{21}z_1(k) + a_{22}z_2(k) + a_{23}z_3(k) + a_{24}z_4(k) + b_{21}F_1(k) + b_{22}F_2(k)\right)\right)
\end{aligned}
\tag{4.8}
$$

The sliding surface is designed to minimize the four state errors at each discrete control interval ($k$) as:

$$
s(k) = \lambda_1 e_1(k) + \lambda_2 e_2(k) + \lambda_3 e_3(k) + \lambda_4 e_4(k) \tag{4.9}
$$

where $\lambda_1 ... \lambda_4$ are gains which together determine the dynamics of the sliding surface after sliding mode is reached. By substituting the state errors (Eq.(4.8)) into Eq.(4.9), the sliding surface (before any specific control force is defined) is expressed as:

$$
\begin{aligned}
&s(k) = s(k-1) + T\{\lambda_1 e_3(k) + \lambda_2 e_4(k)\ldots \\
&+\lambda_3\left(\dot{z}_{3r}(k) - \left(a_{11}z_1(k) + a_{12}z_2(k) + a_{13}z_3(k) + a_{14}z_4(k) + b_{11}F_1(k) + b_{12}F_2(k)\right)\right)\ldots \\
&+\lambda_4\left(\dot{z}_{4r}(k) - \left(a_{21}z_1(k) + a_{22}z_2(k) + a_{23}z_3(k) + a_{24}z_4(k) + b_{21}F_1(k) + b_{22}F_2(k)\right)\right)\}
\end{aligned}
\tag{4.10}
$$

which is governed by the dynamics of the drive (i.e. **M**, **C** and **K** in Eq.(4.3)), the disturbance force ($F_1$), motor command ($F_2$), states, state errors and the reference acceleration signals.

The control law can be used to manipulate the equivalent current or torque on the drive ($F_2$). According to [83], $F_2$ is designed to cancel all the terms in Eq.(4.10) except $s(k-1)$, while introducing a feedback term with gain $K$ into the sliding surface. The resulting $F_2$ is expressed as:

$$\begin{aligned} F_2(k) = \big[ & \lambda_3 \dot{z}_{3r}(k) + \lambda_4 \dot{z}_{4r}(k) - \left(\lambda_3 a_{11} + \lambda_4 a_{21}\right) z_1(k) - \left(\lambda_3 a_{12} + \lambda_4 a_{22}\right) z_2(k) \\ & - \left(\lambda_3 a_{13} + \lambda_4 a_{23}\right) z_3(k) - \left(\lambda_3 a_{14} + \lambda_4 a_{24}\right) z_4(k) - \left(\lambda_3 b_{11} + \lambda_4 b_{21}\right) \hat{F}_1(k) \\ & + \lambda_1 e_3(k) + \lambda_2 e_4(k) + Ks(k) \big] \cdot \frac{1}{\lambda_3 b_{12} + \lambda_4 b_{22}} \end{aligned} \tag{4.11}$$

In Eq.(4.11), $\hat{F}_1$ is the estimated table disturbance force calculated by the adaptation law given in [83]:

$$\hat{F}_1(k) = \hat{F}_1(k-1) - g_1 s(k) + g_2 s(k-1) \tag{4.12}$$

where $g_1$ and $g_2$ are adaptation gains. If the disturbance adaptation error ($\tilde{F}_1$) is defined as $\tilde{F}_1(k) = \hat{F}_1(k) - F_1(k)$, Eq.(4.12) can be re-written as:

$$\tilde{F}_1(k) = \hat{F}_1(k) - F_1(k) = \tilde{F}_1(k-1) - g_1 s(k) + g_2 s(k-1) - F_1(k) + F_1(k-1) \tag{4.13}$$

Substituting $F_2(k)$, as defined in Eq.(4.11), into Eq.(4.10), and combining the resulting equation with Eq.(4.13), the dynamics of the disturbance adaptation and sliding surface emerges as:

$$\begin{Bmatrix} s(k) \\ \tilde{F}_1(k) \end{Bmatrix} = \frac{1}{Q + Rg_1} \begin{bmatrix} 1 + Rg_2 & R \\ g_2 Q - g_1 & Q \end{bmatrix} \begin{Bmatrix} s(k-1) \\ \tilde{F}_1(k-1) \end{Bmatrix} + \frac{1}{Q + Rg_1} \begin{Bmatrix} R \\ Q \end{Bmatrix} \left( F_1(k-1) - F_1(k) \right) \tag{4.14}$$

where:

$$Q = 1 + KT; \quad R = T\left(\lambda_3 b_{11} + \lambda_4 b_{21}\right) \tag{4.15}$$

As explained in [83], the disturbance estimation error ($\tilde{F}_1$) can be decoupled from the sliding surface dynamics in Eq.(4.14) by selecting $g_2 = Q^{-1} g_1$, thus making the coefficient, $g_2 Q - g_1$ equal to zero. The decoupled dynamics results in better disturbance adaptation in the DADSC compared to the adaptive sliding mode controller [5][69] (as will be demonstrated in the next chapter).

If the disturbance ($F_1$) is constant and bounded, the sliding surface is forced to achieve sliding mode (i.e. $s(k) = 0$) by selecting $K$ and $g_1$ such that the eigenvalues of the sliding surface dynamics (in Eq.(4.14)) lie within the unit circle. The two eigenvalues of the sliding surface are evaluated from Eq.(4.14) as:

$$\lambda_{S1} = (1+KT)^{-1},\ \lambda_{S2} = (1+KT+Rg_1)^{-1}(1+KT) \tag{4.16}$$

These two eigenvalues are forced to lie within unit circle by selecting gain $K > 0$ and $\mathrm{sgn}(R)\cdot g_1 > 0$ as:

$$\begin{aligned} |\lambda_{S1}| &= \left|(1+KT)^{-1}\right| < 1 \ \Rightarrow\ KT > 0 \ \text{ or } K > 0,\ \text{since } T > 0 \\ |\lambda_{S2}| &= \left|(1+KT+Rg_1)^{-1}(1+KT)\right| < 1 \ \Rightarrow \mathrm{sgn}(R)\cdot g_1 > 0 \end{aligned} \tag{4.17}$$

which ensures asymptotic stability of the sliding surface and disturbance adaptation dynamics.

### 4.2.2 Error Dynamics

The ability of the proposed mode-compensating DADSC (MCDADSC) to push the reference tracking errors to zero, when sliding mode is reached, is investigated in this section by analyzing the error dynamics of the closed-loop system.

The error dynamics can be derived by substituting the control law in Eq.(4.11) into the open-loop dynamics of Eq.(4.8) then simplifying the result using the sliding surface and disturbance force estimate defined in Eq.(4.9) and Eq.(4.13), respectively. The result is:

$$
\underbrace{\begin{bmatrix} 1 & 0 & -T & 0 & 0 \\ 0 & 1 & 0 & -T & 0 \\ -TN_{11} & -TN_{12} & 1-TN_{13} & -TN_{14} & -Tb_{11} \\ -TN_{21} & -TN_{22} & -TN_{23} & 1-TN_{24} & -Tb_{12} \\ \lambda_1 g_1 & \lambda_2 g_1 & \lambda_3 g_1 & \lambda_4 g_1 & 1 \end{bmatrix}}_{\mathbf{A}_L} \begin{Bmatrix} e_1(k) \\ e_2(k) \\ e_3(k) \\ e_4(k) \\ \tilde{F}_1(k) \end{Bmatrix} =
$$

$$
\underbrace{\begin{bmatrix} 1 & 0 & 0 & 0 & 0 \\ 0 & 1 & 0 & 0 & 0 \\ 0 & 0 & 1 & 0 & 0 \\ 0 & 0 & 0 & 1 & 0 \\ \lambda_1 g_2 & \lambda_2 g_2 & \lambda_3 g_2 & \lambda_4 g_2 & 1 \end{bmatrix}}_{\mathbf{A}_R} \begin{Bmatrix} e_1(k-1) \\ e_2(k-1) \\ e_3(k-1) \\ e_4(k-1) \\ \tilde{F}_1(k-1) \end{Bmatrix} + \underbrace{\begin{Bmatrix} 0 \\ 0 \\ \Sigma_1(k) \\ \Sigma_2(k) \\ F_1(k-1)-F_1(k) \end{Bmatrix}}_{\mathbf{B}_R} \tag{4.18}
$$

where $N_{ij}$ are defined as:

$$
\begin{aligned}
&N_{11} = L_{11} - \lambda_1 K\gamma;\;\; N_{12} = L_{12} - \lambda_2 K\gamma;\;\; N_{13} = L_{13} - \lambda_3 K\gamma - \lambda_1\gamma;\;\; N_{14} = L_{14} - \lambda_4 K\gamma - \lambda_2\gamma; \\
&N_{21} = L_{21} - \lambda_1 K\Gamma;\;\; N_{22} = L_{22} - \lambda_2 K\Gamma;\;\; N_{23} = L_{23} - \lambda_3 K\Gamma - \lambda_1\Gamma;\;\; N_{24} = L_{24} - \lambda_4 K\Gamma - \lambda_2\Gamma; \\
&L_{1j} = (1-\lambda_3\gamma)a_{1j} - \lambda_4\gamma a_{2j};\;\; L_{2j} = -\lambda_3\Gamma a_{1j} + (1-\lambda_4\Gamma)a_{2j};\; j = 1\cdots 4 \\
&\gamma = b_{12}(\lambda_3 b_{12} + \lambda_4 b_{22})^{-1};\;\; \Gamma = b_{22}(\lambda_3 b_{12} + \lambda_4 b_{22})^{-1}
\end{aligned} \tag{4.19}
$$

$\Sigma_1(k)$ and $\Sigma_2(k)$ are functions of the time-step ($k$) given by:

$$
\begin{aligned}
&\Sigma_1(k) = (1-\lambda_3\gamma)\dot{z}_{3r}(k) - \lambda_4\gamma\dot{z}_{4r}(k) - L_{11}z_{1r}(k) - L_{12}z_{2r}(k) - L_{13}z_{3r}(k) - L_{14}z_{4r}(k) - L_{15}\hat{F}_1(k) \\
&\Sigma_2(k) = -\lambda_3\Gamma\dot{z}_{3r}(k) + (1-\lambda_3\Gamma)\dot{z}_{4r}(k) - L_{21}z_{1r}(k) - L_{22}z_{2r}(k) - L_{23}z_{3r}(k) - L_{24}z_{4r}(k) - L_{25}\hat{F}_1(k) \\
&L_{15} = (1-\lambda_3\gamma)b_{11} - \lambda_4\gamma b_{21};\;\; L_{25} = -\lambda_3\Gamma b_{11} + (1-\lambda_4\Gamma)b_{21}
\end{aligned} \tag{4.20}
$$

From Eq.(4.18), if the controller parameters ($\lambda_1 \ldots \lambda_4$, $g_1$, $g_2$ and $K$) are chosen such that the eigenvalues of the matrix $\mathbf{A}_L^{-1}\mathbf{A}_R$ are all within the unit circle the stability of the controlled system is guaranteed. Furthermore, all the errors asymptotically go to zero as time tends to infinity, providing that the disturbance force is constant and that the discrete-time forcing functions $\Sigma_1(k)$ and $\Sigma_2(k)$ are zero, or become zero with time. However, as long as $\Sigma_1(k)$ and

$\Sigma_2(k)$ remain as non-zero forcing functions, the tracking errors do not become zero even if the sliding mode is reached.

### 4.3 Minimum-Tracking Error Filter (MTEF)

In [40], Kamalzadeh and Erkorkmaz point out that since the accurate positioning of the table is most important in ball screw drives, the position reference command to the motor ($z_{2r}$) can be chosen arbitrarily. They propose a method of generating $z_{2r}$ which focuses on offsetting the axial deformations that occur during the acceleration/deceleration of the drive and when external forces are applied to the table, providing the value of $b_{12}$ is zero.

The problem, however, is that $b_{12}$ is not normally zero in ball screw drives because of the presence of the non-zero off-diagonal terms ($m_{12}$) in the mass matrix of the drive dynamics given in Eq.(3.37). These non-zero $m_{12}$ terms are by products of the distributed inertia of the ball screw [79]. As mentioned in Section 3.5.1, the presence of non-zero $m_{12}$ (or $b_{12}$) often has the effect of introducing non-minimum phase zeros into the dynamics of ball screw-driven machines [79]. Under such circumstances, the method proposed in [40], which is based on inverting the ball screw drive's dynamics, becomes unstable and thus destabilizes the whole controller.

Here, a filter is designed to generate $z_{2r}$ in such a way that, irrespective of the value of $b_{12}$ (i.e. $m_{12}$), the filter remains stable and minimizes the forcing functions $\Sigma_1(k)$ and $\Sigma_2(k)$, thereby minimizing the state tracking errors of the MCDADSC.

#### 4.3.1 Design and Stability of MTEF

Consider the following two equations:

$$\dot{z}_{3r}(k) = a_{11}z_{1r}(k) + a_{12}z_{2r}(k) + a_{13}z_{3r}(k) + a_{14}z_{4r}(k) + b_{11}\hat{F}_1(k) + b_{12}F_2(k) \tag{4.21}$$

$$\dot{z}_{4r}(k) = a_{21}z_{1r}(k) + a_{22}z_{2r}(k) + a_{23}z_{3r}(k) + a_{24}z_{4r}(k) + b_{21}\hat{F}_1(k) + b_{22}F_2(k) \tag{4.22}$$

and the linear combination of Eq.(4.21) and Eq.(4.22):

$$\lambda_3\dot{z}_{3r}(k)+\lambda_4\dot{z}_{4r}(k)=(\lambda_3 a_{11}+\lambda_4 a_{21})z_{1r}(k)+(\lambda_3 a_{12}+\lambda_4 a_{22})z_{2r}(k)+(\lambda_3 a_{13}+\lambda_4 a_{23})z_{3r}(k)$$
$$+(\lambda_3 a_{14}+\lambda_4 a_{24})z_{4r}(k)+(\lambda_3 b_{11}+\lambda_4 b_{21})\hat{F}_1(k)+(\lambda_3 b_{12}+\lambda_3 b_{22})F_2(k)$$

(4.23)

$\Sigma_1(k)$ is obtained by eliminating $F_2$ from Eq.(4.21) and Eq.(4.23), while $\Sigma_2(k)$ emerges from the elimination of $F_2$ from Eq.(4.22) and Eq.(4.23). Consequently, $\Sigma_1(k)$ and $\Sigma_2(k)$ are linearly dependent; hence they are also linearly dependent on an equation obtained by eliminating $F_2$ from Eq.(4.21) and Eq.(4.22). The elimination is achieved by multiplying Eq.(4.21) by a factor 1, and Eq.(4.22) by a factor of $r$ and summing up the resulting equations; i.e.:

$$\dot{z}_{3r}(k)+r\dot{z}_{4r}(k)=(a_{11}+ra_{21})z_{1r}(k)+(a_{12}+ra_{22})z_{2r}(k)+(a_{13}+ra_{23})z_{3r}(k)$$
$$+(a_{14}+ra_{24})z_{4r}(k)+(b_{11}+rb_{21})\hat{F}_1(k)+(b_{12}+rb_{22})F_2(k) \qquad (4.24)$$

By choosing the ratio $r = r_e = -b_{12}/b_{22}$, $F_2$ can be eliminated from the equation. For now, $r$ is kept as a variable. Applying the relationship between $z_{2r}$ and its derivatives (Eq.(4.7)) to Eq.(4.24), the reference signal, $z_{2r}$, is calculated as:

$$z_{2r}(z)=G_{mtef}(z)\Psi(z)$$
$$G_{mtef}(z)=\frac{T^2z^2}{\bar{G}z^2+\bar{H}z+\bar{J}}$$
$$\Psi(z)=(a_{11}+ra_{21})z_{1r}(z)+(a_{13}+ra_{23})z_{3r}(z)-\dot{z}_{3r}(z)+(b_{11}+rb_{21})\hat{F}_1(z)+(b_{12}+rb_{22})F_2(z)$$
$$\bar{G}=r-(a_{12}+ra_{22})T^2-(a_{14}+ra_{24})T;\quad \bar{H}=(a_{14}+ra_{24})T-2r;\quad \bar{J}=r$$

(4.25)

where $z$ is the discrete-time forward-shift operator.

From Eq.(4.25), for the feed-forward filter $G_{mtef}(z)$ to be stable, its two poles:

$$p_{1,2}=-\frac{\bar{H}}{2\bar{G}}\pm\sqrt{\left(\frac{\bar{H}}{2\bar{G}}\right)^2-\frac{\bar{J}}{\bar{G}}} \qquad (4.26)$$

have to lie within the unit circle. If this condition is satisfied for $r = r_e = -b_{12}/b_{22}$ then $G_{mtef}(z)$ is stable and $z_{2r}$ can be generated in a way that makes both $\Sigma_1(k)$ and $\Sigma_2(k)$ equal to zero for all $k$. However, because of the aforementioned non-zero off-diagonal terms ($m_{12}$) in the drive's mass matrix, a non-minimum phase zero could be introduced into the open-loop dynamics of the drive. Under this condition, one of the poles of $G_{mtef}(z)$ becomes unstable when $r$ is selected as $-b_{12}/b_{22}$. Consequently, $z_{2r}$ becomes unbounded and $\Sigma_1(k)$ and $\Sigma_2(k)$ cannot be made equal to zero for all $k$. In this case, since $r = r_e = -b_{12}/b_{22}$ leads to an unstable filter, $r \neq -b_{12}/b_{22}$ has to be selected such that $G_{mtef}(z)$ is stable and $\Sigma_1(k)$ and $\Sigma_2(k)$ are minimized. The problem, however, is that when $r \neq -b_{12}/b_{22}$ is selected, $F_2$ is not cancelled out of Eq.(4.25) giving rise to large errors in the generation of $z_{2r}$. To solve this problem, an approximate $F_2$ (i.e. $\hat{F}_2$ ) is calculated from Eq.(4.24) by replacing the ratio $r$ with a special ratio $r^*$ and then assuming that the motor and table are connected by a perfectly rigid transmission such that $z_{2r}$ and its derivatives are equal to $z_{1r}$ and its derivatives, respectively. This results in:

$$\hat{F}_2(k) = \frac{1}{(b_{12} + r^* b_{22})}\begin{pmatrix} (1+r^*)\dot{z}_{3r}(k) - (a_{11} + r^* a_{21} + a_{12} + r^* a_{22})z_{1r}(k) \\ -(a_{13} + r^* a_{23} + a_{14} + r^* a_{24})z_{3r}(k) - (b_{11} + r^* b_{21})\hat{F}_1(k) \end{pmatrix} \tag{4.27}$$

The error arising from this approximation can be evaluated by calculating the difference, $\tilde{z}_{2r}$, between the approximate $z_{2r}$ (i.e. $\hat{z}_{2r}$ ) and the exact $z_{2r}$. $\hat{z}_{2r}$ is calculated by substituting Eq.(4.27) into Eq.(4.25), while the exact $z_{2r}$ is calculated by substituting Eq.(4.27) (without any rigid body approximation) into Eq.(4.25). The result is:

$$\begin{aligned} \tilde{z}_{2r}(z) &= z_{2r}(z) - \hat{z}_{2r}(z) = G_{ez}(z)z_{1r}(z) - G_{eF}(z)\hat{F}_1(z) \\ G_{ez}(z) &= \left( \frac{\bar{G}_1 z^2 + \bar{H}_1 z + \bar{J}_1}{\bar{G}_2 z^2 + \bar{H}_2 z + \bar{J}_2} - \frac{\bar{G}_3 z^2 + \bar{H}_3 z + \bar{J}_3}{\bar{G}_4 z^2 + \bar{H}_4 z + \bar{J}_4} \right) \\ G_{eF}(z) &= \left( \frac{\bar{L}T^2 z^2}{\bar{G}_2 z^2 + \bar{H}_2 z + \bar{J}_2} - \frac{\bar{L}T^2 z^2}{\bar{G}_4 z^2 + \bar{H}_4 z + \bar{J}_4} \right) \end{aligned} \tag{4.28}$$

The full expressions of the numerator and denominator coefficients of $G_{ez}(z)$ and $G_{eF}(z)$ as functions of $r$ and $r^*$ are given in Appendix A.

If the special ratio ($r^*$) is chosen such that:

$$r^* = -\frac{a_{11}}{a_{21}} = -\frac{a_{12}}{a_{22}} \tag{4.29}$$

then the dc gains of $G_{ez}(z)$ and $G_{eF}(z)$ vanish (i.e. $G_{ez}(1) = G_{eF}(1) = 0$). As a result, the approximation error ($\tilde{z}_{2r}$) is minimized at low frequencies. It is noteworthy that the value of $r^*$ expressed in Eq.(4.29) holds true only because of the relationship among the $a_{ij}$ parameters as defined in Eq.(4.3).

To minimize $\tilde{z}_{2r}$ at other frequencies ($\omega$) within the desired bandwidth of the controller, the parameter $r$ is selected such that $G_{mtef}(z)$ is stable, i.e.

$$\max(|p_1(r)|, |p_2(r)|) \leq 1 \tag{4.30}$$

and it minimizes the cost function:

$$\max\left(W_1 \max_{\omega} |G_{ez}(\omega, r)|, W_2 \max_{\omega} |G_{eF}(\omega, r)|\right) \tag{4.31}$$

where $W_1$ and $W_2$ are relative weighting factors which are determined based on the expected maximum amplitudes of the reference signal $z_{1r}$ and the disturbance force $F_1$. They could also be defined as functions of frequency $\omega$ (i.e. $W_1(\omega)$ and $W_2(\omega)$). By minimizing $\tilde{z}_{2r}$ in this way, the forcing functions, $\Sigma_1(k)$ and $\Sigma_2(k)$, hence the state tracking errors are minimized using $G_{mtef}(z)$.

### 4.3.2 Robustness of MTEF

Sliding mode controllers are known to be robust due to their inherent adaptation to unknown/un-modeled dynamics [5][69][75]. However, when the MTEF is added on, its effect on the robustness of the MCDADSC has to be investigated.

Robustness of the MTEF is particularly important in ball screw drives where the dynamics (hence the parameters of the model) change from position to position as the table moves along the ball screw. It is also important because, no matter how accurately the drive's dynamics is modeled, there always will be some amount of uncertainty in the model.

To investigate the robustness of the MTEF, let us consider a case where there is uncertainty in each of the parameters in Eq.(4.8) such that each parameter $a_{ij}$ and $b_{ij}$ is perturbed by a small amount $\Delta a_{ij}$ and $\Delta b_{ij}$, respectively, yielding:

$$
\begin{aligned}
e_1(k) &= e_1(k-1) + Te_3(k) \\
e_2(k) &= e_2(k-1) + Te_4(k) \\
e_3(k) &= e_3(k-1) + T\left( \dot{z}_{3r}(k) - \begin{pmatrix} a_{11}z_1(k) + a_{12}z_2(k) + a_{13}z_3(k) + a_{14}z_4(k)\ldots \\ +b_{11}F_1(k) + (b_{12} + \Delta b_{12})F_2(k) + \Delta_1 \end{pmatrix} \right) \\
e_4(k) &= e_4(k-1) + T\left( \dot{z}_{4r}(k) - \begin{pmatrix} a_{21}z_1(k) + a_{22}z_2(k) + a_{23}z_3(k) + a_{24}z_4(k)\ldots \\ +b_{21}F_1(k) + (b_{22} + \Delta b_{22})F_2(k) + \Delta_2 \end{pmatrix} \right)
\end{aligned}
\tag{4.32}
$$

where $\Delta_1$ and $\Delta_2$ are defined as:

$$
\begin{aligned}
\Delta_1 &= \Delta a_{11}z_1(k) + \Delta a_{12}z_2(k) + \Delta a_{13}z_3(k) + \Delta a_{14}z_4(k) + \Delta b_{11}F_1(k) \\
\Delta_2 &= \Delta a_{21}z_1(k) + \Delta a_{22}z_2(k) + \Delta a_{23}z_3(k) + \Delta a_{24}z_4(k) + \Delta b_{21}F_1(k)
\end{aligned}
\tag{4.33}
$$

Following the procedure outlined in Section 4.2.1, the new sliding surface dynamics becomes:

$$
\begin{Bmatrix} s(k) \\ \tilde{F}_1'(k) \end{Bmatrix} = \frac{1}{Q' + R'g_1} \begin{bmatrix} 1 + R'g_2 & R' \\ g_2Q' - g_1 & Q' \end{bmatrix} \begin{Bmatrix} s(k-1) \\ \tilde{F}_1'(k-1) \end{Bmatrix} + \frac{1}{Q' + R'g_1} \begin{Bmatrix} R' \\ Q' \end{Bmatrix} \left( F_1'(k-1) - F_1'(k) \right)
\tag{4.34}
$$

where $F_1'$ is the augmented disturbance force which includes the effect of uncertainties perceived as disturbance forces. It is defined as:

$$
\begin{aligned}
F_1'(k) &= F_\Delta(k) + \theta^{-1}F_1(k) \\
F_\Delta(k) &= \frac{(\theta - 1)}{\theta(\lambda_3 b_{11} + \lambda_4 b_{12})} \begin{pmatrix} \lambda_1 e_3(k) + \lambda_2 e_4(k) + \lambda_3 \dot{z}_{3r}(k) + \lambda_4 \dot{z}_{4r}(k) - \left(\lambda_3 a_{11} + \lambda_4 a_{21}\right) z_1(k) \\ -\left(\lambda_3 a_{12} + \lambda_4 a_{22}\right) z_2(k) - \left(\lambda_3 a_{13} + \lambda_4 a_{23}\right) z_3(k) \\ -\left(\lambda_3 a_{14} + \lambda_4 a_{24}\right) z_4(k) + (\theta - 1)^{-1}(\lambda_3 \Delta_1(k) + \lambda_4 \Delta_2(k)) \end{pmatrix} \\
\theta &= \left(\lambda_3 b_{12} + \lambda_4 b_{22}\right)^{-1} \left(\lambda_3(b_{12} + \Delta b_{12}) + \lambda_4(b_{22} + \Delta b_{22})\right)
\end{aligned}
\tag{4.35}
$$

$\tilde{F}_1' = \hat{F}_1 - F_1'$ while $Q'$ and $R'$ are the modified gains expressed as:

$$
Q' = 1 + \theta KT; \quad R' = \theta T\left(\lambda_3 b_{11} + \lambda_4 b_{21}\right)
\tag{4.36}
$$

As a result of the uncertainties, the error dynamics of Eq.(4.18) becomes:

$$\underbrace{\begin{bmatrix} 1 & 0 & -T & 0 & 0 \\ 0 & 1 & 0 & -T & 0 \\ -TN'_{11} & -TN'_{12} & 1-TN'_{13} & -TN'_{14} & -T\theta b_{11} \\ -TN'_{21} & -TN'_{22} & -TN'_{23} & 1-TN'_{24} & -T\theta b_{12} \\ \lambda_1 g_1 & \lambda_2 g_1 & \lambda_3 g_1 & \lambda_4 g_1 & 1 \end{bmatrix}}_{\mathbf{A}'_L} \begin{Bmatrix} e_1(k) \\ e_2(k) \\ e_3(k) \\ e_4(k) \\ \tilde{F}'_1(k) \end{Bmatrix} =$$

$$\underbrace{\begin{bmatrix} 1 & 0 & 0 & 0 & 0 \\ 0 & 1 & 0 & 0 & 0 \\ 0 & 0 & 1 & 0 & 0 \\ 0 & 0 & 0 & 1 & 0 \\ \lambda_1 g_2 & \lambda_2 g_2 & \lambda_3 g_2 & \lambda_4 g_2 & 1 \end{bmatrix}}_{\mathbf{A}'_R} \begin{Bmatrix} e_1(k-1) \\ e_2(k-1) \\ e_3(k-1) \\ e_4(k-1) \\ \tilde{F}'_1(k-1) \end{Bmatrix} + \underbrace{\begin{Bmatrix} 0 \\ 0 \\ \Sigma_{\Delta 1}(k) \\ \Sigma_{\Delta 2}(k) \\ F'_1(k-1) - F'_1(k) \end{Bmatrix}}_{\mathbf{B}'_R} \tag{4.37}$$

where $N'_{ij}$ are defined as:

$$\begin{aligned} &N'_{11} = L'_{11} - \lambda_1 K\gamma'; \;\; N'_{12} = L'_{12} - \lambda_2 K\gamma'; \;\; N'_{13} = L'_{13} - \lambda_3 K\gamma' - \lambda_1\gamma'; \;\; N'_{14} = L'_{14} - \lambda_4 K\gamma' - \lambda_2\gamma'; \\ &N'_{21} = L'_{21} - \lambda_1 K\Gamma'; \;\; N'_{22} = L'_{22} - \lambda_2 K\Gamma'; \;\; N'_{23} = L'_{23} - \lambda_3 K\Gamma' - \lambda_1\Gamma'; \;\; N'_{24} = L'_{24} - \lambda_4 K\Gamma' - \lambda_2\Gamma'; \\ &L'_{1j} = (1-\lambda_3\gamma')a_{1j} - \lambda_4\gamma' a_{2j} + \Delta a_{1j}; \;\; L'_{2j} = -\lambda_3\Gamma' a_{1j} + (1-\lambda_4\Gamma')a_{2j} + \Delta a_{2j}; \; j = 1\cdots 4 \\ &\gamma' = (b_{12} + \Delta b_{12})(\lambda_3 b_{12} + \lambda_4 b_{22})^{-1}; \;\; \Gamma' = (b_{22} + \Delta b_{22})(\lambda_3 b_{12} + \lambda_4 b_{22})^{-1} \end{aligned} \tag{4.38}$$

The new forcing functions, $\Sigma_{\Delta 1}(k)$ and $\Sigma_{\Delta 2}(k)$ are given by:

$$\begin{aligned} \Sigma_{\Delta 1}(k) &= \Sigma_1(k) + b_{11}\left((1-\theta)\hat{F}_1(k) + \theta F_\Delta(k)\right) - \Delta\dot{z}_{3r}(k) \\ \Sigma_{\Delta 2}(k) &= \Sigma_2(k) + b_{12}\left((1-\theta)\hat{F}_1(k) + \theta F_\Delta(k)\right) - \Delta\dot{z}_{4r}(k) \end{aligned} \tag{4.39}$$

where $\Delta\dot{z}_{3r}$ and $\Delta\dot{z}_{3r}$ are defined as:

$$\begin{aligned} \Delta\dot{z}_{3r}(k) &= \Delta a_{11} z_1(k) + \Delta a_{12} z_2(k) + \Delta a_{13} z_3(k) + \Delta a_{14} z_4(k) + \Delta b_{11} F_1(k) + \Delta b_{12} F_2(k) \\ \Delta\dot{z}_{4r}(k) &= \Delta a_{21} z_1(k) + \Delta a_{22} z_2(k) + \Delta a_{23} z_3(k) + \Delta a_{24} z_4(k) + \Delta b_{21} F_1(k) + \Delta b_{22} F_2(k) \end{aligned} \tag{4.40}$$

Because of the additional terms, the new forcing functions, $\Sigma_{\Delta 1}(k)$ and $\Sigma_{\Delta 2}(k)$, are no longer linearly dependent. Therefore, it is not possible to use the MTEF to simultaneously make both of them zero for all $k$. This problem can be mitigated by noting that, if the disturbance force, $F_1$ is zero, then $\hat{F}_1 \rightarrow F_\Delta$ around their dc value. Consequently, Eq.(4.39) can be re-written as:

$$\begin{aligned} \Sigma_{\Delta 1}(k) &\cong \Sigma_1(k) + b_{11}\alpha \hat{F}_1(k) - \Delta \dot{z}_{3r}(k) \\ \Sigma_{\Delta 2}(k) &\cong \Sigma_2(k) + b_{12}\alpha \hat{F}_1(k) - \Delta \dot{z}_{4r}(k) \end{aligned} \tag{4.41}$$

where $\alpha$ is a scaling factor for $\hat{F}_1$ which can be adjusted to change the dynamics of the forcing functions. Considering that at constant velocity the dc-value of $\Delta \dot{z}_{3r}$ and $\Delta \dot{z}_{3r}$ are equal to zero, the dc-value of the tracking error at the table, $e_1$, can be made equal to zero by selecting $\alpha$ such that:

$$G^{dc}_{e1\Sigma 1}\,\Sigma^{dc}_{\Delta 1}(\alpha) + G^{dc}_{e1\Sigma 2}\,\Sigma^{dc}_{\Delta 2}(\alpha) = 0 \tag{4.42}$$

In Eq.(4.42), $G_{e1\Sigma 1}(z)$ and $G_{e1\Sigma 2}(z)$ are respectively the transfer functions from the table tracking error ($e_1$) to the forcing functions $\Sigma_{\Delta 1}$ and $\Sigma_{\Delta 2}$ which can be obtained from Eq.(4.37) if the model uncertainties are known. The superscript "*dc*" denotes the dc value of the transfer function or signal. The $\alpha$ value that satisfies the condition in Eq.(4.42) depends on which of the two equations in Eq.(4.41) is used to generate $z_{2r}$. In most cases, $\alpha$ cannot be obtained from Eq.(4.42) analytically because the parametric uncertainties of the transfer function are not known a priori. However, it can easily be determined through trial and error by adjusting $\alpha$ iteratively until the table's tracking error is eliminated.

The foregoing analysis has shown that the performance of the MTEF is adversely affected by the presence of un-modeled dynamics. It has also shown that the estimated disturbance force ($\hat{F}_1$) can be scaled and applied to the MTEF to reduce the deterioration of the tracking accuracy of the table (at low frequencies).

However, employing $\hat{F}_1$ to improve the tracking performance of the MTEF gives rise to some other problems. Firstly, the approximation of Eq.(4.41) assumes that $F_1$=0. When $F_1 \neq 0$, scaling $\hat{F}_1$ by $\alpha$ in order improve the tracking performance of the drive gives rise to incomplete cancellation of $F_1$ in the controller. This greatly diminishes of the disturbance rejection property of the controller. Furthermore, special care must be taken when introducing $\hat{F}_1$ into the MTEF even when $F_1 \neq 0$. This is because, as a result of the un-modeled dynamics, the MTEF can no longer completely cancel $\hat{F}_1$ from $\Sigma_{\Delta 1}(k)$ and $\Sigma_{\Delta 2}(k)$. As shown in Figure 4.1, this introduces an additional feedback loop in the MCDADSC which could adversely affect its stability. Consequently, in the following section, two more practical methods for improving the performance and robustness of the MCDADSC and MTEF are described.

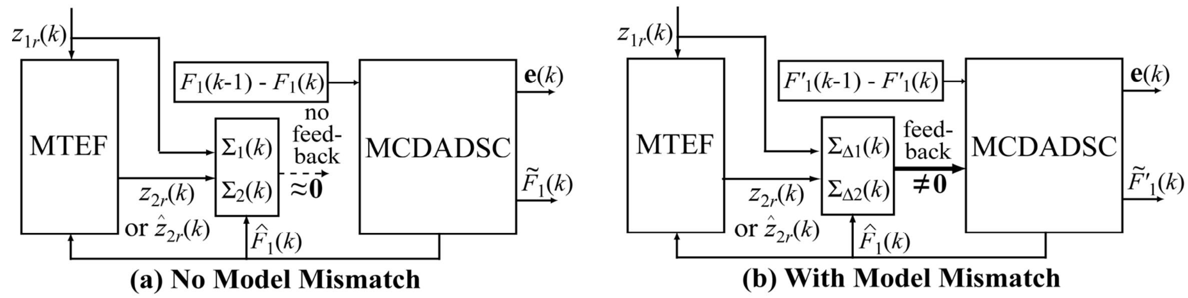


**Figure 4.1: Relationship between MTEF and MCDADSC (a) With no Model Mismatch (b) With Model Mismatch**

### 4.4 Improvement of Performance and Robustness of MCDADSC and MTEF

In this section gain scheduling together with modified disturbance estimation are proffered as means of improving the performance and robustness of the MCDADSC and MTEF in the presence of parametric and non-parametric model uncertainty. Gain scheduling uses the predictable behavior of the plant to reduce the parametric uncertainty while the modified disturbance estimation helps to improve the rejection of other un-modeled low-frequency dynamics.

#### 4.4.1 Gain Scheduling

As explained in Chapter 3, the mass, damping and stiffness matrices of ball screw drives vary in a predictable way as a function of the position of the table along the screw, $X$. This information can be used to schedule the parameters of the MCDADSC and MTEF.

Generally, gain scheduling involves varying parameters of a controller (or varying controllers) to provide satisfactory control for various operating points of a plant which evolves in some predictable fashion as a function of an observable variable called the scheduling variable. In our case, the scheduling variable is $X$.

There are a couple of ways of scheduling controller gains. In [72], Symens et al. compared a simple ad-hoc method with more complicated analytical methods for scheduling the gains of a $H_\infty$ controller designed to control the vibrations of a beam. In their case, the scheduling variable was the length of the beam which influenced the stiffness of the beam in a predictable way. They found out that the analytical methods based on linear parameter varying (LPV) models of the plant performed very poorly compared to the simple ad-hoc one. The reason for this is that the analytical schemes are very conservative because they are based on extremely restrictive assumptions [72].

Consequently, in this chapter, the simple ad-hoc method is employed. The $a_{ij}$ and $b_{ij}$ parameters of the MCDADSC and MTEF are scheduled as function of $X$ while the controller gains, $\lambda_1 \ldots \lambda_4$, $g_1$, $g_2$ and $K$ are kept constant. The functions $a_{ij}(X)$ and $b_{ij}(X)$ are obtained from Eq.(4.3) as:

$$\begin{bmatrix} a_{11}(X) & a_{12}(X) \\ a_{21}(X) & a_{22}(X) \end{bmatrix} = -\mathbf{M}(X)^{-1}\mathbf{K}(X);$$
$$\begin{bmatrix} a_{13}(X) & a_{14}(X) \\ a_{23}(X) & a_{24}(X) \end{bmatrix} = -\mathbf{M}(X)^{-1}\mathbf{C}(X); \; \begin{bmatrix} b_{11}(X) & b_{12}(X) \\ b_{21}(X) & b_{22}(X) \end{bmatrix} = \mathbf{M}(X)^{-1} \tag{4.43}$$

where $\mathbf{M}(X)$, $\mathbf{C}(X)$ and $\mathbf{K}(X)$ are respectively the mass, damping and stiffness matrices of the drive expressed as functions of $X$. Ad-hoc gain scheduling is achieved by updating $a_{ij}$ and $b_{ij}$ in the MCDADSC control law (Eq.(4.11)) and in the MTEF (i.e. Eq.(4.25), (4.27) and (4.29)) based on the instantaneous value of $X$ measured from the drive. The functions $a_{ij}(X)$ and $b_{ij}(X)$ are piecewise continuous, thereby ensuring that the gain scheduling is smooth and that unwanted transients are avoided.

### 4.4.2 Modified Disturbance Estimation

Generally, in sliding mode controllers, disturbance estimation is achieved by integrating the same sliding surface contained in the control law (e.g. Eq.(4.11) and (4.12)). However, Kamalzadeh and Erkorkmaz in [40] observe experimentally that integrating a simpler $1^{st}$ order sliding surface for disturbance estimation instead of the $3^{rd}$ order sliding surface contained in their control law resulted in better performance.

In this subsection, the just-described modified disturbance estimation method of Kamalzadeh and Erkormaz is implemented on the MCDADSC, and a theoretical explanation for improvements observed by using the modified technique is given.

Firstly, the 1st order primary sliding surface, $s_P(k)$, is defined as:

$$s_P(k) = \lambda' e_1(k) + e_3(k) \tag{4.44}$$

where $\lambda'$ is the sliding surface gain. Next, the sliding surface of Eq.(4.9) is made the secondary sliding surface $s_S(k)$:

$$s_S(k) = \lambda_1 e_1(k) + \lambda_2 e_2(k) + \lambda_3 e_3(k) + \lambda_4 e_4(k) \tag{4.45}$$

The primary sliding surface is then used for disturbance estimation according to the law:

$$\hat{F}_1(k) = \hat{F}_1(k-1) - g_1 s_P(k) + g_2 s_P(k-1) \tag{4.46}$$

while the secondary sliding surface is employed in the control law as:

$$\begin{aligned} F_2(k) = \big[ & \lambda_3 \dot{z}_{3r}(k) + \lambda_4 \dot{z}_{4r}(k) - (\lambda_3 a_{11} + \lambda_4 a_{21}) z_1(k) - (\lambda_3 a_{12} + \lambda_4 a_{22}) z_2(k) \\ & - (\lambda_3 a_{13} + \lambda_4 a_{23}) z_3(k) - (\lambda_3 a_{14} + \lambda_4 a_{24}) z_4(k) - (\lambda_3 b_{11} + \lambda_4 b_{21}) \hat{F}_1(k) \\ & + \lambda_1 e_3(k) + \lambda_2 e_4(k) + K s_S(k) \big] \cdot \frac{1}{\lambda_3 b_{12} + \lambda_4 b_{22}} \end{aligned} \tag{4.47}$$

Based on Eqs. (4.32), (4.44) and (4.46), the primary sliding surface and disturbance estimation dynamics can be written as:

$$\begin{Bmatrix} s_P(k) \\ \tilde{F}_1'(k) \end{Bmatrix} = \frac{1}{Q' + R' g_1} \begin{bmatrix} S' + R' g_2 & R' \\ g_2 Q' - S' g_1 & Q' \end{bmatrix} \begin{Bmatrix} s_P(k-1) \\ \tilde{F}_1'(k-1) \end{Bmatrix} + \begin{Bmatrix} * \\ * \end{Bmatrix} \left( F_1'(k-1) - F_1'(k) \right) \tag{4.48}$$

In Eq.(4.48), $F_1'$ is the augmented disturbance force which contains all dynamics that prevent the primary sliding surface from reaching sliding mode. $Q'$, $R'$ and $S'$ are unknown gains which depend on the ball screw drive's parameters, controller parameters and the unknown model errors. $\tilde{F}_1'$ represents the error between $\hat{F}_1$ and $F_1'$ while the asterisks indicate that the elements of the input vector do not matter. If the adaptation gains, $g_1$ and $g_2$, are chosen such that the system matrix in Eq.(4.48) is stable, then the sliding surface dynamics converges to zero over time, providing $F_1'$ is constant and bounded. This means that, in spite of the uncertainties, it is guaranteed that the table will be eventually reach the desired position $z_{1r}$ if $\lambda' > 0$. It is worth noting that it is no longer possible to select $g_2$ such that it decouples the sliding surface dynamics from the disturbance dynamics because $Q'$ and $S'$ are unknown. Therefore, $g_1$ and $g_2$ are tuned by trial and error to ensure stable sliding surface dynamics. Furthermore, there is no longer any guarantee that the secondary sliding surface $s_S(k)$ will converge to zero. As will be explained later using Figure 4.2, it will converge to zero only if there are no disturbance forces and model uncertainties.

Since the modified disturbance estimation law forces the table to reach its desired position, it is no longer necessary to use the inaccurate $\hat{F}_1$ to enforce the low-frequency tracking performance of the MTEF as done in Section 4.3.2. Therefore, the unwanted feedback loop can be eliminated from the MTEF and MCDADSC by setting $\hat{F}_1 = 0$ in Eqs. (4.25), (4.27) and (4.28).

The following example demonstrates using a simple case how the modified MCDADSC compares with the original one.

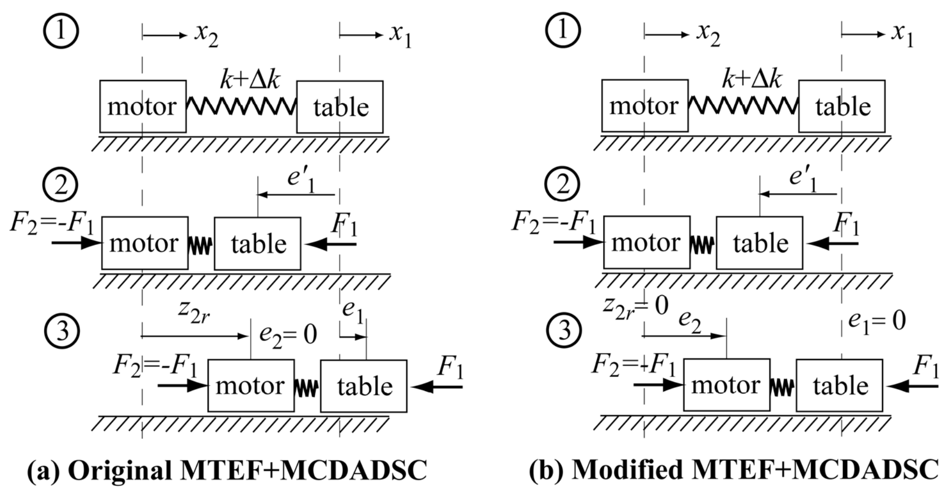


**Figure 4.2: Simple Example Demonstrating Difference between Original MTEF/MCDADSC and Modified MTEF/MCDADSC**

A simplified model of the ball screw drive consisting of two masses representing the motor and the table connected by a spring is shown in Figure 4.2. The spring is assumed to have an actual stiffness of $k+\Delta k$ but its identified (modeled) stiffness is assumed to be $k$. In the figure, $x_1$ and $x_2$ respectively denote the position of the table and motor measured from the dashed datum lines. The aim of this example is to compare the quasi-static response of the original MTEF/MCDADSC (Figure 4.2(a)) to the modified one (Figure 4.2(b)) when a disturbance force $F_1$ is applied to the table.

Initially, in Step 1, both systems are at rest with $x_1$=$x_2$=0. Then in Step 2 $F_1$ is applied to the motor causing the MCDADSC to apply an equal and opposite force $F_2$ to the motor. As a result, the spring is compressed and an error, $e'_1 = F_1/(k+\Delta k)$, occurs in positioning the table whose desired position $z_{1r} = 0$. The positioning error ($e'_1$) is the same for both systems. In Step 3, however, the situation is different for the original and modified MTEF/MCDADSC. In Figure 4.2(a), the original MTEF realizes this error and calculates the reference position of the motor needed to make $x_1$ equal to zero as $z_{2r} = \hat{F}_1/k$. $\hat{F}_1 = -F_2 = F_1$. Typically, the MCDADSC is tuned such that it accurately tracks $z_{2r}$, therefore a positioning error $e_1 = F_1/k - F_1/(k+\Delta k)$ results at the table. This error disappears only when $\hat{F}_1 = F_1$ (as it is in this case) and the model uncertainty $\Delta k$=0. On the other hand, in Figure 4.2(b), the modified MTEF which does not include $\hat{F}_1$ calculates $z_{2r} = 0$. However, as a result of the modified disturbance estimation which ensures that $z_{1r}$ is tracked precisely, the table tracking error is $e_1$=0. This results in an error $e_2 = F_1/(k+\Delta k)$ in tracking $z_{2r}$. In other words, the secondary sliding surface cannot reach sliding mode. This error $e_2$ can only be removed if $F_1 = 0$ or if $\hat{F}_1$=$F_1$ is included into the MTEF and $\Delta k$=0.

The simplified example above provides some insight into how the modified MTEF/MCDADSC achieves good disturbance rejection and tracking accuracy at the low-frequency range.

## 4.5 Simulation and Experimental Tests

### 4.5.1 Simulation Tests

Simulation tests are conducted in this section to evaluate the performance of the control scheme presented in the preceding sections under ideal conditions. In other words, in this section it is assumed that the behavior of the ball screw drive is perfectly governed by Eq.(4.8). Other factors such as non-linear friction, amplifier dynamics, higher-frequency modes and digital-to-analog conversion delays are not considered. This helps us to validate the theoretical analyses presented in the foregoing sections which were performed based on the same idealizations.

Two sets of mass, damping and stiffness matrices are used for the simulation tests. The first set (Eq.(4.49)) represent the matrices identified from the test bed (see Section 3.4.1) at the position $X = 30$ [mm]. Both of its open-loop (OL) zeros are minimum phase. The second set (Eq.(4.50)) represent the matrices measured at $X = 390$ [mm]. However, because none of the identified matrices of the test bed exhibit any non-minimum phase characteristics, the $m_{12}$ value of this second set of matrices is scaled by -0.1 to artificially create a non-minimum phase zero. Thus, Eq.(4.49) represents minimum phase OL dynamics while Eq.(4.50) represents non-minimum phase OL dynamics.

$$\mathbf{M}^{(1)} = \begin{bmatrix} 25.93 & -3.61 \\ -3.61 & 50.19 \end{bmatrix} \text{[kg]}; \mathbf{C}^{(1)} = 1194 \begin{bmatrix} 1 & -1 \\ -1 & 1 \end{bmatrix} \text{[Ns/m]}; \mathbf{K}^{(1)} = 4.127\text{x}10^{7} \begin{bmatrix} 1 & -1 \\ -1 & 1 \end{bmatrix} \text{[N/m]} \tag{4.49}$$

$$\mathbf{M}^{(2)} = \begin{bmatrix} 26.47 & 0.23 \\ 0.23 & 46.98 \end{bmatrix} \text{[kg]}; \mathbf{C}^{(2)} = 1055 \begin{bmatrix} 1 & -1 \\ -1 & 1 \end{bmatrix} \text{[Ns/m]}; \mathbf{K}^{(2)} = 3.3511\text{x}10^{7} \begin{bmatrix} 1 & -1 \\ -1 & 1 \end{bmatrix} \text{[N/m]} \tag{4.50}$$

Using these two sets of matrices three scenarios are investigated using simulation tests in order to show the effectiveness of MCDADSC combined with MTEF compared to MCDADSC without MTEF. The three scenarios are considered for the original MCDADSC/MTEF as well as for the modified one. For the MCDADSC without MTEF, the reference commands for the motor and table assumed to be equal (i.e. $z_{2r} = z_{1r}$). The three scenarios are as follows:

**Scenario 1**: The controller is designed using the first set of matrices (Eq.(4.49)). The parameters of the controller and drive are assumed to be exactly the same (i.e. no parameter mismatch). Since the two OL zeros are minimum phase, $r = r_e = -b_{12}/b_{22}$ is used to design a stable MTEF resulting in perfect cancelation of the forcing functions $\Sigma_1$ and $\Sigma_2$.

**Scenario 2:** The controller is designed using second set of matrices (Eq.(4.50)). The parameters of the controller and drive are assumed to be exactly the same (i.e. no parameter mismatch). Since one of the OL zeros is non-minimum phase, $r \neq -b_{12}/b_{22}$ and $r^* = -a_{12}/a_{22}$

are used to design a stable MTEF resulting in an approximate cancelation of the forcing functions $\Sigma_1$ and $\Sigma_2$.

**Scenario 3**: The controller is designed using the first set of matrices (Eq.(4.49)). However, the parameters of the drive are taken as those of the second set of matrices (Eq.(4.50)). Therefore there is parameter mismatch. $r = r_e = -b_{12}/b_{22}$ is used to design a stable MTEF. However, because of the parameter mismatch, $\alpha$ is introduced to the original MTEF to cancel out the dc-errors due to the parameter mismatch.

The controller parameters of the original and modified MCDADSC/MTEFs are summarized in Table 4.1 and Table 4.2, respectively.

| **Parameter** | **Value** |
|---|---|
| $\lambda_1$ | 0 [1/s] |
| $\lambda_2$ | 5000 [1/s] |
| $\lambda_3$ | 0.1 |
| $\lambda_4$ | 1 |
| $K$ | 1x10$^7$ [1/s] |
| $g_1$ | 1x10$^5$ [kg/s] |
| $T$ | 50 [μs] |
| $r$ (*for Scenarios 1 and 3*) | $-b_{12}/b_{22}$ |
| $r$ (*for Scenario 2*) | 0 |
| $r^*$ (*Only for Scenario 2*) | $-a_{12}/a_{22}$ |
| $\alpha$ (*Only for Scenario 3*) | -2.7 |

**Table 4.1: Parameters used in Simulation Tests of Original MCDADSC and MTEF**

| **Parameter** | **Value** |
|---|---|
| $\lambda_1$ | 0 [1/s] |
| $\lambda_2$ | 1200 [1/s] |
| $\lambda_3$ | 0.1 |
| $\lambda_4$ | 1 |
| $\lambda'$ | 2000 [1/s] |
| $K$ | 500 [1/s] |
| $g_1$ | 10,000 [kg/s] |
| $T$ | 50 [μs] |
| $r$ (*for Scenarios 1 and 3*) | $-b_{12}/b_{22}$ |
| $r$ (*for Scenario 2*) | 0 |
| $r^*$ (*Only for Scenario 2*) | $-a_{12}/a_{22}$ |
| $\alpha$ | N/A |

**Table 4.2: Parameters used in Simulation Tests of Modified MCDADSC and MTEF**

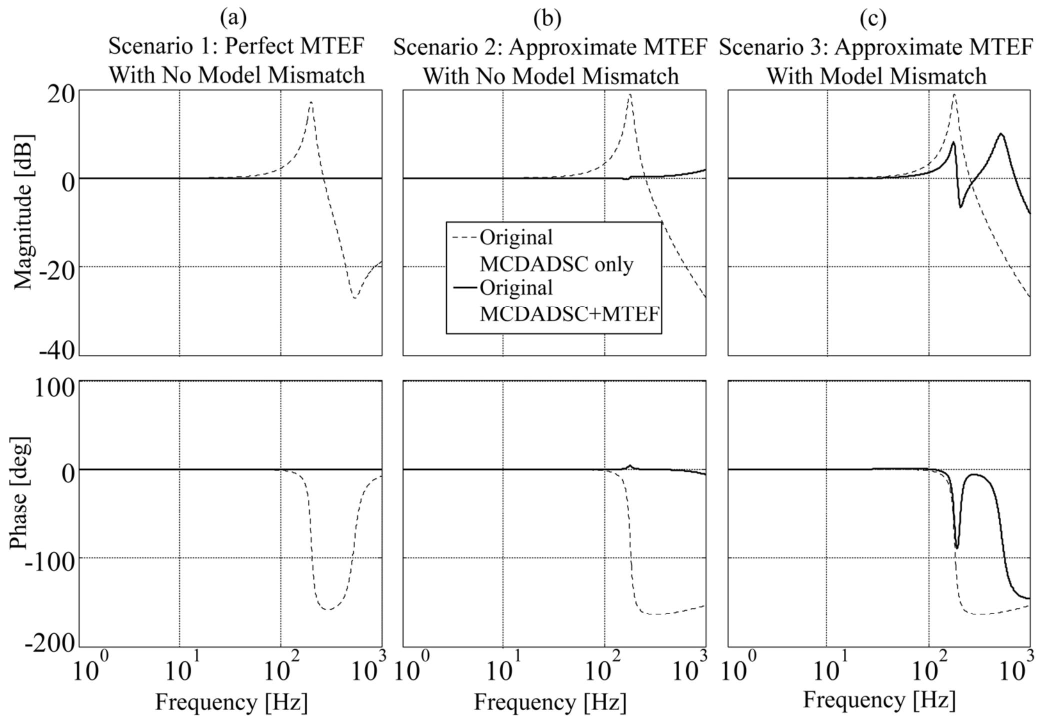


**Figure 4.3: Comparison of Simulated Table Tracking FRF ($z_1/z_{1r}$) of Original MCDADSC Only and Original MCDADSC+MTEF for Three Different Scenarios**

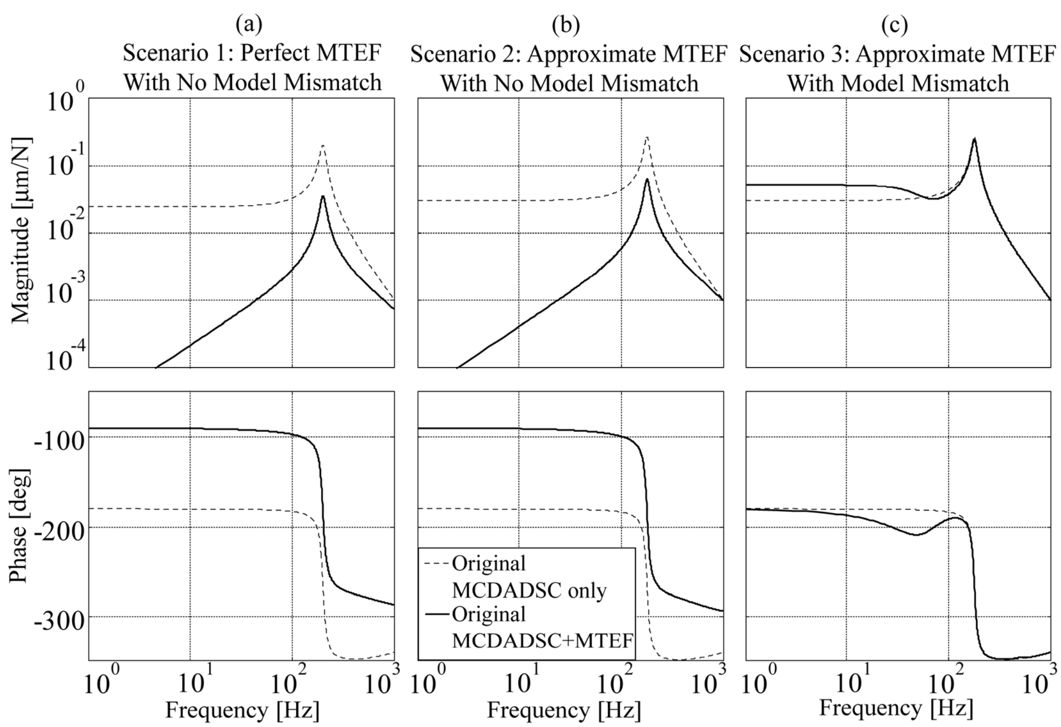


**Figure 4.4: Comparison of Simulated Table Disturbance FRF ($z_1/F_1$) of Original MCDADSC Only and Original MCDADSC+MTEF for Three Different Scenarios**

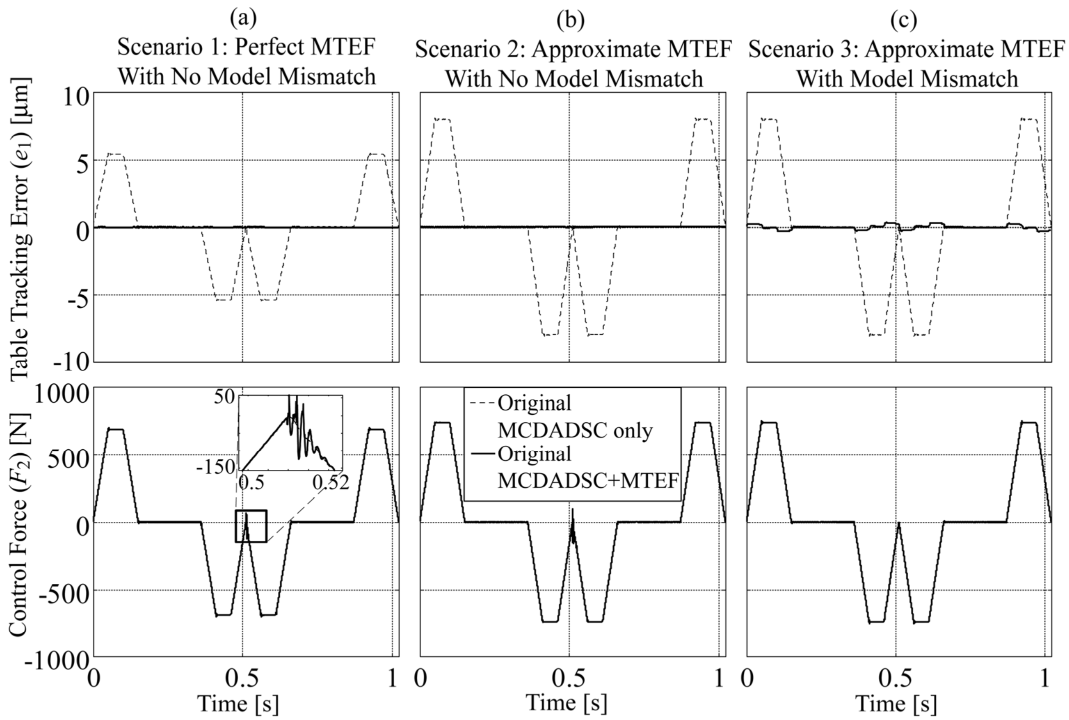


**Figure 4.5: Comparison of Simulated High Speed Trajectory Tracking Response of Original MCDADSC Only and Original MCDADSC+MTEF for Three Different Scenarios**

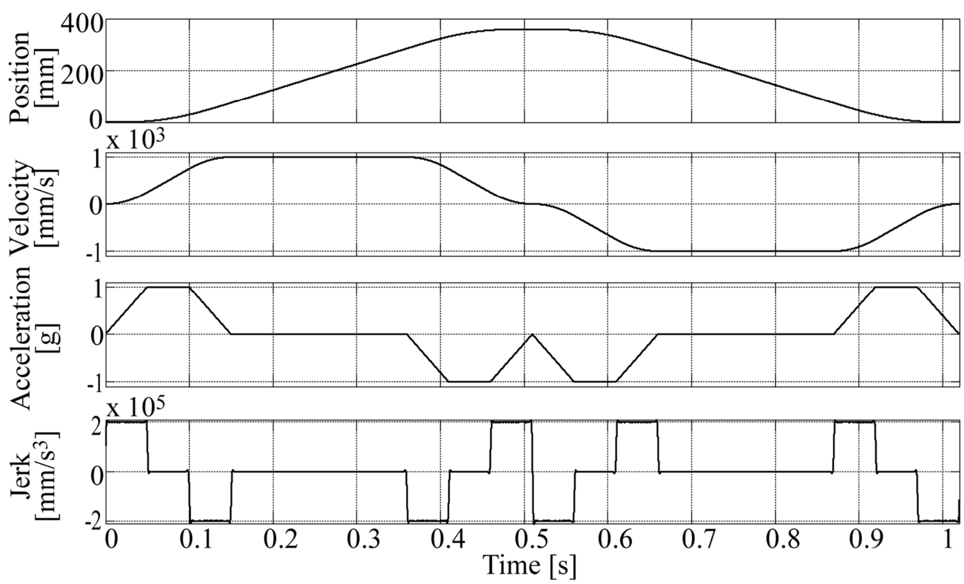


**Figure 4.6: Finite-Jerk Reference Command used in Simulation**

Figures 4.3 and 4.4 respectively show the simulated table tracking ($z_1/z_{1r}$) and table disturbance ($z_1/F_1$) FRFs of the drive controlled by the original MTEF and/or MCDADSC for the three scenarios discussed above. Figure 4.5 on the other hand shows the simulated response of the drive to a typical high speed motion command – a finite-jerk feed motion (Figure 4.6) with 360 [mm] displacement, 1000 [mm/s] velocity, 1 [g] acceleration and 200,000 [mm/s$^3$] jerk. From the plots, we see that the original MCDADSC combined with MTEF outperforms the original MCDADSC without the MTEF in the first two scenarios. In the third scenario where there is parameter mismatch, $\alpha = -2.7$ has to be used to scale $\hat{F}_1$ in order to obtain a good tracking response in Figure 4.5(c). However, as explained in Section 4.3.2, this deteriorates the low-frequency disturbance rejection ability of the original MCDADSC+MTEF as seen in Figure 4.4(c). Furthermore, in this particular case, the controller is destabilized by the additional feedback loop introduced by $\hat{F}_1$. To stabilize the controller, a low-pass filter (with a cut-off frequency of 50 [Hz]) is applied to $\hat{F}_1$ before injecting it into the MTEF. However, as a result of the low pass filtering, the original MCDADSC+MTEF is no longer able to suppress the mode at around 200 [Hz] (i.e. Mode 1) as seen by comparing Figure 4.4(c) to Figure 4.4 (a) and (b). Therefore, even though scaling and injecting $\hat{F}_1$ into the MTEF succeeds in improving the low-frequency tracking performance of the original MTEF+MCDADSC, it results in the loss of both low-frequency and high-frequency disturbance rejection performance. The stability of the controller is also adversely affected by the presence of $\hat{F}_1$ in the MTEF.

Figures 4.7 to 4.9 show the same three plots shown in Figures 4.3 to 4.5 but this time for the modified MTEF and/or MCDADSC. It is observed from Figure 4.7 and Figure 4.9 that the modified MCDADSC+MTEF also performs better than the modified MCDADSC without MTEF in all scenarios in terms of tracking. Furthermore, the MCDADSC+MTEF and the MCDADSC without MTEF are both able to achieve equally good low-frequency disturbance rejection even in the presence of parameter mismatch (Figure 4.8). The elimination of $\hat{F}_1$ from the MTEF also means that there is no additional feedback loop introduced in the modified MCDADSC+MTEF. This underscores the advantage of using the modified MTEF/MCDADSC over the original one. However, it is worth noting that the modified MCDADSC+MTEF is unable to suppress the Mode 1 (occurring at around 200 [Hz]). To suppress this mode, an accurate estimate of the disturbance force ($F_1$) has to be injected into the MTEF in the place of the $\hat{F}_1$ (which is tainted by un-modeled dynamics).

This could be achieved, for instance, by embedding a high-bandwidth force sensor between the nut and table to provide a more accurate measurement of $F_1$.

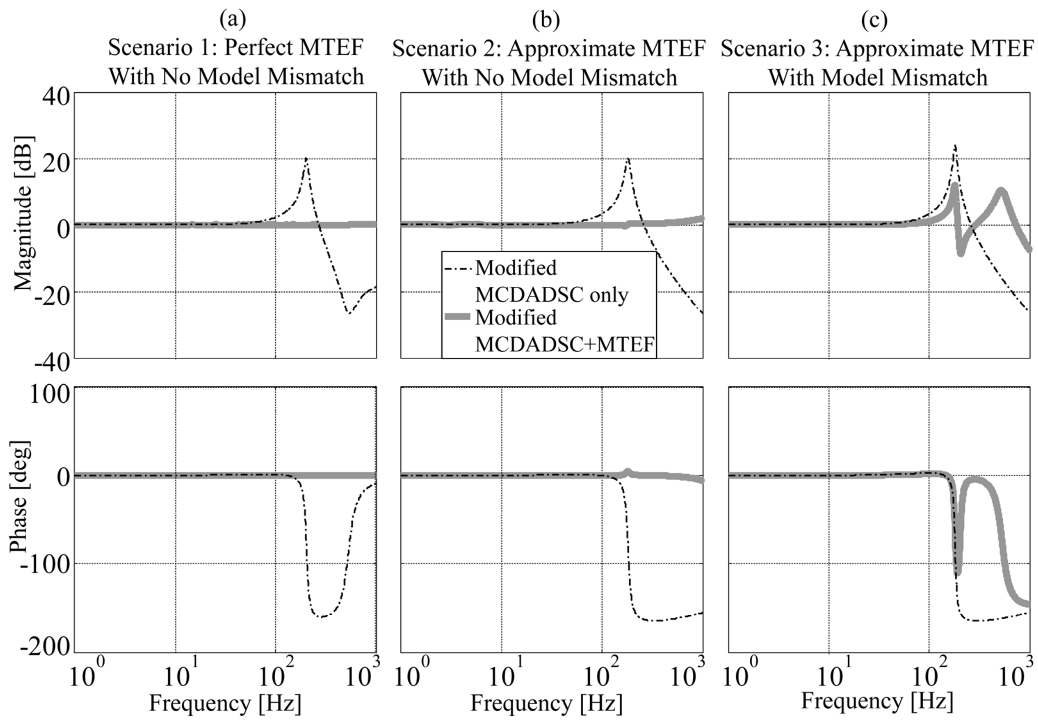


**Figure 4.7: Comparison of Simulated Table Tracking FRF ($z_1/z_{1r}$) of Modified MCDADSC Only and Modified MCDADSC+MTEF for Three Different Scenarios**

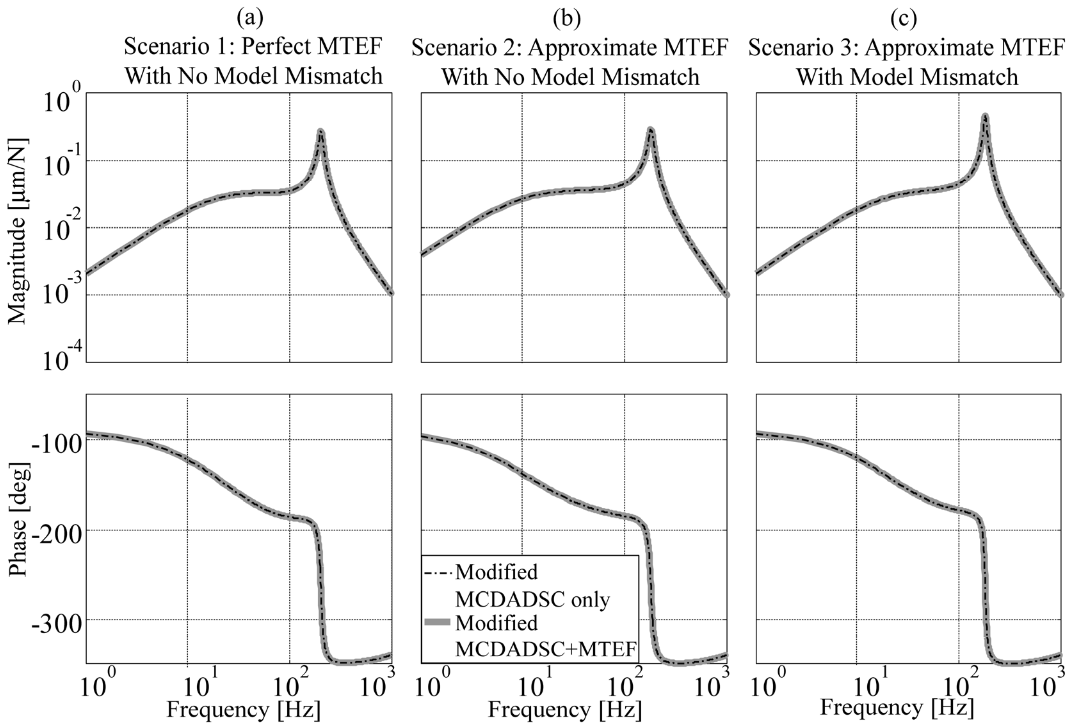


**Figure 4.8: Comparison of Simulated Table Disturbance FRF ($z_1/F_1$) of Modified MCDADSC Only and Modified MCDADSC+MTEF for Three Different Scenarios**

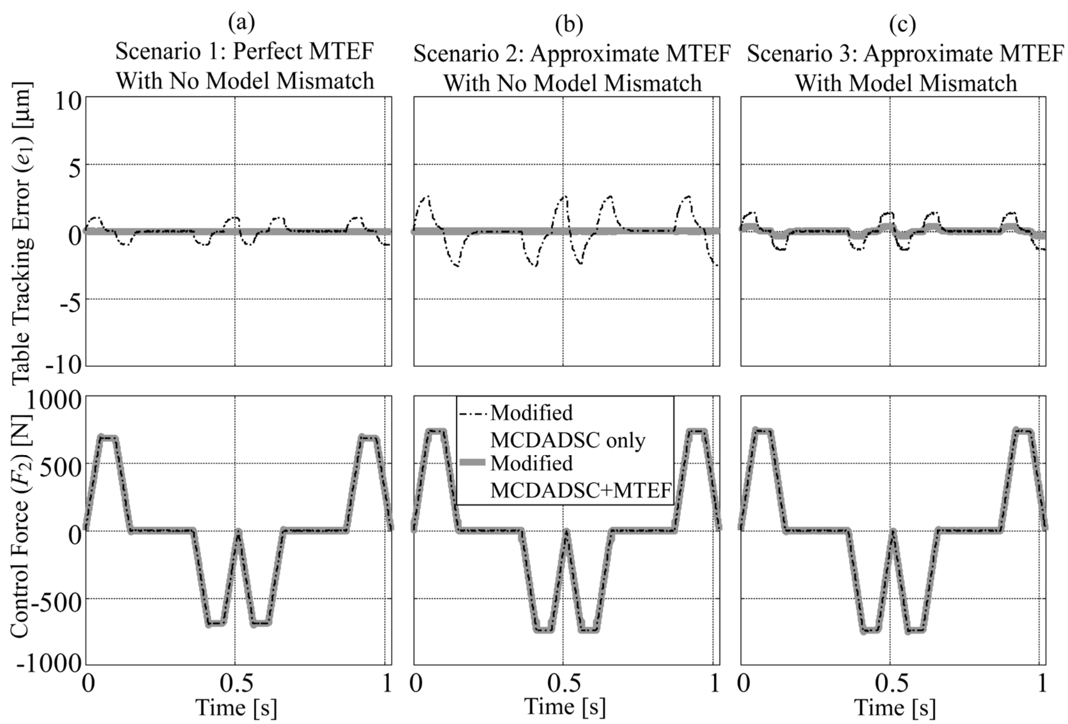


**Figure 4.9: Comparison of Simulated High Speed Trajectory Tracking Response of Modified MCDADSC Only and Modified MCDADSC+MTEF for Three Different Scenarios**

A final simulation test is conducted to demonstrate the influence of gain scheduling on the controller performance. The same finite-jerk feed motion used in Figures 4.5 and 4.9 is applied to the drive. However, this time, the drive parameters (i.e. the coefficients of **M**, **C** and **K**) are assumed to vary as a function of $X$ according to the graphs of Figure 3.25. Figure 4.10 compares the response of the drive controlled by the original and the modified MTEF+MCDADSC for the gain scheduled and non gain scheduled cases. The parameters used for both controllers are the same as those of Scenario 1 in Tables 4.1 and 4.2, respectively. From the figure, it is seen that gain scheduling reduces the tracking error in both cases without any significant difference in the required control energy.

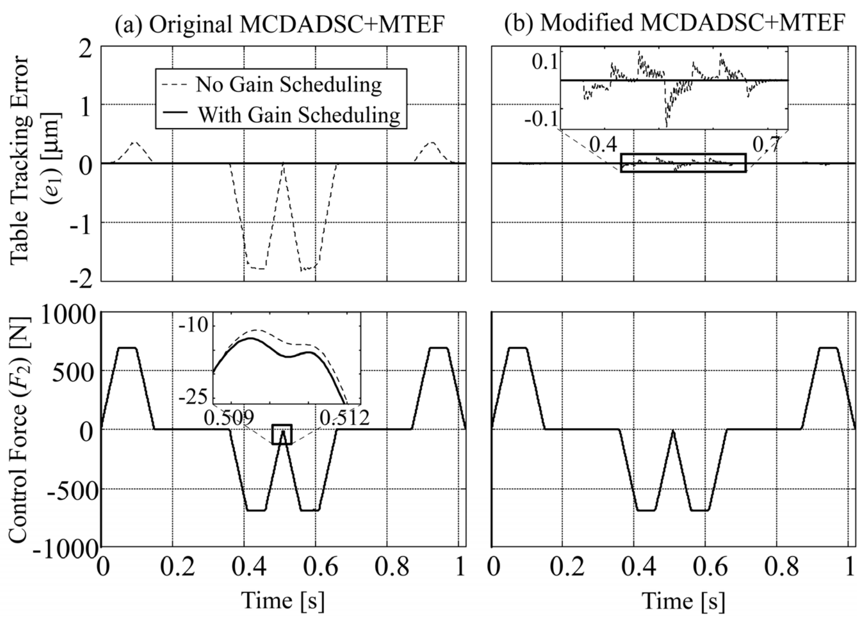


**Figure 4.10: Comparison of Simulated High Speed Trajectory Tracking Response of Original and Modified MTEF+MCDADSC with and without Gain Scheduling**

### 4.5.2 Experimental Tests: Practical Issues

The control laws presented in this chapter are verified experimentally on the test bed described in Section 3.4.1. In order to successfully implement the control laws on the test bed, two practical issues, i.e. friction and geometric errors of the ball screw drive, need to be compensated as follows:

**(A) Feed-Forward Friction Compensation**

Since the non-linear friction behavior of the test bed (Figure 3.23) was not included in the parameter identification performed in Section 3.5.5, it has to be pre-emptively canceled out using feed-forward control action. This is achieved by calculating the friction force ($F_f$) based on the desired velocity of the table (i.e. $z_{3r}$) and adding it to the MCDADSC control force ($F_2$) delivered to the motor. However, special care must be taken in incorporating $F_f$ into the MTEF. This is because $F_f$ is a distributed force. Some portion of $F_f$ results from the motor bearings while the other portion is mainly due to the nut and guideway bearings. As shown in Figure 4.11, this distribution is governed by the parameter $\eta$, where $0 \le \eta \le 1$. Since $\eta$ effects the table positioning error, it also determines the correct performance of the MTEF (compare Figure 4.11 with Figure 4.2). The MTEF can be made more accurate by adding $(1-\eta)F_f$ and $\eta F_f$ respectively to $\hat{F}_1$ and $F_2$ in Eq.(4.25).

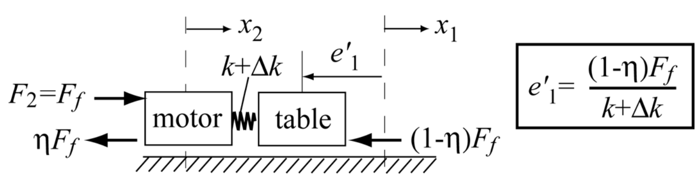


**Figure 4.11: Effect of Distributed Friction on Table Positioning Error**

Although $\eta$ is extremely difficult to determine analytically, it can be approximated experimentally using the original MTEF+MCDADSC. This is achieved by jogging the drive controlled by MTEF+MCDADSC back and forth at a constant velocity (so that $F_f$ is constant) and adjusting $\eta$ iteratively while monitoring the table tracking error $e_1$. If the drive is assumed to be accurately modeled then the correct value of $\eta$ is obtained when the table tracking error equals zero. Using this procedure, the value of $\eta$ is found to be 0.6 for the test bed.

**(B) Geometric Error Compensation**

Compensation of the imperfections of the ball screw assembly arising from straightness, lead, misalignment, flatness and other quasi-static geometric errors play an important role in the successful experimental implementation of the MCDADSC+MTEF. This is because such geometric errors are picked up by the linear encoder and misinterpreted as static deformations of the ball screw by the controllers. As presented in [40], these errors can be identified by moving the table back and forth (at a very slow speed) within its travel range and measuring the difference between $x_1$ and $x_2$:

$$v(X) = x_1 - x_2 \tag{4.51}$$

where $x_1$ and $x_2$ are respectively the measured displacement of the table and the measured equivalent linear displacement of the motor. $X$ is the position of the table within its travel range. Since $x_1$=$x_2$ during rigid-body motions, the difference $v(X)$ is taken as the cumulative geometric error in the measurement of table position $x_1$. The error is corrected by subtracting $v(X)$ from the measured position of the table $x_1$ and also from the reference position for the table $x_{1r}$, such that:

$$z_1 = x_1 - v(X); \;\; z_{1r} = x_{1r} - v(X) \tag{4.52}$$

Figure 4.12 shows the geometric error profile $v(X)$ measured from the test bed by jogging the table at a speed of 1 [mm/s]. As seen, the maximum value of $v$ is about 4.5 [µm] in the forward direction and then it is offset by about 1 [µm] in the reverse direction causing it to peak at 5.5 [µm]. The 1 [µm] offset is mainly due to a backlash-like motion loss at the nut during motion reversals [22], The measured geometric error profile, excluding the backlash-like effect, is represented using a 10$^{th}$ order polynomial in the implemented control laws.

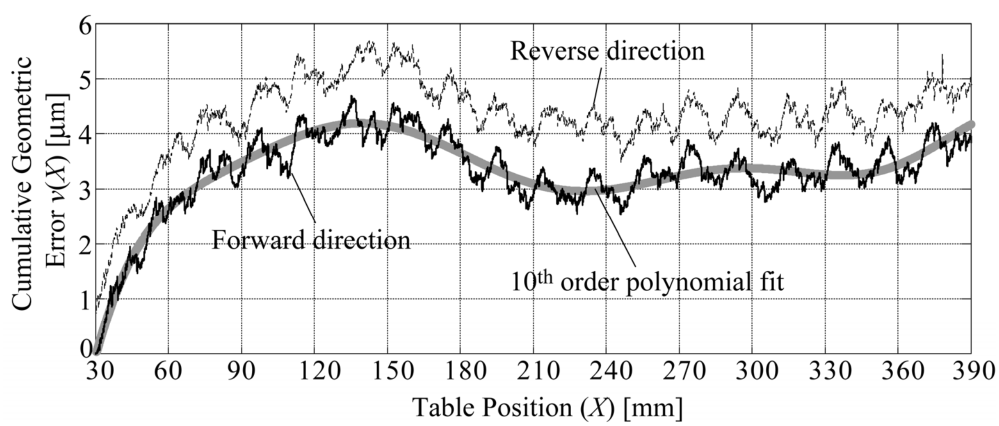


**Figure 4.12: Identified Geometric Error Profile of Test Bed**

### 4.5.3 Experimental Tests: Results

The real-time implementation of the control laws is achieved using a dSPACE 1103® dedicated control board at a sampling frequency of 20 [kHz] (i.e. $T$ = 50 [µs]). In all the experiments, feed-forward friction compensation and geometric error compensation are performed as described in the previous subsection. Except in the case of gain-scheduling, the original and modified MTEF and MCDADSC are designed using the matrices of Eq.(4.49) (i.e. the parameters of the test bed identified for $X$ = 30 [mm]). Tables 4.3 and 4.4 list the control parameters used for the original and modified MTEF and/or MCDADSC, respectively.

Figure 4.13 shows the tracking and disturbance FRFs of the original MTEF and/or MCDADSC measured with the table located at $X$ = 30 [mm]. As seen from Figure 4.13(a), the MCDADSC+MTEF is able to suppress the peak magnitude of Mode 1 from 14.5 [dB] (obtained with the MCDADSC alone) to 4.5 [dB]. Consequently, the bandwidth of the MCDADSC+MTEF is increased from 110 [Hz] to 142 [Hz]. However, in terms of disturbance rejection (Figure 4.13(b)), there is hardly any improvement obtained by using the MCDADSC+MTEF over the MCDADSC. Both of them are unable to achieve good disturbance rejection in both the low and high frequency regions because $\hat{F}_1$ is not included into the MTEF. $\hat{F}_1$ is not included into the MTEF because it destabilizes the MCDADSC+MTEF as a result of the additional feedback loop it introduces (see Figure 4.1).

Figure 4.14 shows the response of the drive controlled by the original MTEF and/or MCDADSC to a limited jerk motion command similar to the one in Figure 4.6. The only difference is that the jerk limit has been increased from 200,000 [mm/s$^3$] to 1,000,000 [mm/s$^3$] while the velocity limit has been reduced from 1000 [mm/s] to 450 [mm/s] which is the velocity limit of the test bed. The maximum table tracking error is 19.4 [µm] based on the original MCDADSC alone. When the MTEF is added on, maximum tracking error reduces to 16.3 [µm]. The relatively small improvement in tracking error by the MTEF is due to the severe vibrations at around 0.9 [s]. These vibrations occur due to the incorrect cancelation of Mode 1 by the controller when the table travels to $X$ = 390 [mm] because the controller is designed using the parameters for $X$ = 30 [mm]. As shown in Figure 4.15, when gain scheduling is performed using the identified parameters of Figure 3.25, the vibrations around 0.9 [s] are damped. Consequently, the maximum tracking error of the MCDADSC+MTEF decreases to 8.6 [µm].

It is also worth highlighting the large errors in the estimated disturbance force ($\hat{F}_1$) shown in Figure 4.14 and Figure 4.15. The only disturbance force on the drive is the identified friction dynamics of Figure 3.23. Since this friction dynamics is canceled out in feed-forward, the estimated disturbance force ($\hat{F}_1$) should be close to zero. However, from the plots, the estimated forces are observed to be up to 1000 [N], which indicates the influence of un-modeled dynamics in $\hat{F}_1$. This is the reason why $\hat{F}_1$ has not been injected into the MTEF because destabilizes the controller. Even when it is low-pass filtered and injected into the MTEF, it deteriorates the performance of the controller instead of improving it.

| Parameter | Value |
|---|---|
| $\lambda_1$ | 0 [1/s] |
| $\lambda_2$ | 550 [1/s] |
| $\lambda_3$ | 0.1 |
| $\lambda_4$ | 1 |
| $K$ | 450 [1/s] |
| $g_1$ | 40,000 [kg/s] |
| $T$ | 50 [μs] |
| $r$ | $-b_{12}/b_{22}$ |
| $r^*$ | N/A |
| $\alpha$ | 0 |

**Table 4.3: Parameters used in Experimental Tests for Original MCDADSC and MTEF**

| Parameter | Value |
|---|---|
| $\lambda_1$ | 0 [1/s] |
| $\lambda_2$ | 550 [1/s] |
| $\lambda_3$ | 0.1 |
| $\lambda_4$ | 1 |
| $\lambda'$ | 550 [1/s] |
| $K$ | 450 [1/s] |
| $g_1$ | 10,000 [kg/s] |
| $T$ | 50 [μs] |
| $r$ | $-b_{12}/b_{22}$ |
| $r^*$ | N/A |
| $\alpha$ | N/A |

**Table 4.4: Parameters used in Experimental Tests for Modified MCDADSC and MTEF**

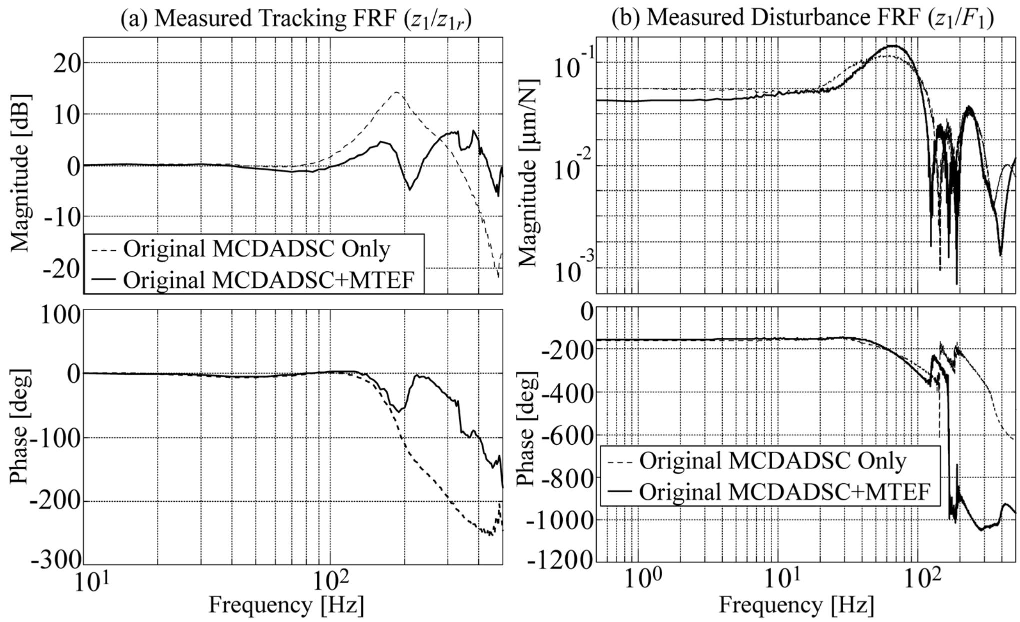


**Figure 4.13: Comparison of (a) Measured Tracking FRF (b) Measured Disturbance FRF of Test Bed Controlled using Original MCDADSC Only and Original MCDADSC+MTEF. Measurement Taken with Table Located at X = 30 [mm]**

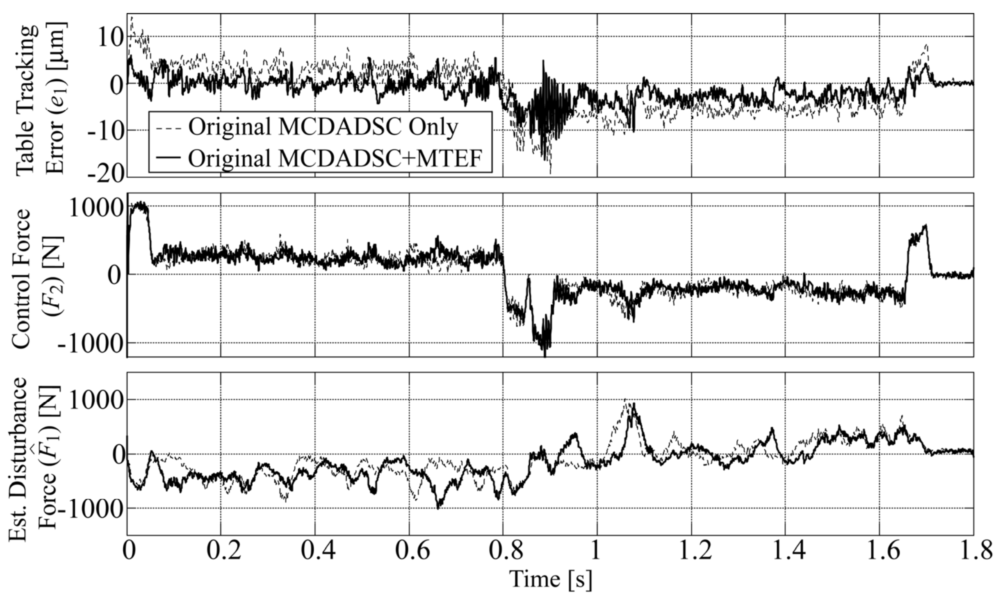


**Figure 4.14: Comparison of Measured High Speed Trajectory Tracking Response of Original MCDADSC Only with Original MTEF+MCDADSC**

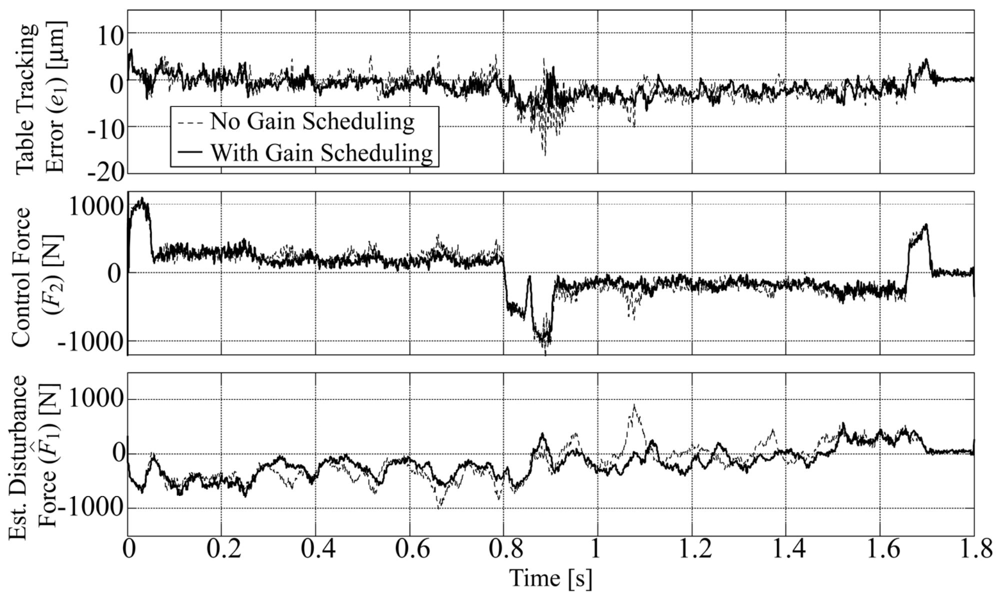


**Figure 4.15: Comparison of Measured High Speed Trajectory Tracking Response of Original MTEF+MCDADSC with and without Gain Scheduling**

Figure 4.16 to Figure 4.18 show the same plots shown in Figure 4.13 to Figure 4.15 but this time for the modified MTEF and/or MCDADSC. The measured tracking FRF of Figure 4.16(a) indicates that the modified MCDADSC+MTEF is also able to suppress the peak amplitude of Mode 1. Its amplitude is 20 [dB] when the test bed is controlled by the modified MCDADSC alone. When the MTEF is added on, Mode 1 is completely damped out thereby increasing the usable frequency range of the controller from 154 [Hz] to about 269 [Hz] based on the +3 [dB] crossing. The disturbance FRF of Figure 4.16(b) shows the significant improvement in low-frequency disturbance rejection in the modified MCDADSC+MTEF and the MCDADSC only compared to the original ones (Figure 4.13(b)). However, neither controller is able to suppress Mode 1 in the disturbance FRF of Figure 4.16(b). As mentioned in Section 4.5.1, the suppression of Mode 1 in the disturbance FRF can be achieved by measuring $F_1$ accurately using a force sensor and injecting it into the MTEF in the place of $\hat{F}_1$.

The tracking FRF of Figure 4.16(a) shows that there is a little bit of overcompensation by the MTEF around 100 [Hz] which causes the tracking FRF of the modified MTEF+MCDADSC to drop to -7 [dB] before rising back to 0 [dB]. This loss of performance is attributed to the low feedback gain $K$ of the secondary sliding surface. This means that the modified MCDADSC is not able to track $z_{2r}$ very well thereby leading to loss of performance in the MTEF+MCDADSC. The problem can be mitigated by increasing $K$ but then the gains of the primary sliding surface ($g_1$ and $g_2$) will have to be reduced to maintain the overall gain of the closed-loop system. Decreasing $g_1$ and $g_2$ will, on the other hand, sacrifice the disturbance rejection capability of the controller. This is the design trade off of using the modified MCDADSC+MTEF. Again, this design trade off can be reduced by injecting an accurate measurement of $F_1$ into the MTEF so that the MCDADSC can be tuned to focus more on trajectory tracking.

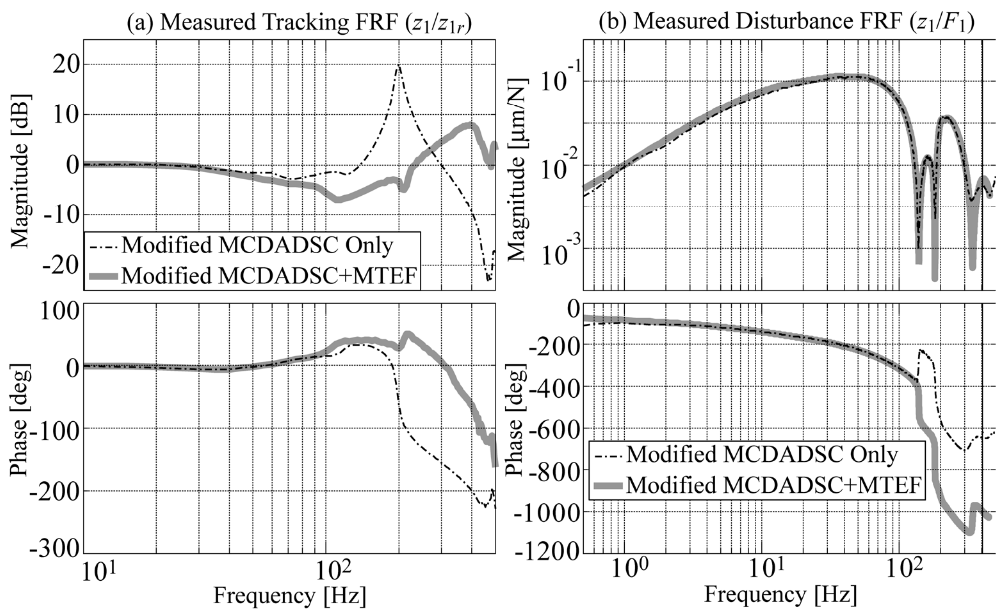


**Figure 4.16: Comparison of (a) Measured Tracking FRF (b) Measured Disturbance FRF of Test Bed Controlled using Modified MCDADSC Only and Modified MCDADSC+MTEF. Measurement Taken with Table Located at X = 30 [mm]**

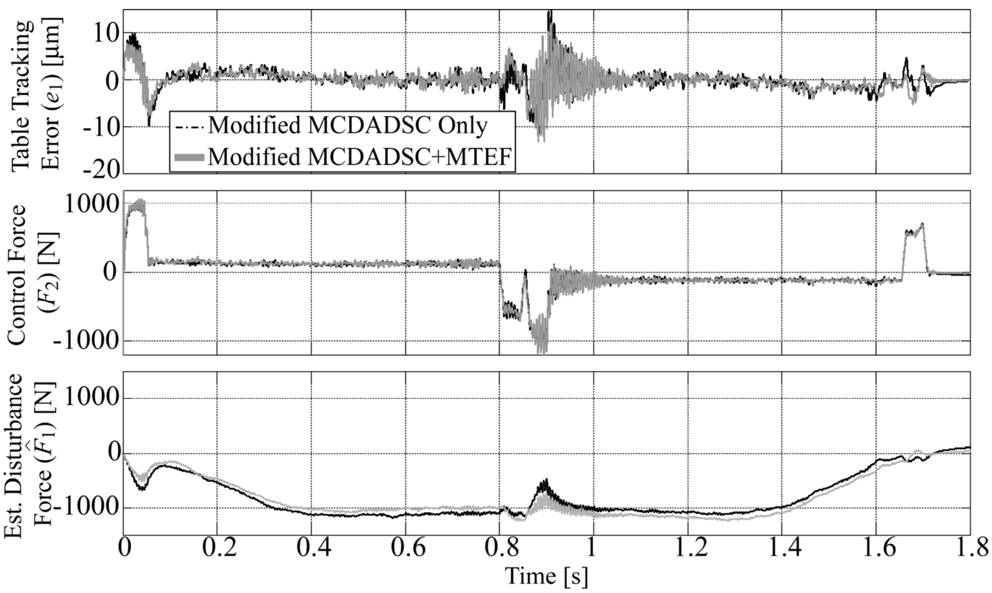


**Figure 4.17: Comparison of Measured High Speed Trajectory Tracking Response of Modified MCDADSC Only with Modified MTEF+MCDADSC**

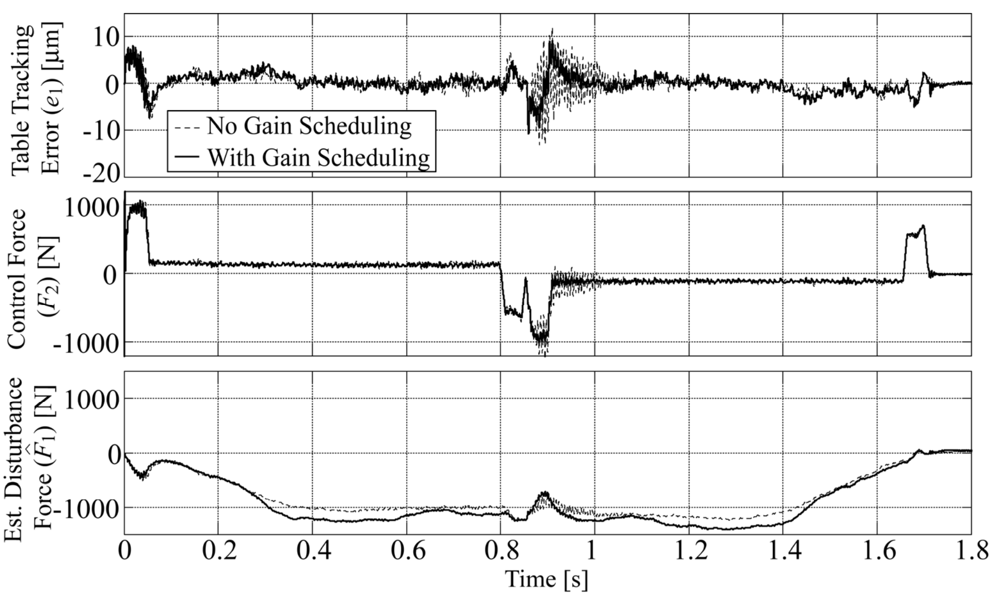


**Figure 4.18: Comparison of Measured High Speed Trajectory Tracking Response of Modified MTEF+MCDADSC with and without Gain Scheduling**

From the high speed trajectory tracking response of Figure 4.17, the modified MCDADSC+MTEF and the MCDADSC without the MTEF are seen to perform very similarly. The maximum tracking error of the MCDADSC is 14.63 [μm] while that of the MCDADSC+MTEF is 13.27 [μm]. Again, an excitation of Mode 1 is noticed when the table reaches $X$ = 390 [mm] as a result of the parameter mismatch between the controller (designed for $X$ = 30 [mm]) and the plant. Similar to the case of the original MCDADSC+MTEF, when gain scheduling is implemented, this vibration of Mode 1 is damped out as seen in Figure 4.18. The tracking error of the gain-scheduled modified MCDADSC+MTEF is 11.02 [μm]. Again, this error can be reduced by increasing $K$ which increases the ability of the MTEF to counteract the static deformations that occur during acceleration/deceleration motions of the table.

### 4.6 Summary

This chapter has presented a mode-compensating disturbance adaptive discrete-time sliding mode controller (MCDADSC) combined with a minimum tracking error filter (MTEF) for effectively controlling ball screw drives with structural flexibility. It has shown theoretically that the MCDADSC alone cannot achieve accurate tracking without including the MTEF. The MTEF is a plant inversion-based feed-forward filter which becomes unstable when the plant possesses non-minimum phase zeros. A method for designing stable and effective MTEF in the presence of non-minimum phase zeros (which are common in flexible ball screw drives) is proposed. Theoretical analysis is also conducted to show that the MCDADSC+MTEF loses its disturbance rejection ability and becomes non-robust in the presence of un-modeled dynamics. Therefore, it is modified slightly such that its robustness and low-frequency disturbance rejection ability is improved even when there is model uncertainty. Moreover, an ad-hoc gain scheduling method is added on to the MCDADSC+MTEF to further improve its performance when the dynamics of the ball screw drive varies in a known fashion as a function of the table's position.

Simulation and experimental tests are used to demonstrate the improvement gained by adding the MTEF to the MCDADSC. The improved robustness and low-frequency disturbance rejection performance gained by using the modified MCDADSC combined with MTEF over the original one are also highlighted through the tests. Finally the benefits of incorporating gain scheduling into the controller are demonstrated.

One drawback of the modified MCDADSC+MTEF is its inability to achieve high-frequency disturbance rejection around the flexible mode of the ball screw. This shortcoming can be eliminated by accurately measuring the disturbance force applied to the table via a high-bandwidth dynamometer or an embedded force sensor and incorporating it into the controller through the MTEF. This also has the potential of further improving the tracking performance of the modified MCDADSC+MTEF by allowing it to focus more on trajectory tracking rather than disturbance rejection. It is also noteworthy that the ad-hoc gain scheduling method, even though effective, does not have theoretically guaranteed stability conditions. Its stability can only be assured by testing it rigorously via simulation and experiments under various operating conditions that the ball screw drive is likely to be subjected to.

# Chapter 5

## Dynamic Stiffness Enhancement of Direct Drives using Sliding Mode Control with True Disturbance Recovery

### 5.1 Overview

Direct drives possess a major drawback compared to ball screw drives due to their lack of dynamic stiffness from the mechanical structure of the machine.

In this chapter, a disturbance adaptive discrete-time sliding mode controller is designed for feed drives equipped with linear motor direct drives. The designed sliding mode controller is shown to be very simple to implement but at the same time more effective than similar controllers in increasing the dynamic stiffness of direct-driven machines. True disturbance force recovery is also introduced as a means of obtaining better estimates of the friction and cutting forces applied to the linear motor. The recovered disturbance forces are used to actively compensate low-frequency machine tool structural modes which are within the bandwidth of the controller. As a result, the dynamic stiffness of the drive, between the tool and workpiece, is further improved. The merits of the disturbance adaptive sliding mode controller with true force recovery are demonstrated experimentally on a high speed linear drive.

The rest of the chapter is organized as follows. Section 5.2 explains the controller design and highlights the similarities and differences between the proposed controller design and similar controllers used for direct drives. Section 5.3 then presents the concept of true disturbance recovery and its application to active vibration of low-frequency machine tool structural modes. Finally Section 5.4 presents the experimental results followed by a summary of the chapter in Section 5.5.

### 5.2 Controller Design

As explained in Chapter 1, linear motor direct drives have very simple mechanical designs. They essentially consist of the table (forcer) attached to the machine tool frame (stator) by linear bearings. Consequently, the structural dynamics of the mechanical system do not play as much of a role in direct drives as they do in ball screw drives. Direct drives are therefore modeled as rigid bodies with mass $m$ and viscous damping $b$ according to the equation:

$$m\ddot{x} + b\dot{x} = F_m(t) + F_d(t) \tag{5.1}$$

where $x$, $\dot{x}$ and $\ddot{x}$ are the actual position, velocity and acceleration of the drive while $F_m$ and $F_d$ are the linear motor force and disturbance cutting forces, respectively. The position error ($e_x = x_r - x$) and velocity error of the drive ($e_v = \dot{x}_r - \dot{x}$) can be represented in discrete time intervals $T$ by applying backward Euler approximation:

$$\left.\begin{aligned} e_x(k) &= e_x(k-1) + Te_v(k) \\ e_v(k) &= e_v(k-1) + \frac{T}{m}\left(m\ddot{x}_r + b\dot{x}(k) - F_m(k) - F_d(k)\right) \end{aligned}\right\} \tag{5.2}$$

where $k$ is the discrete time step counter while $x_r$, $\dot{x}_r$ and $\ddot{x}_r$ are the reference position, velocity and acceleration, respectively.

### 5.2.1 Disturbance Adaptive Discrete-Time Sliding Mode Controller (DADSC)

The disturbance adaptive discrete-time sliding mode controller (DADSC) [83], introduced in the previous chapter, is reformulated here for direct drive control. This is done by designing a first-order sliding surface $s(k)$ such that it minimizes both position and velocity errors as [5][83]:

$$s(k) = \lambda e_x(k) + e_v(k) \tag{5.3}$$

where $\lambda$ is a gain indicating the bandwidth of the controller. The control force can be obtained by minimizing a Lyapunov function using a similar method as presented previously in [5][40][83]:

$$F_m(k) = m\ddot{x}_r(k) + mKs(k) - \hat{F}_d\left(k\right) + b\dot{x}(k) + m\lambda e_v(k) \tag{5.4}$$

where $K$ is a feedback gain and $\hat{F}_d\left(k\right)$ is the estimated disturbance force given by the discrete-time transfer function:

$$\hat{F}_d(k) = -\left(\frac{g_1 z - g_2}{z-1}\right)s(k) \tag{5.5}$$

with tunable adaptation gains $g_1$ and $g_2$. Substituting Eqs. (5.2), (5.4) and (5.5) into Eq.(5.3) and simplifying the result yields the sliding surface dynamics of the closed-loop system as:

$$\begin{Bmatrix} s(k) \\ \hat{F}_d(k) \end{Bmatrix} = \frac{1}{Q+g_1 R}\left(\begin{bmatrix} 1+g_2 R & R \\ g_2 Q - g_1 & Q \end{bmatrix}\begin{Bmatrix} s(k-1) \\ \hat{F}_d(k-1) \end{Bmatrix} + \begin{Bmatrix} -R \\ g_1 R \end{Bmatrix} F_d(k)\right) \tag{5.6}$$

where $Q = 1+KT;\ R = m^{-1}T$. The term $g_2 Q - g_1$ in Eq.(5.6) determines the coupling between the disturbance force estimation and the sliding surface. It is eliminated by selecting $g_2 = Q^{-1} g_1$. This selection of $g_2$ constitutes the main difference between the DADSC and the adaptive sliding mode control (ASMC) as will be explained in the next subsection.

### 5.2.2 Adaptive Sliding Mode Control (ASMC)

The adaptive sliding mode controller (ASMC) [5][69] is very similar to the DADSC presented in the previous subsection. The only difference is the disturbance adaptation law which is given as:

$$\hat{F}_d(k) = -\left(\frac{g_1 z}{z-1}\right)s(k) \tag{5.7}$$

As a result of this definition of $\hat{F}_d$, the closed-loop sliding surface dynamics expressed in Eq.(5.6) for the DADSC becomes:

$$\begin{Bmatrix} s(k) \\ \hat{F}_d(k) \end{Bmatrix} = \frac{1}{Q+g_1 R}\left(\begin{bmatrix} 1 & R \\ -g_1 & Q \end{bmatrix}\begin{Bmatrix} s(k-1) \\ \hat{F}_d(k-1) \end{Bmatrix} + \begin{Bmatrix} -R \\ g_1 R \end{Bmatrix} F_d(k)\right) \tag{5.8}$$

for the ASMC. In other words $g_2$ = 0 in the ASMC. Therefore, the $g_2 Q - g_1$ term in the DADSC becomes simply $-g_1$ in the ASMC. The effects of this difference on the performance of the ASMC compared to the DADSC will be explored in later sections.

### 5.2.3 Cascaded Controller (CC)

The widely used cascaded controller (CC) [62][63] consists of cascaded velocity and position loops as shown in Figure 5.1. The velocity loop is closed using a proportional integral (PI) while the position loop is closed using a proportional (P) controller. Velocity and acceleration feed-forward loops are also included in order to improve the reference tracking accuracy. $K_v$, $K_p$ and $T_i$ are the gains of the CC controller shown in Figure 5.1.

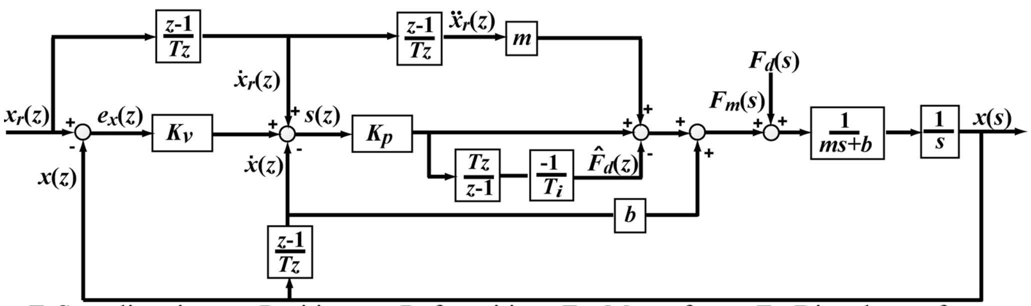


T: Sampling time; x: Position; $x_r$: Ref. position; $F_m$: Motor force; $F_d$: Disturbance force

**Figure 5.1: Block Diagram of P-PI Cascaded Controller with Velocity and Acceleration Feed-Forward**

From the block diagram of Figure 5.1, the closed-loop dynamics of the CC is found in a similar form as in the DADSC:

$$\begin{Bmatrix} s(k) \\ \hat{F}_d(k) \end{Bmatrix} = \frac{1}{Q' + g_1' R}\left( \begin{bmatrix} 1 & R \\ -g_1' & Q' \end{bmatrix} \begin{Bmatrix} s(k-1) \\ \hat{F}_d(k-1) \end{Bmatrix} + \begin{Bmatrix} -R \\ g_1' R \end{Bmatrix} F_d(k) + \begin{Bmatrix} K_v T \\ -g_1' K_v T \end{Bmatrix} e_v(k) \right) \tag{5.9}$$

where $Q' = 1 + m^{-1} K_p T;\ g_1' = T_i^{-1} K_p T$ .

### 5.2.4 Theoretical Comparison of CC, ASMC and DADSC

Comparing the dynamics of the CC (Eq.(5.9)) to those of the ASMC (Eq.(5.8)) and DADSC (Eq.(5.6)), it is observed that the velocity error term, $e_v(k)$, is not completely cancelled out of the closed-loop dynamics of the CC. The presence of $e_v(k)$ in the CC's closed-loop dynamics introduces errors in both its sliding surface ($s(k)$) and its estimated disturbance force ( $\hat{F}_d(k)$ ).

Furthermore, it is observed that the cross-coupling term $g_2 Q - g_1$ in the DADSC's dynamics is replaced by $-g_1$ in both the ASMC and CC. This means that in the latter two controllers, the disturbance estimation $\hat{F}_d(k)$ cannot be decoupled from the equivalent sliding surface $s(k)$ except if the disturbance estimation is turned off (i.e. $g_1 = 0$).

For the purpose of analytical comparison, it is assumed that the drive is ideal and well represented by Eq.(5.2). Under this assumption, the drive position tracking transfer function (TF), $x(z)/x_r(z)$, is unity for all three controllers. However, the disturbance transfer function, $x(z)/F_d(z)$, for the three controllers is given by:

$$\frac{x(z)}{F_d(z)} = \frac{T^2 z^2 (z-1)}{m(z-1)^2 (r_1 z - 1) + r_2 T z (z-1)(r_3 z - 1) + T z (r_4 z - r_5)(r_3 z - 1)} \tag{5.10}$$

The coefficients $r_1$ to $r_5$ for the CC, ASMC and DADSC are summarized in Table 5.1.

| Coefficient | CC | ASMC | DADSC |
|---|---|---|---|
| $r_1$ | 1 | $\lambda T$+1 | $\lambda T$+1 |
| $r_2$ | $K_p$ | $mK$ | $mK$ |
| $r_3$ | $K_v T$+1 | $\lambda T$+1 | $\lambda T$+1 |
| $r_4$ | $K_p T/T_i$ | $g_1$ | $g_1$ |
| $r_5$ | 0 | 0 | $Q^{-1} r_4$ |

**Table 5.1: Definition of Coefficients of Disturbance Transfer Function (Eq.(5.10)) for the CC, ASMC and DADSC**

First, to investigate the difference between the CC and the two sliding mode controllers as a result of the uncancelled $e_v(k)$ term in the CC, the disturbance adaptation gain, $r_4$, is set to zero. The feedback gain, $r_2$, is then increased steadily while keeping the other parameters constant. As $r_2$ is increased, the poles of the disturbance TF of the CC begin to leave the real axes (in other words they become under-damped), see Figure 5.2(a). However, no matter how much $r_2$ is increased, the disturbance TF poles of the two SMCs remain over-damped and never leave the real-axis. As seen from the disturbance Bode plot (Figure 5.2(b)) this makes the CC more susceptible to disturbances than the two SMCs.

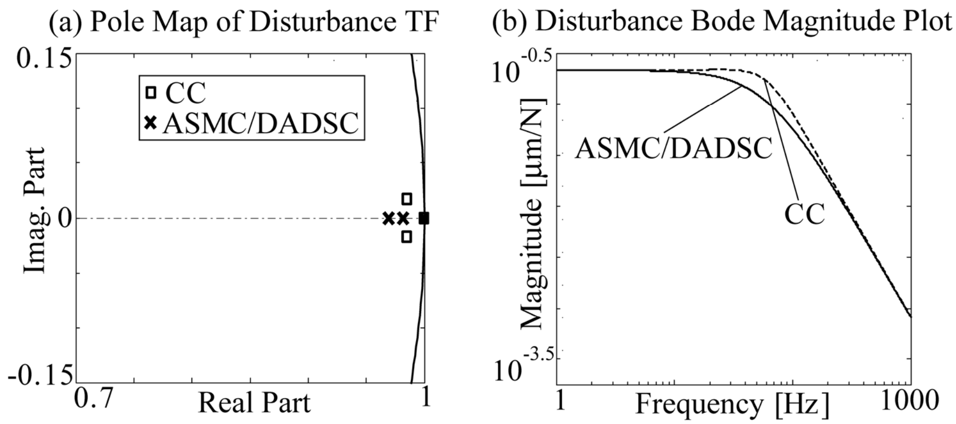


**Figure 5.2: Pole Map and Bode Magnitude Plot of Disturbance Transfer Function of the CC, ASMC and DADSC Showing Adverse Effect of Uncancelled Velocity Error Term ($e_v(k)$) on the Dynamics of the CC**

Next, the influence of decoupling the disturbance estimation from the sliding surface in DADSC is investigated by keeping $r_1$, $r_2$ and $r_3$ constant while the disturbance adaptation gain, $r_4$, is increased steadily. This time it is observed that the disturbance TF poles of the ASMC also leave the real axes while those of the DADSC remain over-damped no matter how high $r_4$ is set (Figure 5.3(a)). This makes the DADSC to have the greatest resistance to disturbances compared to the ASMC and the CC as shown in Figure 5.3(b).

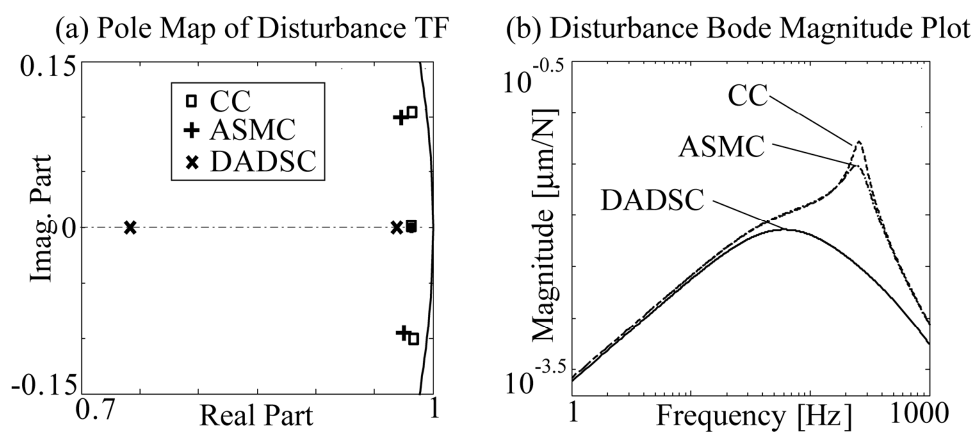


**Figure 5.3: Pole Map and Bode Magnitude Plot of Disturbance Transfer Function of the CC, ASMC and DADSC Showing Adverse Effect of Coupled Sliding Surface and Disturbance Estimation on the Dynamics of the CC and ASMC**

## 5.3 Disturbance Recovery and its Application to Active Vibration Control

Although the DADSC has better disturbance rejection than the ASMC and CC, it has a gain-dependent bandwidth which is often too low to be useful for practical purposes. Therefore, its disturbance estimation property is improved using the disturbance recovery (DR) algorithm presented here. The 'true' disturbance force $F_d(k)$ is extracted from Eq.(5.6) and expressed as a function of the estimated disturbance $\hat{F}_d(k)$ as:

$$F_d(k) = \frac{1}{g_1 R}\left( \left(Q + g_1 R\right)\hat{F}_d(k) - \underbrace{\left(g_2 Q - g_1\right)}_{0} s(k-1) - Q\hat{F}_d(k-1) \right) \tag{5.11}$$

The coefficient of $s(k\text{-}1)$ is zero in the DADSC because $g_2 = Q^{-1} g_1$. Since the 'true' disturbance here is not exactly the same as the actual one due to factors like modeling errors, it is called the 'recovered' disturbance, $F_{dR}$, in this thesis. The transfer function that recovers the disturbance from the estimated one is evaluated from Eq.(5.11) as:

$$\frac{F_{dR}(z)}{\hat{F}_d(z)} = \frac{(Q + g_1 R)z - Q}{g_1 R z} \tag{5.12}$$

This disturbance recovery transfer function essentially converts the low-bandwidth and controller gain-dependent disturbance force estimate of the DADSC ($\hat{F}_d(k)$) to a higher-bandwidth disturbance force ($F_{dR}(k)$) which is theoretically gain-independent. Consequently, $F_{dR}$ is more useful in practical feed drive applications, such as cutting force prediction from linear motor current and active vibration control of machine tool structural modes.

Low-frequency modes originate from the vibration of large components of machine tools such as columns and beds. Their resonance frequency is usually less than 100 [Hz] and they may be excited during high accelerations or machining at low speeds [17]. The DADSC with disturbance recovery can be used to actively compensate such low-frequency modes as shown in Figure 5.4. The transfer function $G_m(s)$ of the machine tool's structural mode must be measured and its parameters must be identified – which is a relatively straightforward procedure in practice. Then, the discrete-time equivalent of $G_m(s)$ is generated as $G_m(z)$. By applying the recovered disturbance $F_{dR}(z)$ to $G_m(z)$, the predicted machine tool vibrations,

$x_{m\_comp}(z)$, are computed and added to the reference command sent to the controller (i.e. feed-forward compensation). As the machine tries to follow this modified reference command, it indirectly reduces the relative vibration between the tool and workpiece, $x_{tcp}(s)$, thereby improving the dynamic stiffness of the machining process and the surface quality of the machined part. This strategy makes it possible to achieve a robust feed drive controller with high bandwidth and strong cutting force disturbance rejection ability, while reducing the machine tool vibrations during low speed metal cutting using the same linear motor.

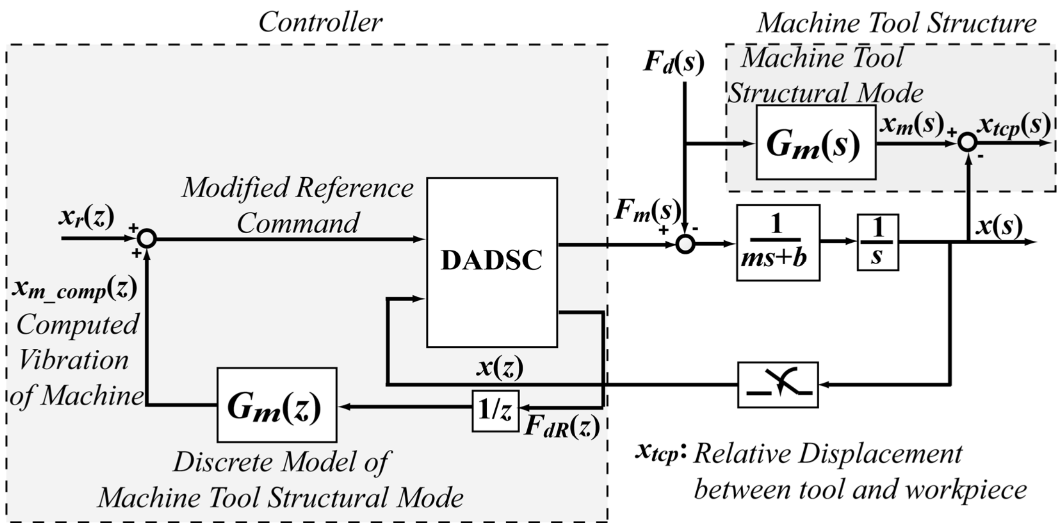


**Figure 5.4: Block Diagram of Proposed Active Damping Technique for Low-Frequency Machine Tool Structural Modes using the DADSC with Disturbance Recovery**

### 5.4 Experimental Validation

A high speed Siemens direct drive test bed shown in Figure 5.5 is used for evaluating the performance of the control and disturbance force prediction presented in this article. All the control algorithms have been applied to the main slider which can achieve speeds of up to 200 [m/min]. The open-loop Bode magnitude plot of the drive from motor force ($F_m$) to table position ($x$) is shown in Figure 5.6. As seen from the plot, the drive's behavior is dominated by rigid-body dynamics until about 400 [Hz] where a resonant is observed. Experimental modal analysis conducted on the table reveals that the mode observed at about 400 [Hz] is a yaw mode originating from the guideway joint of the table (similar to Mode 3 of the ball screw drive – see Figure 3.21). As discussed in Section 3.4, such guideway modes can easily be pushed out of the frequency range of interest by adding stiffness to the guideway joint. Therefore, only the rigid-body dynamics of the drive is considered for the linear drive. The moving mass and viscous damping constant of the drive are identified from time-domain data (using the method of Section 3.5.5) as $m$ = 31 [kg] and $b$ = 52.5 [kg/s].

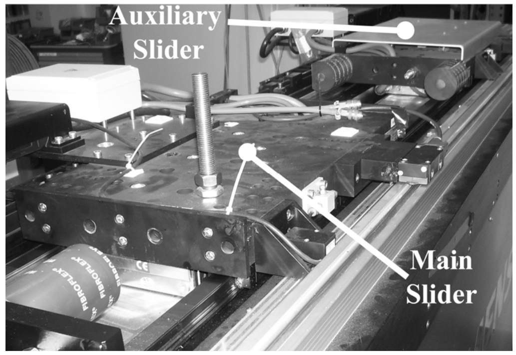


**Figure 5.5: Single-Axis High Speed Direct Drive Test Bed**

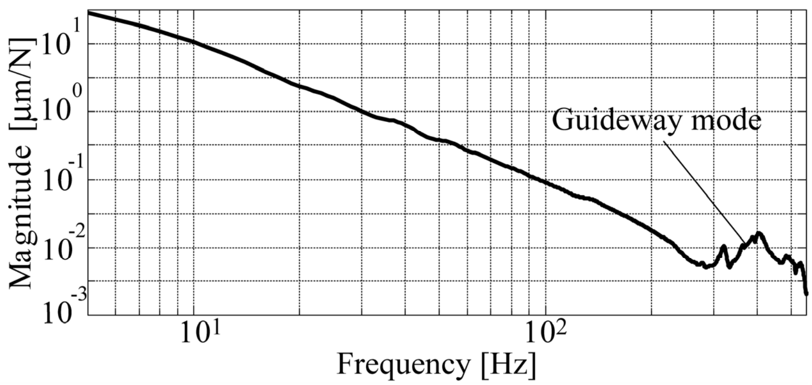


**Figure 5.6: Disturbance Bode Magnitude Plot of Open-loop Dynamics of Direct Drive Test Bed (i.e. from Force applied to Table to Displacement Measured from Table)**

All three controllers discussed in Section 5.2 are implemented using dSPACE® at a sampling frequency of $T$ = 62.5 [μs]. The parameters for each of the controllers are summarized in Table 5.2.

| **Parameters** | **Controllers** | | |
|---|---|---|---|
| | CC | ASMC | DADSC |
| $K_v$ [1/s] | 600 | N/A | N/A |
| $K_p$ [kg/s] | 30,000 | N/A | N/A |
| $T_i$ [ms] | 7.5 | N/A | N/A |
| $\lambda$ [1/s] | N/A | 300 | 300 |
| $K$ [1/s] | N/A | 500 | 500 |
| $g_1$ [kg/s] | N/A | 500 | 20,000 |

**Table 5.2: Controller Parameters used in Experiments for the CC, ASMC and DADSC**

### 5.4.1 Tracking Tests

Figure 5.7 shows the closed-loop tracking Bode plot for the three controllers. The controllers have all been tuned to have very high closed-loop bandwidths (greater than 100 [Hz]). Consequently, they have a large resonance (resulting from the controller dynamics) at around 110 [Hz]. However, since the reference input for the controller is generated internally in the CNC (computer numerical controller), it can easily be adjusted or shaped to prevent it from exciting such resonance dynamics [37][45][81].

To demonstrate the tracking performance of the controllers in time-domain, a finite-jerk feed motion (similar to the one shown in Figure 4.6) with 350 [mm] displacement, 1800 [mm/s] velocity, 1.5 [g] acceleration and 200,000 [mm/s$^3$] jerk is used as a reference position command for the table. Figure 5.8 shows the reference position command, reference tracking errors and motor force of the DADSC. The results of the other two controllers are omitted because, for the most part, there is no significant difference between the DADSC and the other two in terms of tracking (as also deduced from the Bode Plot of Figure 5.7). All three controllers have a maximum tracking error of about 6 [µm] during the entire motion.

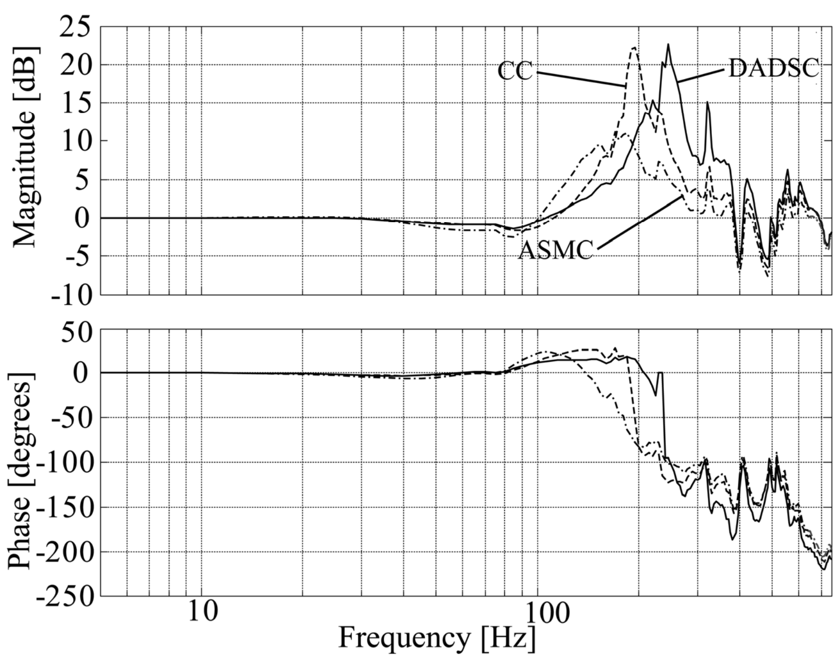


**Figure 5.7: Reference Tracking Bode Plots ($x(z)/x_r(z)$) for the CC, ASMC and DADSC**

The only difference between the responses of the three controllers is that, in the DADSC, when the table reaches the commanded position, it begins to oscillate wildly and so does not settle to the desired position. One of the methods of dealing with this problem, as suggested in [45], is to schedule the disturbance adaptation gain, $g_1$, of the DADSC as a function of reference velocity. The idea is to keep $g_1$ low when the reference velocity is high (i.e. during rapid traverse) so that its high frequency content does not excite the resonance dynamics of the controller, and then increase the gains proportionately as the table approaches the desired position and the reference velocity decreases. In this particular case the gains have been scheduled linearly from $g_1$ = 2,500 [kg/s] when the velocity is highest (i.e. 1800 [mm/s]) to $g_1$ = 20,000 [kg/s] when the velocity lowest (i.e. 0 [mm/s]). As seen from Figure 5.8, the gain-scheduled DADSC settles nicely when compared to the unscheduled one.

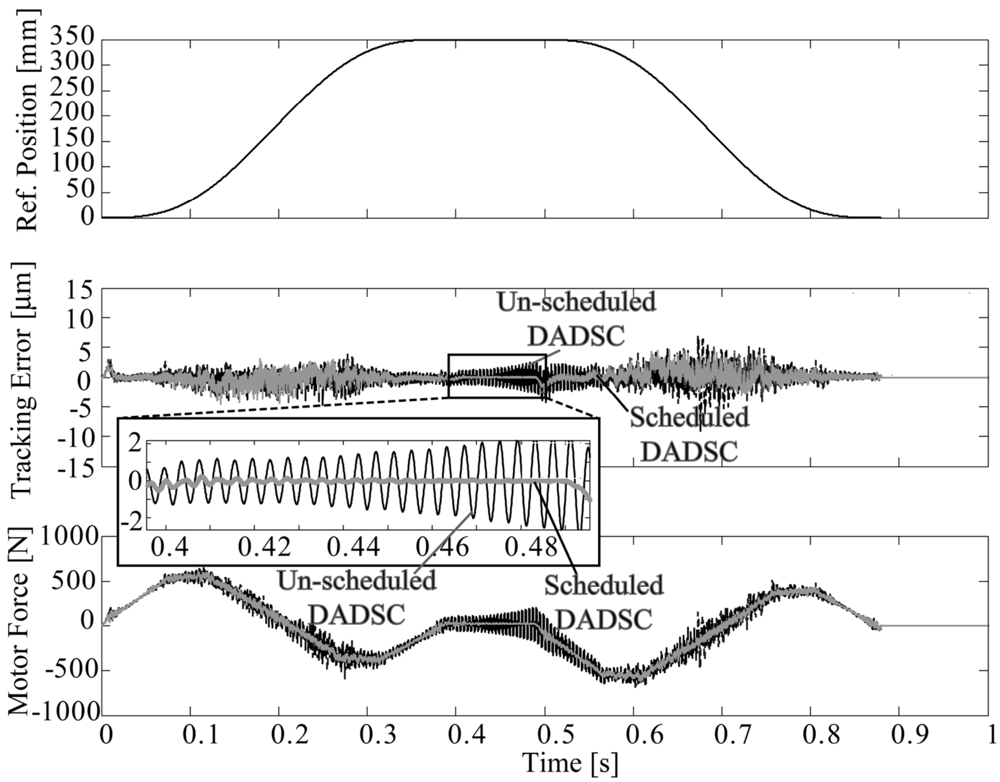


**Figure 5.8: Reference Command, Tracking Error and Motor Force of DADSC with and without Gain Scheduling**

### 5.4.2 Disturbance Rejection Tests

The same 110 [Hz] controller resonance dynamics that is seen in the tracking transfer function also shows up in the disturbance transfer function, as shown in the disturbance Bode plot of the controllers (Figure 5.9). However, in agreement with the theoretical findings of

Section 5.2.4, the DADSC shows the best performance in terms of disturbance suppression (Figure 5.9). The peak magnitude of the disturbance Bode plot is 0.18 [μm/N] for the CC, 0.14 [μm/N] for the ASMC and 0.1 [μm/N] for the DADSC. In other words, the dynamic stiffness of the linear drive is 5.6 [N/μm], 7.1 [N/μm] and 10 [N/μm], respectively for the CC, ASMC and DADSC. This means that the DADSC has a 140 [%] and 178 [%] improvement in dynamics stiffness over the ASMC and CC, respectively.

The improved disturbance rejection capability of the DADSC is also reflected in the result of the step disturbance test (snap-the-rope test) shown in Figure 5.10. It can be observed that the DADSC has the least peak displacement (9.2 [μm]) of the table due to the applied 200 [N] step disturbance force and also its vibrations die out fastest. The same disturbance force produces a peak table displacement of 10.8 [μm] and 15 [μm], respectively when the CC and ASMC are used to control the linear drive.

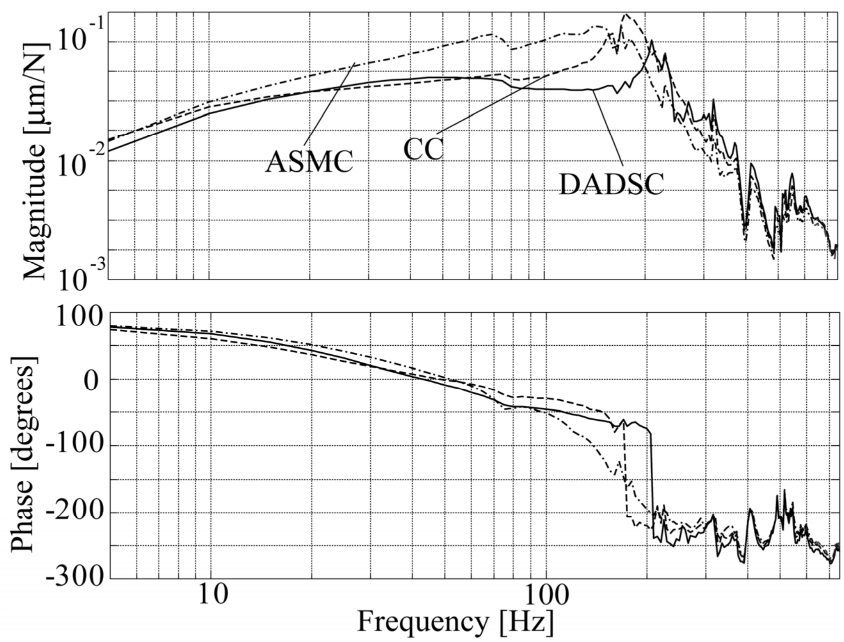


**Figure 5.9: Disturbance Bode Plots ($x(z)/F_d(z)$) for the CC, ASMC and DADSC**

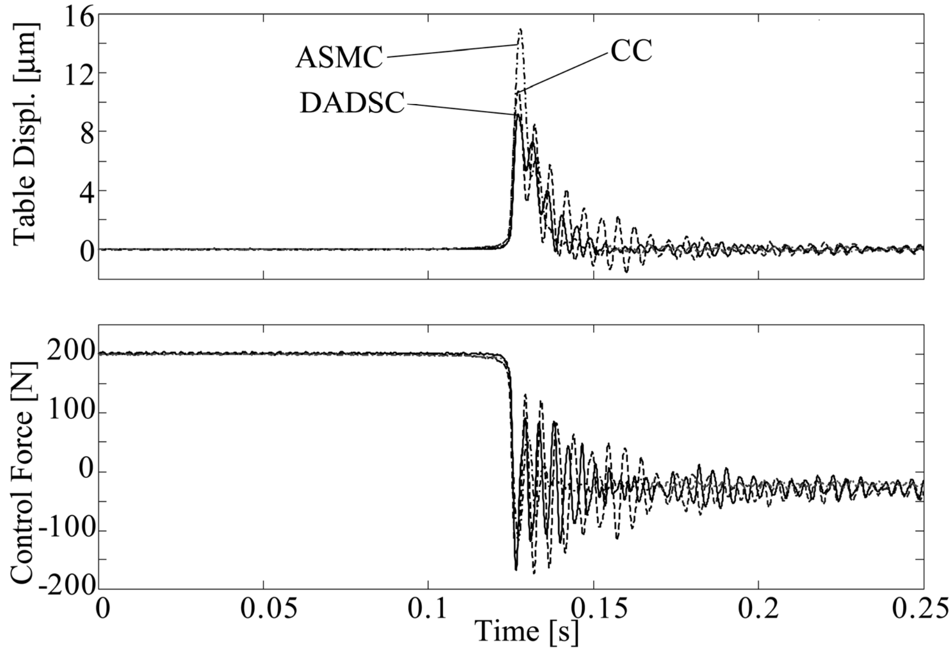


**Figure 5.10: Table Displacement and Control Force for the CC, ASMC and DADSC in Step Disturbance Test (Snap-the-Rope Test)**

### 5.4.3 Disturbance Force Estimation and Suppression of Machine Tool Structural Modes

The advantage of disturbance recovery is demonstrated by applying an external force ($F_d$), via equivalent current, to the direct drive during frequency response measurements. The frequency response of estimated ($\hat{F}_d$) and recovered ($F_{dR}$) disturbance forces against the applied external force ($F_d$) are shown in Figure 5.11 (a) and (b). It is shown that as the disturbance adaptation gain ($g_1$) decreases, the bandwidth of the estimated disturbance force ($\hat{F}_d$) drops while the bandwidth of the recovered disturbance force ($F_{dR}$) remains relatively constant and consistently higher than that of $\hat{F}_d$. A sample comparison of predicted and measured external forces is given in Figure 5.11 (c) and (d). It demonstrates the effectiveness of the proposed controller to predict cutting forces within the bandwidth of the drive.

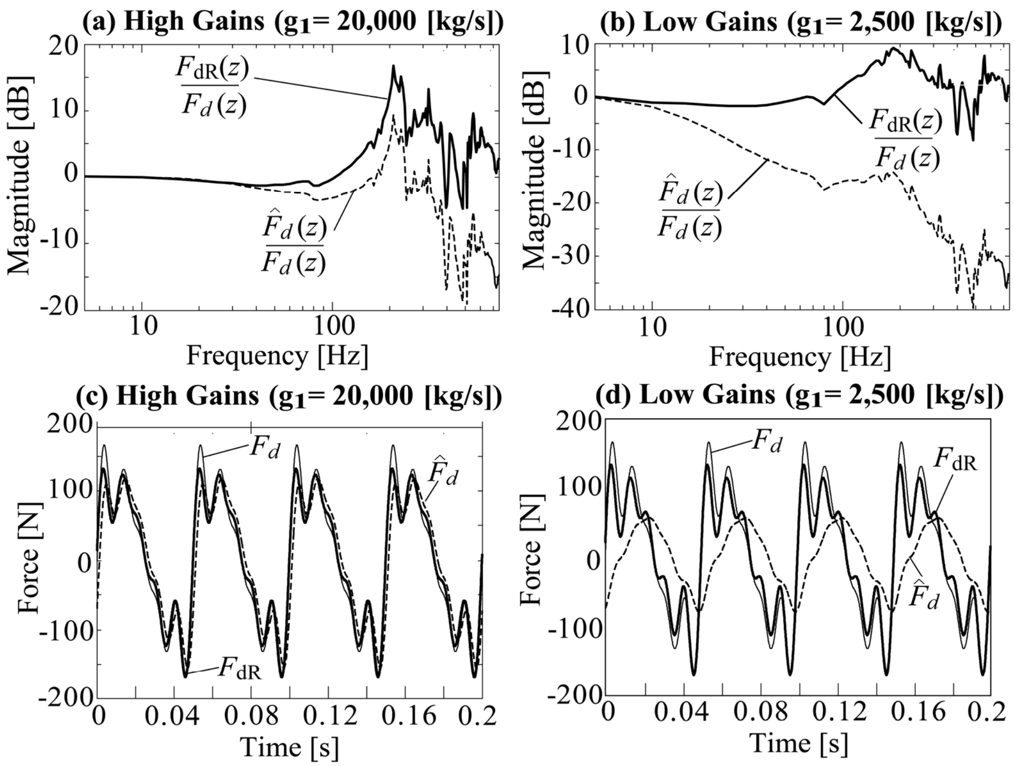


**Figure 5.11: Comparison of DADSC Estimated Force ($\hat{F}_d$) with Recovered Force ($F_{dR}$) for High and Low Adaptation Gains**

The experimental test bed (Figure 5.5) does not have any significant low-frequency structural modes to demonstrate the active damping feature of the proposed controller. Therefore, the use of recovered disturbance forces for compensating machine tool vibrations is demonstrated using a simulated low frequency structural mode ($G_m(s)$) between the tool tip displacement and external force applied to the tool tip by the table. It is given by:

$$G_m(s) = \frac{1}{k_s} \cdot \frac{\omega_n^2}{s^2 + 2\zeta\omega_n s + \omega_n^2} \tag{5.13}$$

where the natural frequency is $\omega_n$ = 308 [rad/s] (49 [Hz]), damping ratio $\zeta$ = 3 [%] and modal stiffness is $k_s$ = 20 [N/µm]. The external forces are exerted on the structure (Eq.(5.13)) and the resulting displacements $x_m(s)$ are used to calculate the relative displacement between tool and workpiece, $x_{tcp}(s)$. Similarly, $G_m(z)$ in Figure 5.4 is obtained by converting Eq.(5.13) to discrete-time domain using a zero-order hold equivalent. It can be seen from the frequency response function between the tool tip vibration and external force that the dynamic stiffness of the machine tool's structural mode is improved significantly (Figure 5.12). The recovered disturbance ($F_{dR}$) is used to effectively damp out the mode at 49 [Hz] by attenuating the dynamic flexibility from 0.70 [μm/N] to 0.22 [μm/N], leading to a 320 [%] increase in the dynamic stiffness of the machine tool, hence its capability to have the same amount of higher chatter-free depth of cut. However, the use of the estimated disturbance force ($\hat{F}_d$) in active damping is hardly effective, which indicates the importance of estimating the cutting and inertial forces accurately. It must be noted here that the time delay between the vibration measurement and control action must be minimum to avoid the large delay. The control frequency was 16,000 [Hz], which is more than 100 times higher than low frequency modes of the machines used in practice.

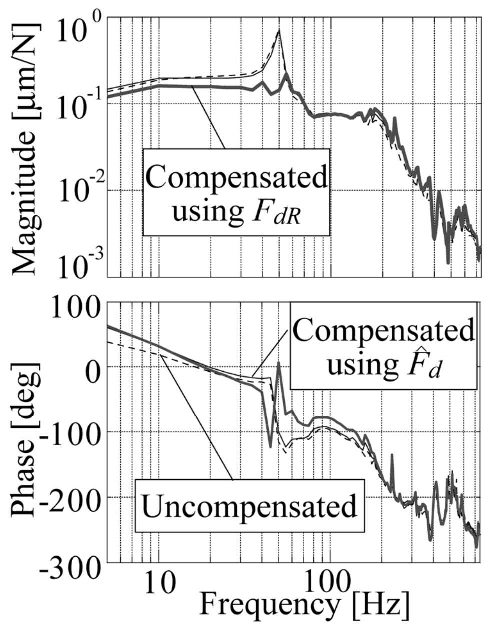


**Figure 5.12: Bode Plot of Transfer Function between Tool and Workpiece ($x_{tcp}(s)/F_d(s)$) – Uncompensated, Compensated using $\hat{F}_d$ and Compensated using $F_{dR}$. $g_1$ = 2,500 [kg/s]**

### 5.5 Summary

This chapter has demonstrated improvement of the dynamic stiffness of direct-driven machine tools using a combination of two techniques. The first technique involves designing a disturbance adaptive sliding mode controller (DADSC) which is shown (theoretically and experimentally) to improve the disturbance rejection capability of the controller compared to similar controllers (i.e. the adaptive sliding mode controller and the cascaded controller). The DADSC achieves this improvement in disturbance rejection, without sacrificing the bandwidth of the controlled drive, by decoupling disturbance estimation from the sliding surface dynamics. True disturbance recovery has also been introduced as a means of achieving better estimation of cutting forces applied to the direct drive. Using the recovered cutting force disturbances, a feed-forward technique is used to predict and cancel out the low-frequency machine tool structural vibrations that are induced during cutting operations. Consequently, the dynamic stiffness between the tool and workpiece is further improved.

# Chapter 6

## Workpiece Mass Estimation in the Presence of Cutting Force Disturbances

### 6.1 Overview

The mass of the table was assumed to be constant while designing controllers for flexible ball screw drives and direct drives in the previous two chapters. However, the mass of the workpiece, which could initially be up to two or three times the mass of the table, changes significantly as material is removed during high speed cutting operations. Consequently, the total mass of the table could vary by more than a hundred percent within a short period of time. The situation is further complicated by the fact that the rate of mass change cannot be easily predicted because it depends on many factors which must be known or measured for each tool, workpiece, machine tool and cutting process combination.

This chapter investigates the effects of the workpiece mass variation on the dynamics of flexible ball screw and direct drives and then proposes a method for estimating the table mass (including the mass of the workpiece) in a way that does not interrupt the cutting process. The estimated table mass can be used to improve the dynamic performance of flexible ball screw and direct drives by updating their table-mass-dependent controller parameters as the cutting operation progresses.

### 6.2 Effects of Table Mass Variation on Dynamics of Feed Drives

#### 6.2.1 Flexible Ball Screw Drives

Generally, rigid ball screw drives are not very sensitive to workpiece inertia variation due to the gear reduction ratio of the ball screw mechanism. Mathematically, if the mass of the table changes by an amount $\Delta m_t$, the corresponding change in equivalent inertia of the drive, $\Delta J_{eq}$, is:

$$\Delta J_{eq} = r_g^2 \Delta m_t \tag{6.1}$$

where $r_g$ is the constant defined in Eq.(3.13). For a typical ball screw drive, $r_g$<<1 so the effect of $\Delta m_t$ on $\Delta J_{eq}$ is greatly reduced.

However, in flexible ball screw drives, the natural frequencies and amplitudes of crucial resonant modes are significantly affected by the variation of table mass. The influence of table mass variation on the axial-torsional-lateral mode (i.e. Mode 1) of the ball screw drive test bed (described in Chapter 3) is shown in Figure 6.1.

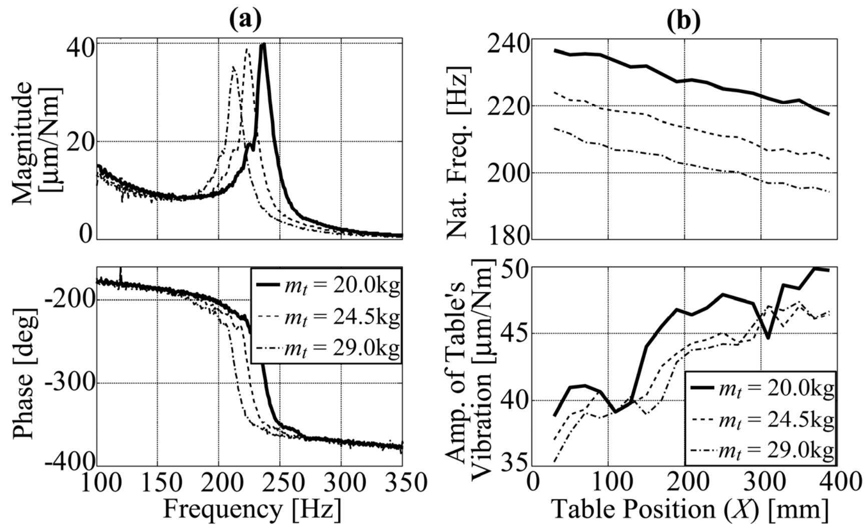


**Figure 6.1: (a) FRF between Torque Applied to Motor and Displacement Measured at Table Positioned at X = 30 [mm] (b) Variation of Mode 1's Natural Frequency and Table Vibration Amplitude as a Function of Table Position for Three Values of Table Mass. Experiments Performed on Ball Screw Drive Test Bed**

Figure 6.1(a) shows that, as the table mass increases, the natural frequency and amplitude of Mode 1 decrease steadily. Figure 6.1(b) indicates that Mode 1's natural frequency decreases with increasing mass at each position of the table within its travel range. Also, it demonstrates that the effect of table mass on the natural frequency of Mode 1 is at least as significant as the effect of table position (*X*). However, the effect of table mass on Mode 1's amplitude is not uniform at every position. This is because the locations of the dips in amplitude (due to the bending of the ball screw – see Chapter 3) also vary as the table's mass changes. Nevertheless, the general trend is that the amplitude of the table's vibration decreases as the mass of the table increases.

The effect table mass variation on the parameters of the drive (identified using the method presented in Section 3.5) is shown in Figure 6.2. As expected the changes in table mass are reflected mainly on $m_{11}$, which is in agreement with theoretical findings [79]. $m_{12}$, $m_{22}$ and $k$ are affected by the table mass change to a much lesser degree. It is observed from experiments that the modal damping ratio ($\zeta$) of Mode 1 does not change significantly due to the increase in table mass. However, the damping coefficients ($c_{11}$, $c_{12}$ and $c_{22}$) are affected indirectly by the influence of $m_{11}$ on the natural frequency ($\omega_n$) and mode shape matrix, **U**. The relationship among the damping coefficients, $\omega_{n,}$ $\zeta$ and **U** is expressed in Eq.(3.49).

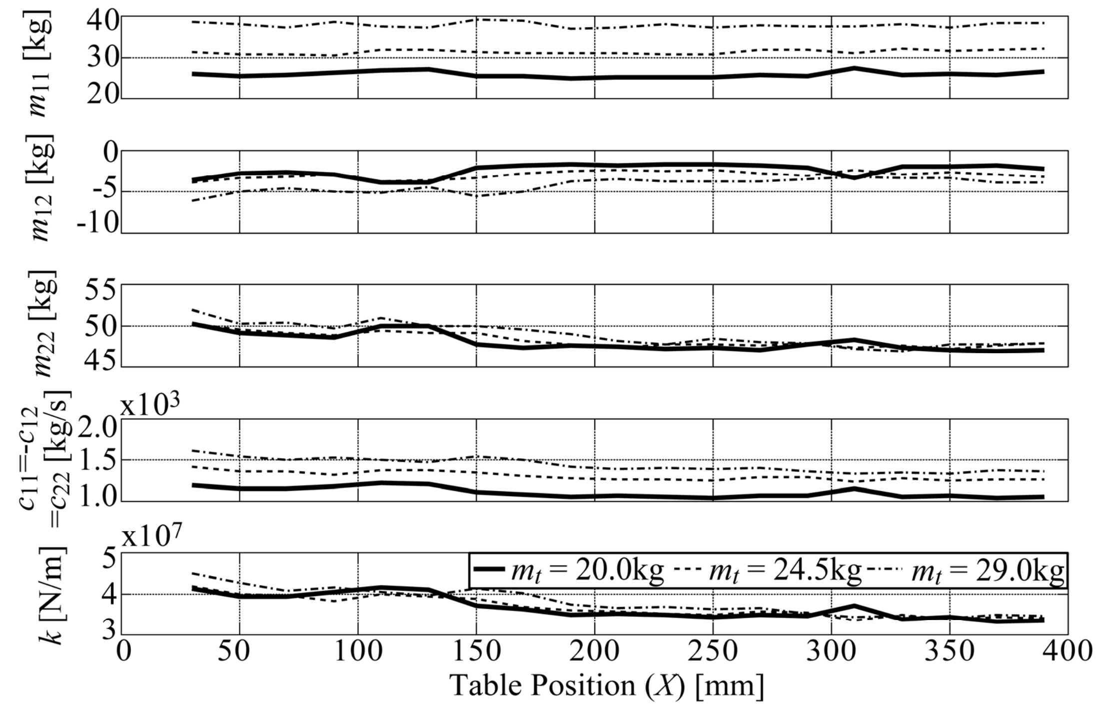


**Figure 6.2: Effects of Table Mass Variation on the Identified Parameters of the Ball Screw Drive Test Bed**

Figure 6.3 shows the closed-loop tracking FRFs for the original and modified MCDADSC+MTEF (introduced in Chapter 4) under the influence of mass variation. Both sets of FRFs are generated with the table located at $X$=30 [mm]. The two controllers are designed using mass, damping and stiffness matrices identified for $X$=30 [mm] and $m_t$ = 20 [kg]

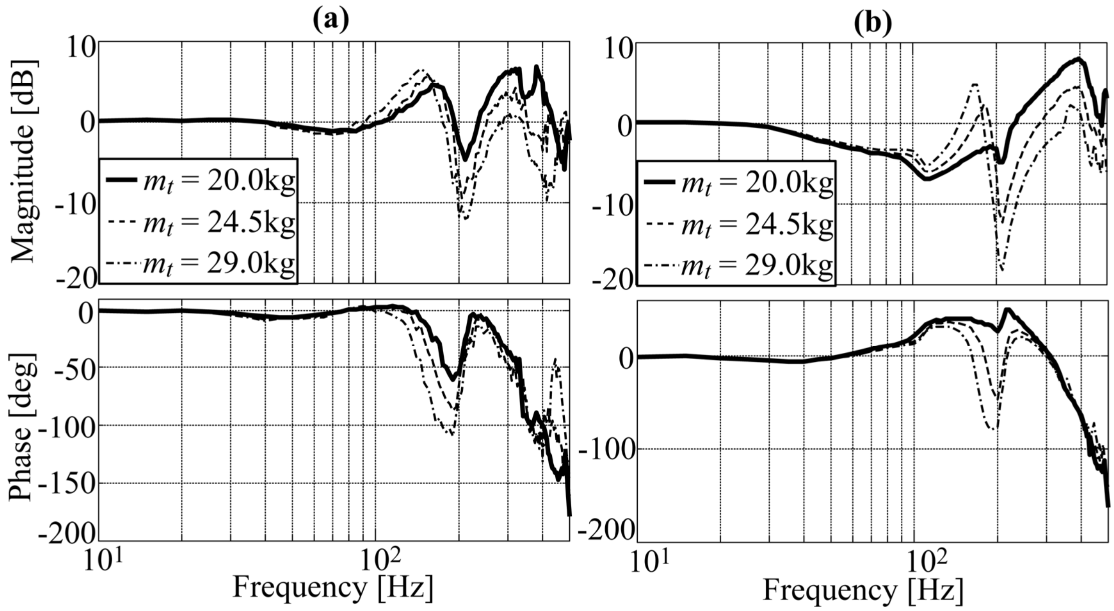


**Figure 6.3: Effect of Mass Variation on Closed-loop Tracking FRF ($x_1/x_{1r}$ or $z_1/z_{1r}$) of Ball Screw Drive Test Bed Controlled using (a) Original MCDADSC+MTEF (b) Modified MCDADSC+MTEF. Controllers Designed for $m_t$ = 20 [kg] and X = 30 [mm]. Table is located at X = 30 [mm]**

Figure 6.3(a) indicates that the peak amplitude of Mode 1 increases from 4.5 [dB] (for $m_t$ = 20 [kg]) to 6.5 [dB] for $m_t$ = 29 [kg]. Consequently, the usable frequency range of the controlled drive (based on the +3 [dB] crossing) reduces from 142 [Hz] to 116 [Hz]. Similarly, for the modified MCDADSC+MTEF, the peak amplitude of Mode 1 increases from –3 [dB] (for $m_t$ = 20 [kg]) to 5 [dB] for $m_t$ = 29 [kg]. The result is that the +3 [dB] crossing drops from 269 [Hz] to 158 [Hz]. However, the dip in amplitude at about 115 [Hz] (see Section 4.5.3 for explanation) reduces from –7 [dB] (for $m_t$ = 20 [kg]) to –5 [dB] for $m_t$ = 29 [kg] due to the increased gain brought about by the extra mass.

### 6.2.2 Direct Drives

Unlike ball screw drives, direct drives do not have any gear reduction ratio; therefore they “feel” the full impact of every change in the mass of the table even when they are rigid. Increase in the mass of the table has the effect of reducing the bandwidth of the drive as depicted in the reference tracking FRF – $x/x_r$ (which is the same as the disturbance recovery FRF – $F_{dR}/F_d$) as shown in Figure 6.4.

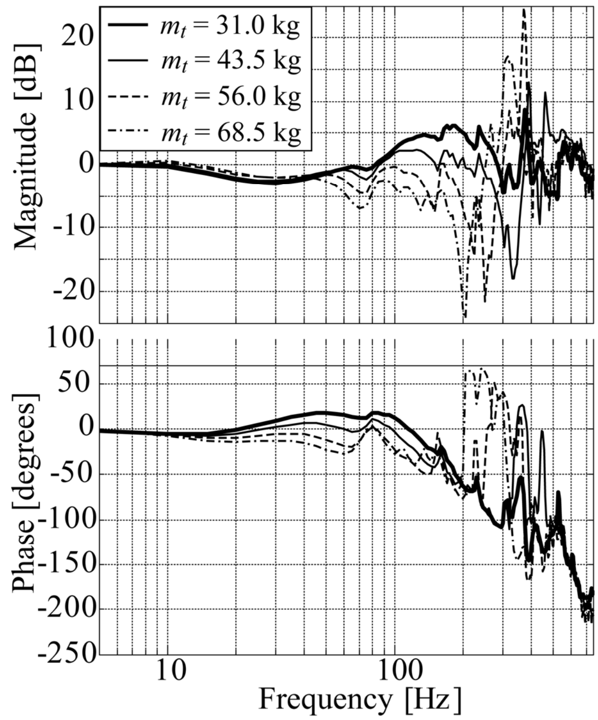


**Figure 6.4: Effect of Mass Variation on Closed-loop Tracking FRF - $x/x_r$ (same as Disturbance Recovery FRF - $F_{dR}/F_d$) of Siemens Direct Drive Test Bed Controlled using a DADSC Designed for $m_t$ = 31 [kg]. $g_1$ = 2,500 [kg/s]**

It is observed from Figure 6.4 that the bandwidth of reference tracking/disturbance recovery FRF of the Siemens direct drive test bed (see Figure Figure 5.5) drops from 104 [Hz] (for $m_t$ = 31 [kg]) to 52 [Hz] for $m_t$ = 68.5 [kg]. This 50 [%] drop in bandwidth is due to the parameter mismatch caused by the variation of table mass.

### 6.3 Estimation of Table Mass during Cutting Operations

The foregoing section has shown that changes in the mass of the table have a significant impact on the closed-loop performance of flexible ball screw and direct drives. This loss of performance due to mass variation can be mitigated by updating the table-mass-dependent parameters of the controllers as a function of the table mass, similar to the table-position-dependent gain scheduling described for ball screw drives in Section 4.4.

However, unlike the position of the table in ball screw drives, accurately measuring the mass of the table during metal cutting operations is not a trivial procedure. This is because embedding weighing scales into machine tool feed drives is costly and the weight readings are likely to be distorted by cutting forces acting in the direction of the weight measurements.

Furthermore, since most weighing scales work on measuring some sort of compliance, they are likely to reduce the dynamic stiffness of the machine tool. Another option is to calculate the removed material from information about the cutter, workpiece and cutting operation. Such calculations are advanced topics of research in the computer-aided design (CAD) field ([7][8][31]). The problem, however, is that the information needed for such calculations are not readily available in the commands sent to the computer numeric control (CNC) unit which is responsible for machine tool feed drive control.

As explained in Chapter 2, various methods have been proposed for observing or estimating the mass of the table using the equations of motion governing the drive [9][12] [24][47]. However, none of these methods are effective when the disturbance forces and workpiece mass are both unknown and time varying at fast rates.

Here, a method for estimating the workpiece mass in the presence of unknown periodic cutting forces is proposed.

### 6.3.1 Theoretical Basis

The workpiece identification method proposed in this chapter is based on two theoretical premises. Firstly, most single-point or multi-point machining operations are periodic at spindle frequency, $f_{sp}$ (or tooth-passing frequency which is an integer multiple of $f_{sp}$) [4]. This means that, as shown in Figure 6.5, their frequency spectrum is dominated by harmonics at integer multiples of $f_{sp}$. It also means that the portions in between these harmonics are zero-force pockets (i.e. the cutting force can be considered equal to zero in the regions between the harmonics). Identifying the mass of the workpiece in these zero-force pockets theoretically ensures that the effects of the unknown cutting forces on the estimated mass are eliminated.

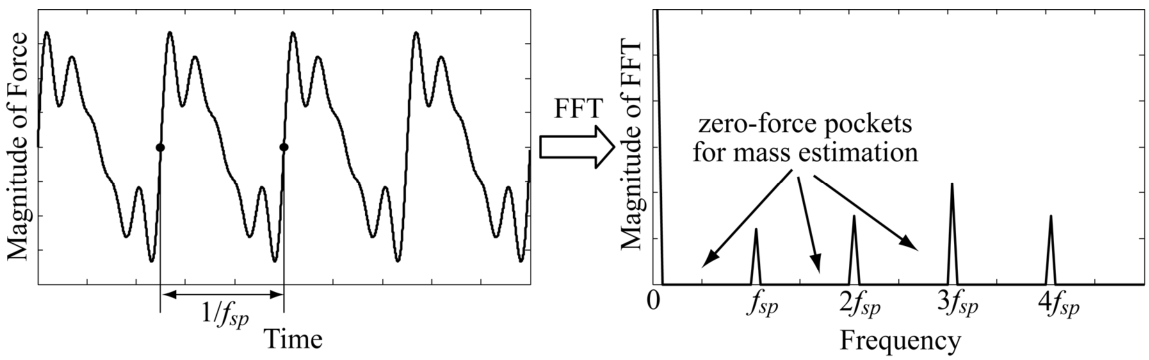


**Figure 6.5: Cutting Forces Periodic at Spindle or Tooth Passing Frequency in both Time and Frequency Domain. The Transformation from Time to Frequency Domain is obtained using the Fast Fourier Transform (FFT)**

Secondly, the low-frequency dynamics of both flexible ball screw drives and direct drives is dominated by the rigid-body dynamics of the drive which can be represented by the transfer function:

$$G_r(\omega) = \frac{v(\omega)}{F_m(\omega)} = \frac{1}{M_r j\omega + B_r} \tag{6.2}$$

where $M_r$ and $B_r$ are the equivalent mass and viscous damping constants of the drive. $G_r(\omega)$ is the transfer function from the force applied to the drive's motor ($F_m$) to the velocity ($v$) of table. If $B_r$ is assumed to be constant then, as $M_r$ increases (due to increases in table mass), the magnitude of $G_r(\omega)$ decreases monotonically at all frequencies (see Figure 6.6).

Based on these two premises, the proposed method estimates the drive's mass ($M_r$) by tracking the changes in the amplitude of $v(\omega)$ per unit force applied to the drive within the zero-force frequency range(s) governed by the rigid body dynamics of the drive (i.e. Eq.(6.2)). A block diagram of the proposed method is shown in Figure 6.7.

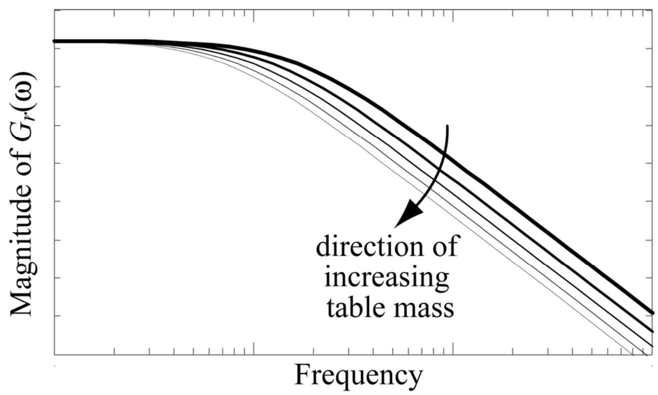


**Figure 6.6: Monotonic Decrease in Magnitude of $G_r(\omega)$ as Mass of Table Increases**

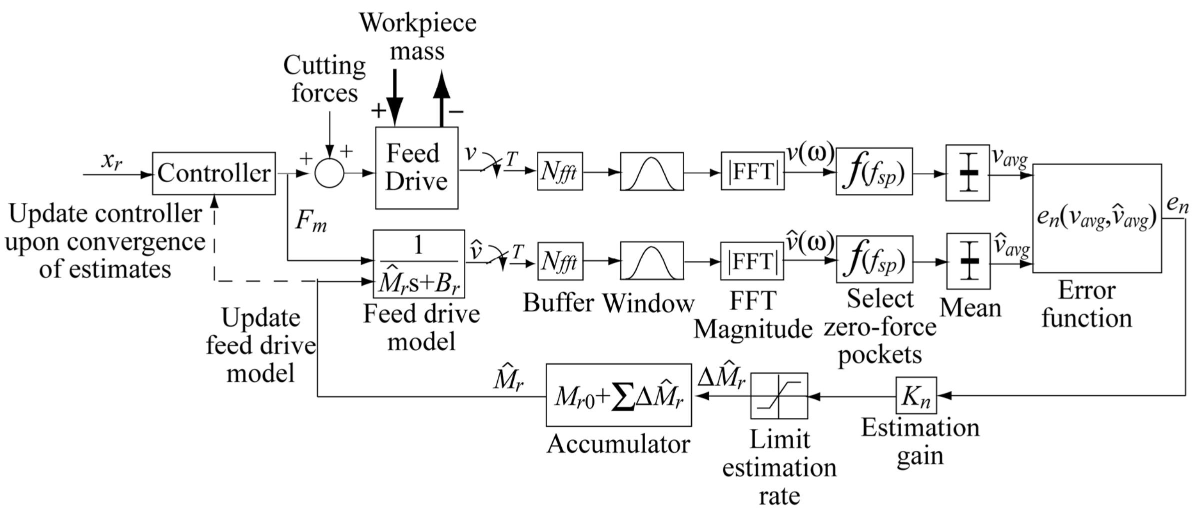


**Figure 6.7: Block Diagram of Frequency Spectrum-Based Mass Estimation**

As shown in the block diagram, the velocity ($v$) of the real feed drive which is subject to motor force commands ($F_m$), unknown cutting forces and workpiece mass variations is measured. An approximation of $v$ (i.e. $\hat{v}$) is also calculated by applying the motor force, $F_m$, measured from the real drive, to the approximated rigid body model of the drive (i.e. Eq.(6.2) with the estimated mass of the drive, $\hat{M}_r$, substituted in place of $M_r$). $v$ contains the influence the workpiece mass variations while $\hat{v}$ does not. In order to calculate the FFTs of $v$ and $\hat{v}$, $N_{fft}$ discrete samples of both velocities are stored in a buffer; where $N_{fft} = 2^n$ and $n$ is an integer. A window function is then applied to the buffered velocities to reduce the effects of spectral leakage when their FFTs are taken. The Blackman window ($W_{BM}$) is preferred for the windowing operation because it results in the least amount of spectral leakage in the frequency domain. Its expression is given by [53]:

$$W_{BM}(k) = 0.42 - 0.5\cos\left(\frac{2\pi(k-1)}{N_{fft}-1}\right) + 0.08\cos\left(\frac{4\pi(k-1)}{N_{fft}-1}\right), \quad 1 \le k \le N_{fft} \tag{6.3}$$

If the feed drive has linear dynamics, the magnitude of the FFT of $v$ (i.e. $v(\omega)$) will be dominated by harmonics at integer multiples of the spindle frequency ($f_{sp}$) due to the influence of the unknown cutting forces. $\hat{v}(\omega)$ may also contain some harmonics of the unknown cutting forces due to the efforts of the controller to cancel them out using $F_m$, but the amplitude of the harmonics in $v(\omega)$ and $\hat{v}(\omega)$ will be different. Furthermore, both $v(\omega)$ and $\hat{v}(\omega)$ will contain frequency contents of the reference velocity command, $\dot{x}_r$. To eliminate the portions of $v(\omega)$ and $\hat{v}(\omega)$ that contain the unknown cutting force harmonics, $f_{sp}$ (which is available to the CNC) is used to select the zero-force pockets from the FFTs of both velocities. The selection blocks also make sure that only the low-frequency range of the FFTs (which agrees with the model of Eq.(6.2)) is selected. In addition, to reduce the effects of sensor noise on the estimation, the selection blocks focus on the frequency regions that contain useful information (i.e. regions where the FFT of the reference velocity is non-zero). If the reference velocity does not have a rich enough frequency spectrum, it can be augmented by introducing a small reference velocity signal within the selected frequency range. Based on Figure 6.7, if the actual mass of the drive ($M_r$) is greater than the estimated mass ($\hat{M}_r$), then the amplitude of $v(\omega)$ will be less than that of $\hat{v}(\omega)$ throughout the selected frequency range. The situation is reversed if $M_r$ is less than $\hat{M}_r$. Consequently, the mean values ($v_{avg}$ and $\hat{v}_{avg}$) of the respective amplitudes of $v(\omega)$ and $\hat{v}(\omega)$ are taken and used to calculate a normalized error ($e_n$) given by:

$$e_n = -\frac{v_{avg} - \hat{v}_{avg}}{\sqrt{0.5\left(v_{avg}^2 + \hat{v}_{avg}^2\right) + \varepsilon}} \tag{6.4}$$

where $\varepsilon$ is a small positive number which ensures that the denominator of Eq.(6.4) does not vanish when the signals are equal to zero. $e_n$ in Eq.(6.4) is defined such that its typical values range between -1 and 1. $e_n$>0 indicates that the mass of the actual drive is greater than that of the model while $e_n$<0 indicates the opposite situation. During each cycle, the value of $e_n$ is scaled by a gain $K_n$ and is used to calculate the incremental mass ($\Delta\hat{M}_r$) which must be added to (or subtracted from) the estimated mass of the model ($\hat{M}_r$) in order to make $e_n$ equal to zero. The rate of change of $\hat{M}_r$ can be controlled by placing a limit on the value of $\Delta\hat{M}_r$ calculated per cycle. When $\hat{M}_r$ is judged to have converged (based on a pre-determined criterion e.g. the value of $e_n$) it can be used to update the table-mass-dependent parameters in the controller so as to improve the performance of the feed drive.

### 6.3.2 Simulation Results

To demonstrate the potential of the mass estimation method presented in the preceding section, a simulation test consisting of high speed cutting of an aluminum alloy is conducted. The feed drive as assumed to be the Siemens direct drive test bed in Chapter 5 and the DADSC, whose parameters are given in Table 5.2, is used to control the drive. The specifics of the cutting operation are summarized in Table 6.1.

Material is removed from the workpiece by milling it in back and forth motions using the finite-jerk feed trajectory of Figure 4.6 with a 350 [mm] stroke (i.e. the length of the workpiece), 400 [mm/s] velocity, 1.5 [g] acceleration and 1,000,000 [mm/s$^3$] jerk. The cutting process is simulated using a milling simulation software [20] and the cutting forces in the direction of motion are obtained as shown in Figure 6.8.

The mass estimation method described in the previous section is implemented in MATLAB Simulink® using a sampling interval of $T$ = 62.5 [µs]. The mass estimation parameters used for the simulation are summarized in Table 6.2.

| Parameter | Value |
|---|---|
| Workpiece Material | Al 7075 |
| Tool Type/Material | 4-Fluted Helical Endmill/Carbide |
| Tool Diameter | 20 [mm] |
| Tool Helix Angle | 30 [deg] |
| Spindle Speed | 20000 [rpm] |
| Feed per tooth | 0.3 [mm/flute] |
| Axial Depth of Cut | 10 [mm] |
| Milling type | Half Immersion Up Milling |
| Initial Mass of Workpiece | 53.2 [kg] |
| Final Mass of Workpiece | 10 [kg] |
| Total Volume of Material Removed | 16,000 [$cm^3$] |
| Metal Removal Rate | 40 [$cm^3/s$] |

**Table 6.1: Specifics of Cutting Operation Used in Simulation Test**

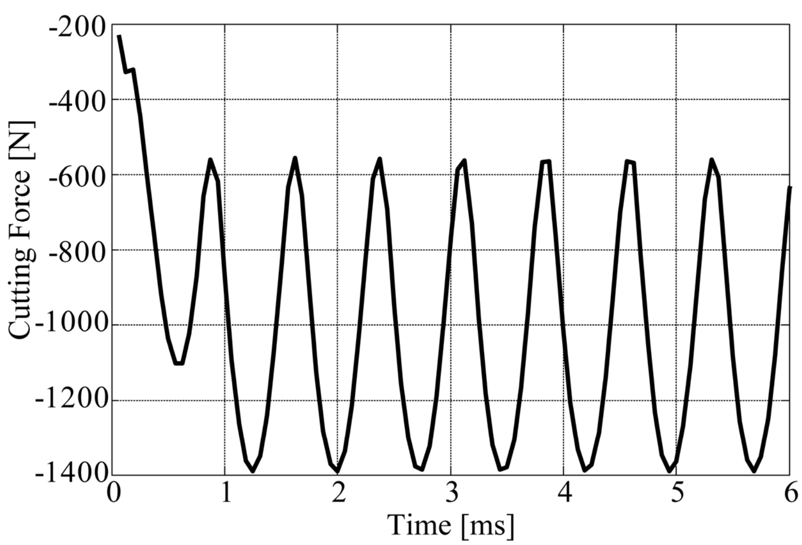


**Figure 6.8: Cutting Forces Applied To Drive in Direction of Motion**

| Parameter | Value |
|---|---|
| $N_{fft}$ | 131,072 (i.e. 8.19 [s]) |
| $f_{sp}$ | 333 [Hz] |
| $\varepsilon$ | $1x10^{-6}$ |
| Estimation Rate Limits | ±5 [kg] |
| $M_{r0}$ | 31 [kg] |

**Table 6.2: Parameters used for Mass Estimation in Simulation Test**

Figure 6.9 shows the result of the mass estimation. When the workpiece is loaded onto the table, the total drive mass (i.e. table+workpiece) is 84.2 [kg]. As the cutting operation progresses, this drive mass is reduced at an average rate of 0.108 [kg/s]. After 400 [s], the final mass of the table and workpiece (i.e. 41 [kg]) is reached. The mass estimator is initialized at 31 [kg] (i.e. the mass of the table without any workpiece). The estimated mass increases gradually until it reaches the actual mass of the table and then it continues tracking the actual mass as it gradually decreases. There is a small steady-state error of about 3 [kg] in tracking the actual mass. This error is attributed to errors in computing the FFT (e.g. spectral leakage) and also to the minimal amount of white noise introduced into the “measured” velocity signal. The estimated mass is used to update the controller only when the normalized error, $e_n$, has dropped below a pre-specified value. In this case, $e_n<0.1$ is used as the convergence criterion. This convergence criterion is satisfied at $t = 106$ [s].

To demonstrate the benefits of updating the controller with mass estimates, in Figure 6.10, the reference tracking Bode plot of the controlled drive is shown for the three points marked in Figure 6.9 (i.e. $t = 150$ [s], $t = 250$ [s] and $t = 350$ [s]). One set of plots represents the case where there is no mass update applied to the controllers (i.e. the mass of 31 [kg] is kept constant throughout the simulation). In the second set of plots, the controller is updated using the estimated mass. The Bode plots show that when mass updates are applied to the controller, the tracking bandwidth is consistently high and does not change much as the actual table mass changes. Conversely, when mass updates are not applied to the controller, the bandwidth of the drive deteriorates with increasing table mass, as formerly seen in Figure 6.4.

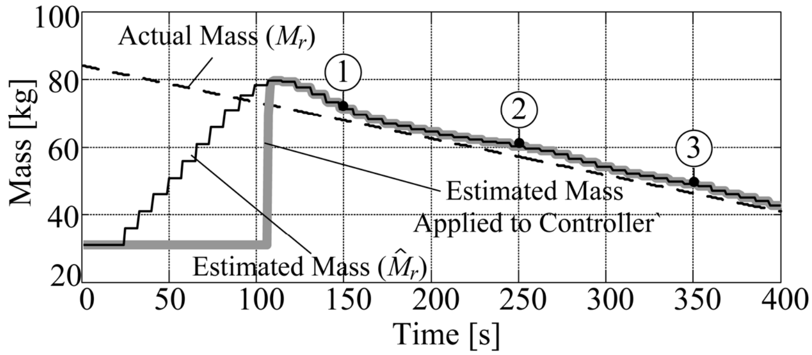


**Figure 6.9: Actual Mass, Estimated Mass and Estimated Mass Applied to the Controller using Proposed Mass Estimation Method**

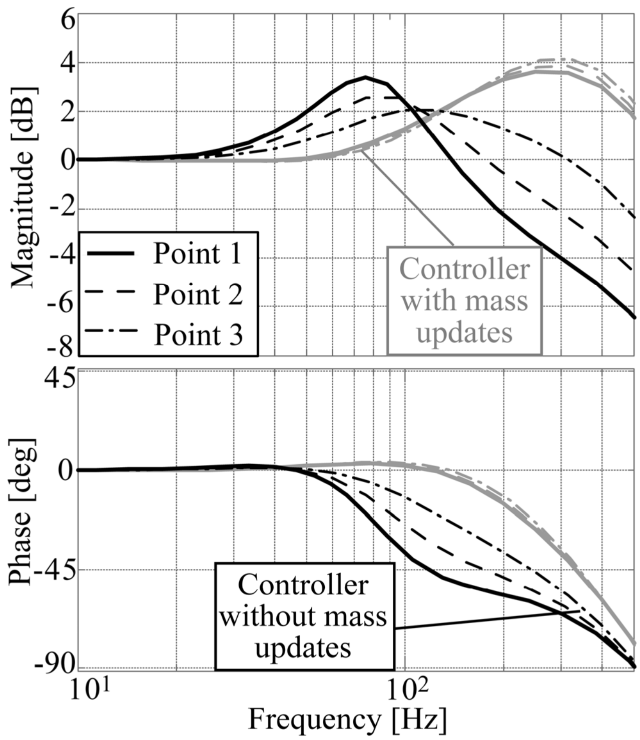


**Figure 6.10: Reference Tracking Bode Plots ($x/x_r$) for Controller without Mass Updates and Controller with Mass Updates at the Three Points Marked on Figure 6.9**

### 6.4 Summary

In this chapter, the effects of workpiece mass change on the dynamics of flexible ball screw and direct drives has been studied. It has been shown using experiments that the dynamic performance of both types of feed drives deteriorates as a result of changes in the mass of the workpiece mounted on to the table. A method for accurately estimating the changes in workpiece mass during metal cutting operations has been proposed. The proposed method assumes that the cutting process is periodic at spindle frequency and that the low-frequency characteristics of the drive is governed by rigid-body dynamics. This allows the mass of the workpiece to be estimated accurately in frequency domain even in the presence of unknown cutting force disturbances. The potentials of the mass estimation method put forward in this chapter have been demonstrated using a simulation test.

# Chapter 7

## Conclusions

### 7.1 Conclusions

Modeling, parameter identification, high-bandwidth control and online parameter estimation techniques addressing key problems encountered in the utilization of ball screw and direct drives in high speed machine tools are proposed in this thesis.

Analytical modeling using finite element methods is carried out to gain a deeper understanding of the structural dynamics behavior of high speed ball screw drives. The information obtained from the finite element model, together with the results of experimental tests on a single-axis ball screw drive test bed, is used to pinpoint the most critical vibration mode that limits high bandwidth control of ball screw drives. The parameters of the drive are accurately identified and then used to design mode-compensating controllers which effectively suppress the critical vibration mode of ball screw drives thereby achieving high-bandwidth control.

For linear motor direct drives, a rigid body dynamics-based sliding mode controller is designed to achieve high dynamic stiffness without sacrificing the tracking performance of the drive. The dynamic stiffness of direct drives is further improved by actively canceling out low-frequency machine tool vibrations based on a high bandwidth disturbance force estimation method.

Finally, for both ball screw and direct drives, online estimation of the changing mass of the workpiece during machining operations with periodic cutting forces is presented.

The contributions of this thesis are summarized as follows:

- A new stiffness matrix, based on rigid ball screw assumptions, is derived for connecting the distributed finite element representation of the screw to a lumped-mass representation of the nut in hybrid models of ball screw drives. This new screw-nut interface stiffness matrix is shown analytically and experimentally to predict the coupling between axial, torsional and lateral dynamics in ball screw drives equipped with short nuts. The effect of the dynamic coupling on the positioning of the table is also demonstrated with experimental proof.

- A screw-nut interface model which considers the deformations of the ball screw within the nut using the Timoshenko beam shape function matrix is developed for modeling ball screw drives with long nuts. A simulation study is used to demonstrate the potential merits of the shape function-based screw-nut interface model over the rigid ball screw-based model for ball screws with long nuts.

- A simple and accurate least squares-based parameter identification technique is introduced for identifying the mass, damping and stiffness matrices of flexible ball screw drives based on measured frequency response function data. Its effectiveness is verified experimentally.

- Mode-compensating disturbance adaptive discrete-time sliding mode controllers combined with minimum tracking error filters are designed for active suppression of structural dynamics and high-bandwidth control of flexible ball screw drives. A method for designing the plant-inversion-based minimum tracking error filters even when there are non-minimum phase zeros in the identified open-loop dynamics of the drive is proposed. The parameters of the designed controller are scheduled in an ad hoc fashion to achieve minimum tracking error control in the presence of table position-dependent variations in the dynamics of the drive. The effectiveness of the control laws is demonstrated numerically and experimentally.

- A rigid-body dynamics-based disturbance adaptive sliding mode controller is designed for linear motor direct drives. This controller is shown, theoretically and experimentally, to improve the dynamic stiffness of direct drives compared to the cascaded controller and the adaptive sliding mode controller, without any loss in reference tracking performance or increase in controller complexity. Disturbance force recovery is also introduced as a more accurate way of estimating the cutting forces applied to the drive compared to the force estimates obtained directly from the controller. The recovered disturbance forces are used to actively cancel out low-frequency vibrations of a simulated machine tool thereby further improving the dynamic stiffness of direct-driven machines.

- A frequency spectrum-based method for online estimation of the changing mass of the workpiece during machining operations which are periodic at spindle frequency is put forward. The technique exploits the periodicity of the cutting forces and low-frequency properties of both ball screw and direct drives to estimate the mass of the workpiece without interrupting the cutting operation. The potentials of this technique are demonstrated in simulation tests.

The major contributions of this thesis have been published in journal ([6][57][58]) and conference ([55][56]) articles.

## 7.2 Future Research Directions

The potential merits of the shape function-based screw-nut interface model presented in this thesis for modeling ball screw drives with long nuts has been demonstrated only in simulation tests. It will be useful to conduct experiments on a long-nut ball screw to ascertain the validity and significance of the advantages of the shape function-based model over the rigid ball screw model observed from simulation results.

In a similar vein, the practicability of the online mass estimation technique and the active vibration cancelation of low-frequency modes of direct-driven machine tools presented in this thesis have to be demonstrated experimentally under real cutting conditions. A linear drive set-up, equipped with a high speed spindle, is needed for this purpose.

The ad hoc gain scheduling method presented in Chapter Four, even though effective, did not have theoretically guaranteed stability conditions. It will be useful to explore other gain scheduling techniques which are effective and have theoretical stability proofs. Moreover, it will be interesting to extend the gain scheduling (based on only table position) performed in this thesis to one which also incorporates the effects of workpiece mass variation in ball screw drives. This will require generating a two-dimensional map for each element of the drive's mass, damping and stiffness matrices as a function of table position and workpiece (table) mass. The map can then be used to update the drive parameters based on the measured table position and the estimated (or measured) mass of the table.

Another topic of research which emanates from this thesis is the design of a high-bandwidth force sensor that can be embedded between the table and nut in ball screw drives.

Such a sensor will provide accurate force estimates that can be utilized to achieve better disturbance rejection using the minimum tracking error filters designed in this thesis.

Parallel kinematic machine tools have generated a lot of interest lately because they have the potential to be faster, more flexible and more accurate than regular Cartesian machine tools. However, quite unlike Cartesian machine tools, they exhibit large rotations; therefore their kinematics is non-linear and configuration-dependent. They are actuated using ball screws and/or direct drives and so they present new challenges to the modeling and control topics tackled in this thesis.

# Bibliography


[1] Allotta, B., Angioli, F., Rinchi, M., 2001, "Constraints Identification for Vibration Control of Time-Varying Boundary Conditions Systems," *Proceedings of the 2001 IEEE/ASME International Conference on Advanced Intelligent Mechatronics*, pp.606-611.

[2] Alter, D.M., Tsao, T-C., 1994, "Dynamic Stiffness Enhancement of Direct Linear Motor Feed Drives for Machining," *Proceedings of the American Control Conference*, Baltimore, MD, pp.3303-3307.

[3] Alter, D.M., Tsao, T.-C., 1996, "Control of Linear Motors for Machine Tool Feed Drives: Design and Implementation of H∞ Optimal Feedback Control," *ASME Journal of Dynamic Systems, Measurement and Control*, Vol.118, pp.649-656.

[4] Altintas, Y., 2000, *Manufacturing Automation*, Cambridge University Press, Cambridge, UK.

[5] Altintas, Y., Erkorkmaz, K., Zhu, W.-H., 2000, "Sliding Mode Controller Design for High Speed Feed Drives," *Annals of CIRP*, Vol.49, No.1, pp.265-270.

[6] Altintas, Y., Okwudire, C.E., 2009, "Dynamic Stiffness Enhancement of Direct-Driven Machine Tools using Sliding Mode Control with True Disturbance Recovery," *Annals of the CIRP*, Vol.58, pp.335-338.

[7] Aras, E., Yip-Hoi, D., 2008, "Geometric Modeling of Cutter/Workpiece Engagements in Three-Axis Milling Using Polyhedral Representations," *ASME Journal of Computing and Information Science in Engineering*, Vol.8, No.3, pp.031007-1 to 031007-13.

[8] Aras, E., 2009, "Generating Cutter Swept Envelopes in Five-Axis Milling by Two-Parameter Families of spheres," *Computer-Aided Design*, Vol.41, No.2, pp.95-105.

[9] Awaya, I., Kato, Y., Miyaka, I., Masami, I., 1992, "New Motion Control with Inertia Identification Function Using Disturbance Observer," *IEEE: Proceedings of International Conference on Power Electronics and Motion Control*, pp.77-81.

[10] Berkermer, J., 2003, *Ph.D. Thesis: Gekoppelte Simulation von Maschinen-dynamik und Antriebsregelung unter Verwendung linearer Finite Elemente Modelle*, Universität Stuttgart, Institut für Statik und Dynamik der Luft-Und Raumfahrtkonstruktionen, Stuttgart.

[11] Brecher, C., Schulz, A., Weck, M., 2005, "Electrohydraulic Active Damping System," *Annals of the CIRP*, Vol.54, No.1, pp.389-392.

[12] Butler, H., Honderd, G., van Amerongen, J., 1989, "Model Reference Adaptive Control of a Direct-Drive DC Motor," *IEEE Control Systems Magazine*, pp.80-84.

[13] Castaneda-Castillo, E., Okazaki, Y., 1998, "Load Variation Compensation in Real-Time for Motion Accuracy of Machine Tools," *IEEE 5th International Workshop on Advanced Motion Control*, Coimbra, Portugal, pp.305-309.

[14] Chen, J.-S., Huang, Y.-K., Cheng, C.-C., 2004, "Mechanical Model and Contouring Analysis of High-Speed Ball-Screw Drive Systems with Compliance Effect," *International Journal of Advanced Manufacturing Technology*, Vol.24, pp.241-250.

[15] Chen, Y., Tlusty, J., 1995, "Effect of Low-Friction Guideways and Lead-Screw Flexibility on Dynamics of High-Speed Machines", *Annals of the CIRP*, Vol. 44, No. 1, pp. 353-356.

[16] Choi, C., Tsao, T.-C., 2005, "Control of Linear Motor Machine Tool Feed Drives for End Milling: Robust MIMO Approach," *Mechatronics*, Vol.15, pp.1207-1224.

[17] Chung, B., Smith, S., Tlusty, J., 1997, "Active Damping of Structural Modes in High-Speed Machine Tools," *Journal of Vibration and Control*, Vol.3, pp.279-295.

[18] Chung, S.K., Lee, J.H., Ko, J.S., Youn, M.J., 1995 "Robust Speed Control of Brushless Direct-drive Motor using Integral Variable Structure Control," *IEEE Proceedings on Electrical Power Applications*, Vol.142, No.6, pp.361-369.

[19] Cobb, W.T., 1989, *M.Sc. Thesis: Design of Dampers for Boring Bars and Spindle Extensions*, University of Florida, Department of Mechanical Engineering, Florida.

[20] *Cut Pro® - Milling and Virtual CNC Modules*. Manufacturing Automation Laboratory, University of British Columbia.

[21] Cuttino, J.F., Dow, T.A., 1997, "Contact between Elastic Bodies with an Elliptic Contact Interface in Torsion," *ASME Journal of Applied Mechanics*, Vol.64, pp.144-148.

[22] Cuttino, J.F., Dow, T.A., Knight, B.F., 1997, "Analytical and Experimental Identification of Nonlinearities in a Single-Nut Preloaded Ballscrew," *ASME Journal of Mechanical Design*, Vol.119, pp.15-19.

[23] Denkena, B., Tonshoff, H.K., Li, X., 2004, "Analysis and Control/Monitoring of the Direct Linear Drive in End Milling," *International Journal of Production Research*, Vol.42, No.24, pp.5149-5166.

[24] Dessaint, L.A., Hebert, B.J., Le-Huy, H., Cavouti, G., 1990, "A DSP-Based Adaptive Controller for a Smooth Positioning System," *IEEE Transactions on Industrial Electronics*, Vol.37, No.5, pp.372-377.

[25] Dumur, D., Boucher, P., Ramond, G., 2000, "Direct Adaptive Generalized Predictive Control. Application to Motor Drives with Flexible Modes," *Annals of the CIRP*, Vol.49, No.1, pp.271-274.

[26] Egami, T., Tsuchiya, T., 1995, "Disturbance Suppression Control with Preview Action of Linear DC Brushless Motor," *IEEE Transactions on Industrial Electronics*, Vol.42, No.5, pp.494-500.

[27] Erkorkmaz, K., Altintas, Y., 2001, "High Speed CNC System Design: Part II – Modeling and Identification of Feed Drives," *International Journal of Machine Tools and Manufacture*, Vol.41, No.10, pp.1487-1509.

[28] Erkorkmaz, K., 2003, *Ph.D. Thesis: Optimal Trajectory Generation and Precision Tracking Control for Multi-Axis Machines*, University of British Columbia, Department of Mechanical Engineering, Vancouver.

[29] Erkorkmaz, K., Kamalzadeh, A., 2006, "High Bandwidth Control of Ball Screw Drives," *Annals of the CIRP*, Vol.55, No.1, pp.393-398.

[30] Ewin, D.J., 1999, *Modal Testing – Theory, Practice and Application (2nd Ed.)*, Research Studies Press Ltd., Hertfordshire, UK.

[31] Ferry, W., Yip-Hoi, D., 2008, "Cutter-Workpiece Engagement Calculations By Parallel Slicing For Five-Axis Flank Milling of Jet Engine Impellers," *ASME Journal of Manufacturing Science and Engineering*, Vol.130, pp.051011-1 to 051011-12.

[32] Freudenberg, J.S., Looze, D.P., 1985, "Right Half Plane Poles and Zeros and Design Tradeoffs in Feedback Systems," *IEEE Transactions on Automatic Control*, Vol.30, No.6, pp.555-565.

[33] Gross, E., Tomizuka, M., Messner, W., 1994, "Cancellation of Discrete Time Unstable Zeros by Feedforward Control," *ASME Journal of Dynamic Systems, Measurement and Control*, Vol.116, pp.33-38.

[34] Haack, B., Tomizuka, M., 1991, "The Effects of Adding Zeroes to Feedforward Controllers," *ASME Journal of Dynamic Systems, Measurement and Control*, Vol.113, pp. 6-10.

[35] Jamaludin, Z., Brussel, H.V., Swevers, J., 2007, "Classical Cascade and Sliding Mode Control Tracking Performances for a XY Feed Table of a High-Speed Machine Tool," *International Journal of Precision Technology*, Vol.1, No.1, pp.65-74.

[36] Jamaludin, Z., Van Brussel, H., Pipeleers, G., Swevers, J., 2008, "Accurate Motion Control of XY High-Speed Linear Drives using Friction Model Feed-Forward and Cutting Forces Estimation," *Annals of the CIRP*, Vol.57, No.1, pp.403-406.

[37] Jones, S.D, Ulsoy, A.G, 1999, "An Approach to Control Input Shaping with Application to Coordinate Measuring Machines," *ASME Journal of Dynamic Systems, Measurement and Control*, Vol.121, No.2, pp.242-247.

[38] Hirvonen, M., Pyrhonen, O., Handroos, H., 2006, "Adaptive Nonlinear Velocity Controller for a Flexible Mechanism of a Linear Motor," *Mechatronics*, Vol. 16, pp.279-290.

[39] Holroyd, G., Pislaru, C., Ford, D.G., 2003, "Modelling the Dynamic Behaviour of a Ball-Screw System Taking into Account the Changing Position of the Ball-Screw Nut," *Proceedings of the 6$^{th}$ International Conference LAMDAMAP*, Huddersfield, UK, pp.337-348.

[40] Kamalzadeh, A., Erkorkmaz, K., 2007 "Compensation of Axial Vibrations in Ballscrew Drives," *Annals of the CIRP*, Vol.56, No.1, pp.373-378.

[41] Kamalzadeh, A., Erkorkmaz, K., 2007, "Compensation of Lead Errors and Elastic Deformations in Ball Screw Drives," *Proceedings of CIRP/NIST International Conference on Smart Machining Systems (ICSMS'07)*, March 13-15, Gaithersburg, MD.

[42] Kamalzadeh, A., Erkorkmaz, K., 2007, "Accurate Tracking Controller Design for High-Speed Drives," *International Journal of Machine Tools and Manufacture*, Vol.47, No.9, pp.1393-1400.

[43] Kamalzadeh, A., 2008, Ph.D. Thesis: Precision Control of High Speed Ball Screw Drives, University of Waterloo, Department of Mechanical Engineering, Waterloo.

[44] Kim, M.-S., Chung, S.-C., 2006, "Integrated Design Methodology of Ball-Screw Driven Servomechanisms with Discrete Controllers. Part I: Modelling and Performance Analysis," *Mechatronics*, Vol.16, pp.491-502.

[45] Komada, S., Ishida, M., Ohnishi, K., 1991, "Disturbance Observer-Based Motion Control of Direct Drive Motors," *IEEE Transactions on Energy Conversion*, Vol.6, No.3, pp.553-559.

[46] Lee, K., Ibaraki, S., Matsubara, A., Kakino, Y., Suzuki, Y., Arai, S., Braasch, J., 2002, "A Servo Parameter Tuning Method for High-Speed NC Machine Tools based on Contouring Error Measurement," *Laser Metrology and Machine Performance VI*, WIT Press, Southampton, UK.

[47] Lee, K.B., Yoo, J.Y., Song, J.H., Choy, I., 2004, "Improvement of Low Speed Operation of Electric Machine with an Inertia Identification using ROELO," *IEE Proceedings on Electric Power Applications*, Vol.151, No.1, pp.116-120.

[48] Lim, H., Seo, J., Choi, C., 2000, "Position Control of XY Table in CNC Machining Center with Non-Rigid Ballscrew," *Proceedings of the 2000 American Control Conference*, Chicago, pp.1542-1546.

[49] Lim, H., Seo, J.W., Choi, C.H., 2001, "Torsional Displacement Compensation in Position Control for Machining Centers," *Control Engineering Practice*, Vol.9, No.1, pp.79-87.

[50] Lin, M.C., Ravani, B., Velinsky, S.A., 1994, "Kinematics of the Ball Screw Mechanism," *ASME Journal of Mechanical Design*, Vol.116, pp.849-855.

[51] Liu, T.-H., Lee, Y.-C., Chang, Y.-H., 2004, "Adaptive Controller Design for a Linear Motor Control System," *IEEE Transactions on Aerospace and Electronic Systems*, Vol.40, No.2, pp.601-615.

[52] Maeda, O., 2003, *M.A.Sc. Thesis: Expert Spindle Design System*, University of British Columbia, Department of Mechanical Engineering, Vancouver.

[53] Oppenheim, A.V., Schafer, R.W., 1999, *Discrete-Time Signal Processing*, Upper Saddle River, NJ: Prentice-Hall, pp.468-471.

[54] Okwudire, C.E., 2005, *M.A.Sc. Thesis: Finite Element Modeling of Ball screw Feed Drive Systems for Control Purposes*, University of British Columbia, Department of Mechanical Engineering, Vancouver.

[55] Okwudire, C.E., Altintas, Y., 2007, "Modeling of the Screw-Nut Interface of Ball screw Drives," *ASME International Mechanical Engineering Congress and Exposition*, Seattle, Washington, USA. IMECE 2007-42593.

[56] Okwudire, C.E., Altintas, Y., 2008, "Effective Control of Direct Drives using a Disturbance Adaptive Discrete-Time Sliding Mode Controller," *3rd CIRP High Performance Cutting Conference*, June 12-13, 2008, Dublin, Ireland.

[57] Okwudire, C.E., Altintas, Y., 2009, "Hybrid Modeling of Ball Screw Drives with Coupled Axial, Torsional and Lateral Dynamics," *ASME Journal of Mechanical Design*, Vol.131, pp.071002-1 to 071002-9.

[58] Okwudire, C.E., Altintas, Y., 2009, "Minimum-Tracking Error Control of Flexible Ballscrew Drives using a Discrete-Time Sliding Mode Controller," *ASME Journal of Dynamic Systems, Measurement and Control*, (in press).

[59] Pislaru, C., Ford, D.G., Holroyd, G., 2004, "Hybrid Modelling and Simulation of a Computer Numerical Control Machine Tool Feed Drive," *Proceedings of the Institution of Mechanical Engineers*, Part I: Journal of Systems and Control Engineering, Vol.218, pp.111-120.

[60] Poignet, P., Gautier, M., Khalil, W., 1999, "Modeling, Control and Simulation of High Speed Machine Tool Axis," *Proceedings of IEEE International Conference on Advanced Intelligent Mechatronics*, Atlanta, September 19-23, pp.617-622.

[61] Pritschow, G., 1998, "A Comparison of Linear and Conventional Electromechanical Drives," *Annals of the CIRP*, Vol.47, No.2, pp.541-547.

[62] Pritschow, G., Philipp, W., 1990, "Direct Drives for High-Dynamic Machine Tool Axes," *Annals of the CIRP*, Vol.39, No.1, pp.413-416.

[63] Pritschow G., Philipp, W., 1992, "Research on the Efficiency of Feedforward Controllers in M Direct Drives," *Annals of the CIRP*, Vol.41, No.1, pp.411-415.

[64] Przemieniecki, J.S., 1968, *Theory of Matrix Structural Analysis*, McGraw-Hill, New York.

[65] Qian, X., Wang, Y., Ni, M.L., 2005, "Robust Position Control of Linear Brushless DC Motor Drive System Based on μ-Synthesis," *IEEE Proceedings on Electrical Power Applications*, Vol.152, No.2, pp.341-351.

[66] Renton, D., Elbestawi, M.A., 2001, "Motion Control for Linear Motor Feed Drives in Advanced Machine Tools," *International Journal of Machine Tools and Manufacture*, Vol.41, pp.479-507.

[67] Schafers, E., Denk, J., Hamann, J., 2006, "Mechatronic Modeling and Analysis of Machine Tools," *Proceedings of the 2nd International Conference on High Performance Cutting (CIRP-HPC'06)*, June 12-13, Vancouver.

[68] Shieh, N.C., Tung, P.C., 2001, "Robust Position Control of a Transportation Carriage Directly Driven by a Linear Brushless D.C. Motor," *Proceedings of the Institution of Mechanical Engineers*, Vol.215, pp.611-623.

[69] Slotine, J.-J.E., Li, W., 1988, "Adaptive Manipulator Control: A Cast Study," *IEEE Transactions on Automatic Control*, Vol.33, No.11, pp.95-1003.

[70] Smith, A.D., 1999, *Ph.D. Thesis: Wide Bandwidth Control of High-Speed Milling Machine Feed Drives*, University of Florida, Department of Mechanical Engineering, Florida.

[71] Spector, V.A., Flashner, H., 1990, "Modeling and Design Implications of Noncollocated Control in Flexible Systems," *ASME Journal of Dynamic Systems, Measurement and Control*, Vol.112, pp.186-193.

[72] Symens, W., Van Brussel, H., Swevers, J., 2004 "Gain-Scheduling Control of Machine Tools with Varying Structural Dynamics," *Annals of the CIRP*, Vol.53, No.1, pp.321-324.

[73] Tomizuka, M., 1987, "Zero Phase Error Tracking Algorithm for Digital Control," *ASME Journal of Dynamic Systems, Measurement, and Control*, Vol.109, pp.65-68.

[74] Torfs, D., De Schutter, J., Swevers, J., 1992, "Extended Bandwidth Zero Phase Error Tracking Control of Nonminimal Phase Systems," *ASME Journal of Dynamic Systems, Measurement and Control*, Vol.114, pp.347-351.

[75] Utkin, V.I., 1977, "Variable Structure Systems with Sliding Modes," *IEEE Transactions on Automatic Control*, Vol.22, No.2, pp.212-222.

[76] Van Brussel, H., Sas, P., Istvan, N., De Fonseca, P., Van Den Braembussche, P., 2001, "Towards a Mechatronic Compiler," *IEEE/ASME Transactions on Mechatronics*, Vol.6, No.1, pp.90-105.

[77] Van Brussel, H., Van den Braembussche, P., 1998, "Robust Control of Feed Drives with Linear Motors," *Annals of the CIRP*, Vol.47, No.1, pp.325-328.

[78] Van den Braembussche, P., Swevers, J., Van Brussel, H., 2001, "Design and Experimental Validation of Robust Controllers for Machine Tool Drives with Linear Motor," *Mechatronics*, Vol.11, pp.545-561.

[79] Varanasi, K.K., Nayfeh, S.A., 2004, "The Dynamics of Lead-Screw Drives: Low-Order Modeling and Experiments," *ASME Journal of Dynamic Systems, Measurement and Control*, Vol.126, pp.388-396.

[80] Wang, J., Van Brussel, H., Swevers, J., 2003, "Robust Perfect Tracking Control with Discrete Sliding Mode Controller," *ASME Journal of Dynamic Systems, Measurement and Control*, Vol.125, pp.27-32.

[81] Weck, M., Ye, G., 1990, "Sharp Corner Tracking Using the IKF Control Strategy," *Annals of the CIRP*, Vol.39, No.1, pp.437-441.

[82] Wei, C.C., Lin, J.F., 2003, "Kinematic Analysis of the Ball Screw Mechanism Considering Variable Contact Angles and Elastic Deformations," *ASME Journal of Mechanical Design*, Vol.125, pp.717-733.

[83] Won, M., Hedrick, J.K., 2001, "Disturbance Adaptive Discrete-Time Sliding Control with Application to Engine Speed Control," *ASME Journal of Dynamic Systems, Measurement and Control*, Vol.123, pp.1-9.

[84] Whalley, R., Ebrahimi, M., Abdul-Ameer, A.A., 2006, "Machine Tool Axis Dynamics," *Proceedings of IMechE Part C: Journal of Mechanical Engineering Science*, Vol.220, pp.403-419.

[85] Xu, L., Yao, B., 2001, "Adaptive Robust Precision Motion Control of Linear Motors with Negligible Electrical Dynamics: Theory and Experiments," *IEEE/ASME Transactions on Mechatronics*, Vol.6, No.4, pp.444-452.

[86] Yang, T., Lin, C.-S., 2004, "Identifying the Stiffness and Damping Parameters of a Linear Servomechanism," *Mechanics Based Design of Structures and Machines*, Vol.32, No.3, pp.283-304.

[87] Yokoyama, T., 1990, "Vibrations of a Hanging Timoshenko Beam Under Gravity," *Journal of Sound and Vibration*, Vol.141, No.2, pp.245-258.

[88] Zaeh, M.F., Oertli, T., Milberg, J., 2004, "Finite Element Modelling of Ball screw Feed Drive Systems," *Annals of the CIRP*, Vol.53, No.1, pp.289-294.

[89] Zatarain, M., Ruiz de Argandona, I., Illarramendi, A., Azpeitia, J.L., Bueno, R., 2005, "New Control Techniques Based on State Space Observers for Improving the Precision and Dynamic Behaviour of Machine Tools," *Annals of the CIRP*, Vol.54, No.1, pp.393-396.

[90] Zhou, Y., Peng, F., Chen, J., 2007, "Torsion Vibration Analysis of Lead-Screw Feed Drives with Changeable Table Position and Work-piece Mass," *Proceedings of IEEE International Conference on Mechatronics and Automation*, August 5-8, Harbin, China, pp.2194-2199.

[91] Zhou, Y., Peng, F., Chen, J., Li, B., 2008, "Adaptive Notch Filter Control for the Torsion Vibration in Lead-Screw Feed Drive System Based on Neural Network," *Proceedings of International Conference on Intelligent Robotics and Applications*, October 15-17, Wuhan, China.

# Appendix A

## Timoshenko Beam Shape Functions, Current-Frame Rotation Operators and Coefficients of MTEF Error Transfer Functions

### A.1 Timoshenko Beam Shape Functions

The shape function matrix ($\mathbf{T}_{BS\xi\text{-}BSi}$) which describes the relationship between $CS_\xi$ and the global coordinate systems ($CS_{i\text{-}1}$, $CS_i$ and $CS_{i+1}$) attached to the nodes of the ball screw is given in Eq.(3.19). The interpolation functions making up the elements of the shape function matrix are all functions of $\xi$. Their expressions are given as:

$$
\begin{aligned}
&N_{ux1} = N_{uy1} = \frac{1}{1+\Phi}\left(2\xi^3 - 3\xi^2 - \Phi\xi + (1+\Phi)\right) \\
&N_{ux2} = -N_{uy2} = \frac{L_{Elm}}{1+\Phi}\left(\xi^3 - \left(2+\frac{\Phi}{2}\right)\xi^2 + \left(1+\frac{\Phi}{2}\right)\xi\right) \\
&N_{ux3} = N_{uy3} = -\frac{1}{1+\Phi}\left(2\xi^3 - 3\xi^2 - \Phi\xi\right) \\
&N_{ux4} = -N_{uy4} = \frac{L_{Elm}}{1+\Phi}\left(\xi^3 - \left(1-\frac{\Phi}{2}\right)\xi^2 - \frac{\Phi}{2}\xi\right) \\
&N_{\theta x1} = -N_{\theta y1} = -N_{\theta x3} = N_{\theta y3} = -\frac{6}{(1+\Phi)L_{Elm}}\left(\xi^2 - \xi\right) \\
&N_{\theta x2} = N_{\theta y2} = \frac{1}{1+\Phi}\left(3\xi^2 - (4+\Phi)\xi + (1+\Phi)\right) \\
&N_{\theta x4} = N_{\theta y4} = \frac{1}{1+\Phi}\left(3\xi^2 - (2-\Phi)\xi\right) \\
&N_{z1} = N_{\theta z1} = 1-\xi; \quad N_{z2} = N_{\theta z2} = \xi; \quad \Phi = \frac{12EI_{Elm}}{k^s GA_{Elm}L_{Elm}^2}
\end{aligned}
\tag{A.1}
$$

Here $I_{Elm}$ indicates the second moment of area of the element's cross section, $A_{Elm}$ indicates the cross sectional area of the element, $E$ and $G$ respectively represent the Young's modulus and shear modulus of the element while $k_s$ is the cross section factor which takes a value of 9/10 for circular cross sections.

## A.2 Current Frame Rotation Operators

The rotation matrix operators used to perform a rotation of a specified angle $\theta$ about the $x$, $y$ and $z$ axis of a Cartesian coordinate system are respectively denoted by $\mathrm{Rot}_x(\theta)$, $\mathrm{Rot}_y(\theta)$ and $\mathrm{Rot}_z(\theta)$. Their expressions are given as:

$$\mathrm{Rot}_x(\theta) = \begin{bmatrix} 1 & 0 & 0 \\ 0 & \cos\theta & -\sin\theta \\ 0 & \sin\theta & \cos\theta \end{bmatrix}$$
$$\mathrm{Rot}_y(\theta) = \begin{bmatrix} \cos\theta & 0 & \sin\theta \\ 0 & 1 & 0 \\ -\sin\theta & 0 & \cos\theta \end{bmatrix} \qquad \text{(A.2)}$$
$$\mathrm{Rot}_z(\theta) = \begin{bmatrix} \cos\theta & -\sin\theta & 0 \\ \sin\theta & \cos\theta & 0 \\ 0 & 0 & 1 \end{bmatrix}$$

A current-frame rotation operation is one performed such that each subsequent rotation is based on the new coordinate system resulting from the preceding rotations. For instance, a rotation from a coordinate system ($CS_1$) to another coordinate system ($CS_2$) could involve a rotation of $\alpha$ about the $x$-axis of $CS_1$, then another rotation of $\beta$ about the $y$-axis of the new intermediate coordinate system resulting from the $x$-axis rotation. Then the rotation operation from $CS_1$ to $CS_2$, $\mathbf{T}_{1\text{-}2}$, can be represented by:

$$\mathbf{T}_{1-2} = \mathrm{Rot}_x(\alpha) \cdot \mathrm{Rot}_y(\beta) \qquad \text{(A.3)}$$

Generally, a rotation operation involving a sequence of current frame rotations from one coordinate system to another is performed by multiplying the respective rotation matrices in the same sequence as the rotations.

Another important fact about rotation operations is that a rotation matrix $\mathbf{T}_{1\text{-}2}$ from one coordinate system $CS_1$ to another $CS_2$ also represents a transformation matrix from $CS_2$ to $CS_1$. In order words, a vector expressed in $CS_2$ can be transformed to $CS_1$ by pre-multiplying it by $\mathbf{T}_{1\text{-}2}$.

### A.3 Coefficients of MTEF Error Transfer Functions

The full expressions of the numerator and denominator coefficients of $G_{ez}(z)$ and $G_{eF}(z)$ in Eq.(4.28) as functions of $r$ and $r^*$ are given below.

$$
\begin{aligned}
\bar{G}_1 &= 1+\sigma(1+r^*)-(a_{11}+ra_{21}+\sigma(a_{11}+r^*a_{21}+a_{12}+r^*a_{22}))T^2 \ldots \\
&\quad -(a_{13}+ra_{23}+\sigma(a_{13}+r^*a_{23}+a_{14}+r^*a_{24}))T \\
\bar{H}_1 &= (a_{13}+ra_{23}+\sigma(a_{13}+r^*a_{23}+a_{14}+r^*a_{24}))T-2(1+\sigma(1+r^*)) \\
\bar{J}_1 &= 1+\sigma(1+r^*) \\
\bar{G}_2 &= r-(a_{12}+ra_{22})T^2-(a_{14}+ra_{24})T \\
\bar{H}_2 &= (a_{14}+ra_{24})T-2r \\
\bar{J}_2 &= r \\
\bar{G}_3 &= 1+\sigma-(a_{11}+ra_{21}+\sigma(a_{11}+r^*a_{21}))T^2-(a_{13}+ra_{23}+\sigma(a_{13}+r^*a_{23}))T \\
\bar{H}_3 &= (a_{13}+ra_{23}+\sigma(a_{13}+r^*a_{23}))T-2(1+\sigma) \\
\bar{J}_3 &= 1+\sigma \\
\bar{G}_4 &= r+\sigma r^*-(a_{12}+ra_{22}+\sigma(a_{12}+r^*a_{22}))T^2-(a_{14}+ra_{24}+\sigma(a_{14}+r^*a_{24}))T \\
\bar{H}_4 &= (a_{14}+ra_{24}+\sigma(a_{14}+r^*a_{24}))T-2(r+\sigma r^*) \\
\bar{J}_4 &= r+\sigma r^* \\
\bar{L} &= (b_{11}+rb_{12}+\sigma(b_{11}+r^*b_{12})) \\
\sigma &= \frac{b_{12}+rb_{22}}{b_{12}+r^*b_{22}}
\end{aligned}
\tag{A.4}
$$

# Appendix B

## Comparison of Rigid Ball Screw and Shape Function-Based Screw-Nut Interface Models for Short and Long Nuts

### B.1 Purpose of Study

This study aims at comparing the performance of the Rigid Ball Screw and Shape Function methods presented in Chapter 3 for deriving the screw-nut interface of ball screw drives. The Rigid Ball Screw method assumes that the portion of the ball screw within the nut translates and rotates as a rigid body while the Shape Function Method considers the elastic deformations of the screw within the nut. The formulations for the Rigid Ball Screw method are much simpler than those of the Shape Function method. Therefore, it is of interest to find out:

(1) If there exists any significant difference between the predictions of the two models in terms of the natural frequency and mode shapes of the ball screw and nut assembly; and

(2) Under what circumstances these differences are likely to occur (if at all they do).

This study is entirely based on simulations and is therefore preliminary to a more detailed study including experimental validation.

### B.2 Description of Simulation Test Set-up

The set-up used for this study (Figure B.1) consists of the ball screw and nut of the test bed described in Section 3.4.1. The nut is assumed to be rigidly clamped at a position 150 [mm] from the left end of the screw while the screw is allowed to freely rotate inside the nut. The effective length of the nut ($L_{Nut}$) is considered the variable in the study. Three $L_{Nut}$ values are considered: $L_{Nut}$ = 30 [mm] (which is the length of the actual test bed's nut), $L_{Nut}$ = 60 [mm] and $L_{Nut}$ = 90 [mm].

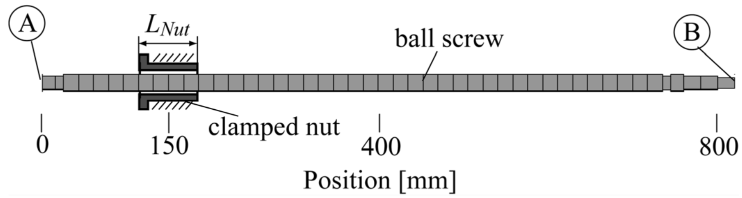


**Figure B.1: Simulation Set-up consisting of Ball Screw attached to Clamped Nut**

### B.3 Description of Simulation Test Set-up

For each $L_{Nut}$ value, three frequency response functions (FRF) are simulated:

(1) Axial FRF between an axial excitation at Point A (see Figure B.1) and axial displacement of Point B

(2) Torsional FRF between a torsional excitation at Point A and torsional displacement of Point B

(3) Lateral FRF between a lateral excitation at Point A and lateral displacement of Point B

The simulated FRFs are shown in Figures B.2, B.3 and B.4 for $L_{Nut}$ = 30 [mm], 60 [mm] and 90 [mm], respectively.

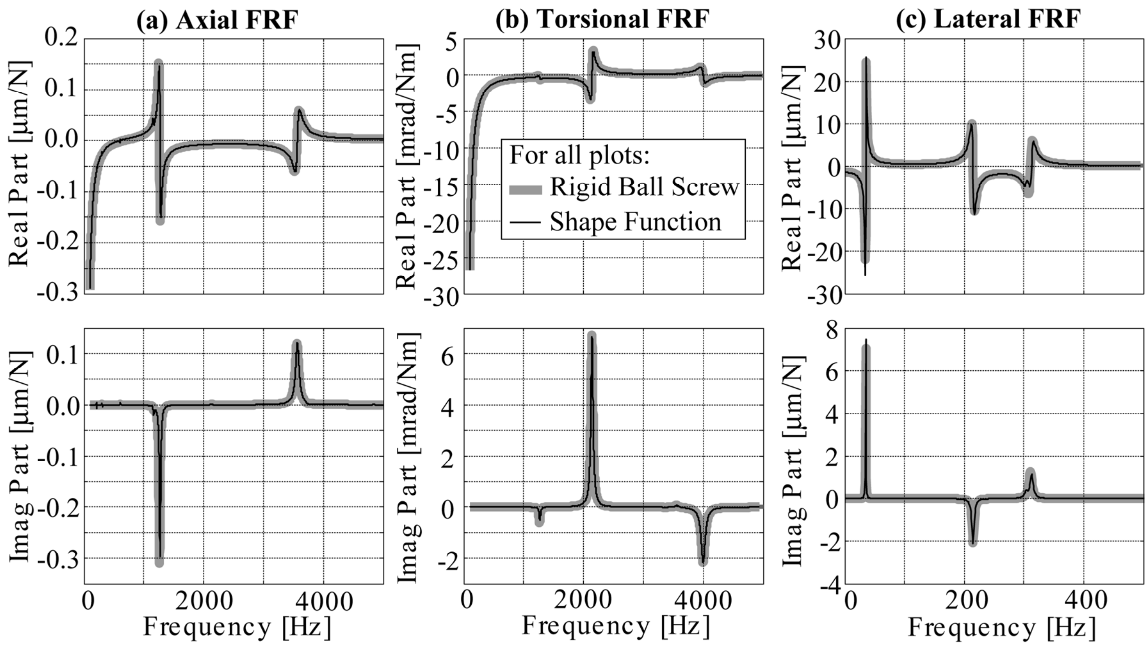


**Figure B.2: Simulated FRFs Comparing the Rigid Ball Screw and Shape Function Methods for $L_{Nut}$ =30 [mm]**

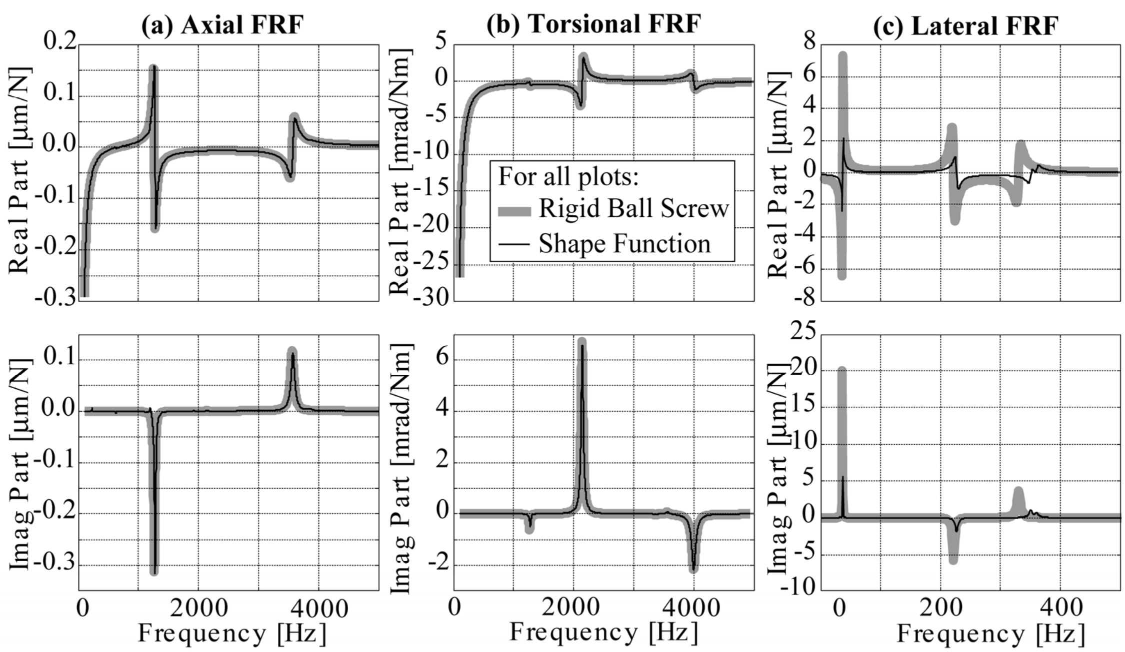


**Figure B.3: Simulated FRFs Comparing the Rigid Ball Screw and Shape Function Methods for $L_{Nut}$ =60 [mm]**

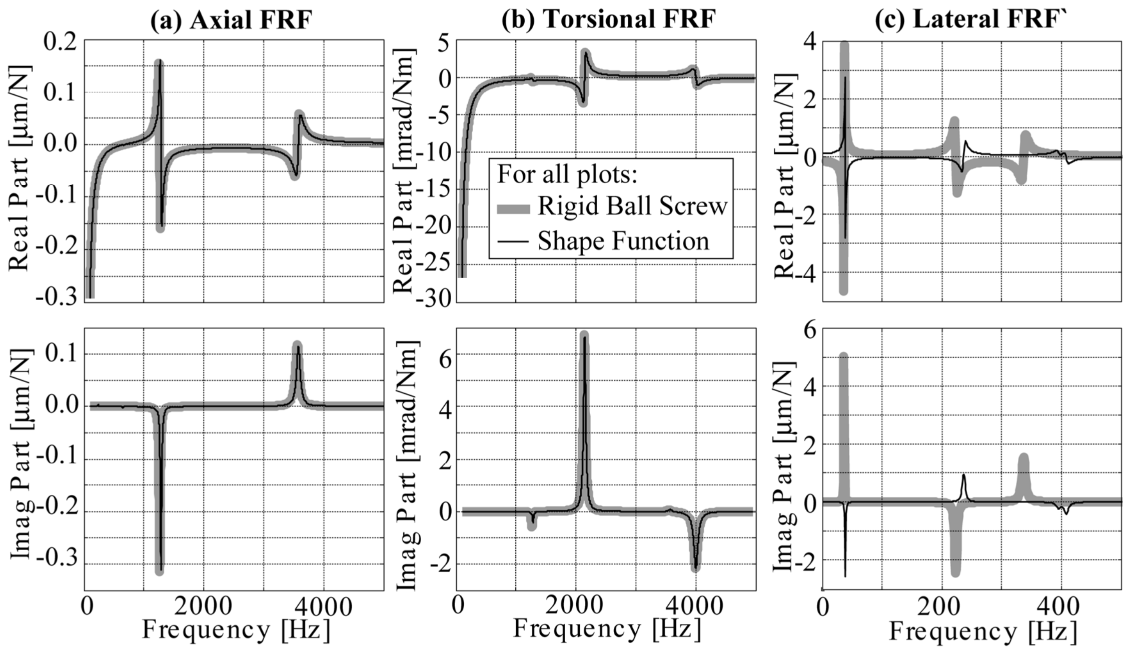


**Figure B.4: Simulated FRFs Comparing the Rigid Ball Screw and Shape Function Methods for $L_{Nut}$ =90 [mm]**

From the figures it is observed that the two methods give very similar results for both axial and torsional modes irrespective of the length of the nut. When the $L_{Nut}$ = 30 [mm], their predicted lateral FRFs are also very similar. However, as the length of the nut increases, significant mismatches in both natural frequency and mode shape (as deduced from the FRF amplitude) begin to occur. For instance, when $L_{Nut}$ = 90 [mm], there is a difference of about 70 [Hz] (i.e. 18 [%]) in the prediction of third lateral mode occurring around 400 [Hz]. Furthermore, the modes in the lateral FRF predicted by the two methods are out of phase with each other.

Intuitively, the observations made in from the simulated FRFs make a lot of sense. The length of the nut is not likely to affect the axial and torsional modes because it does not impose a lot of constraint in the axial and torsional directions. Furthermore, the axial and torsional modes of the screw are usually much stiffer than the lateral modes. This means that there is less likelihood of any significant elastic deformation within the nut in those directions. However, length of the nut tends to pose a great deal of constraint on the rotation of the screw about the lateral axes. This in turn leads to higher natural frequencies and stiffer modes.

The effect of the constraint imposed by the longer nuts can be better understood by studying the shapes of the screw for the three modes appearing in the simulated lateral FRFs. As seen from the composite plot of Figure B.5, when $L_{Nut}$ = 30 [mm], the mode shapes generated by the two methods are almost identical. However, as $L_{Nut}$ increases, the mode shapes from the two models begin to differ. The Shape Function method imposes greater constraints on the rotation of the screw around the point of attachment of the nut. This is the reason for the large discrepancies observed in the lateral FRFs for $L_{Nut}$ = 60 [mm] and 90 [mm].

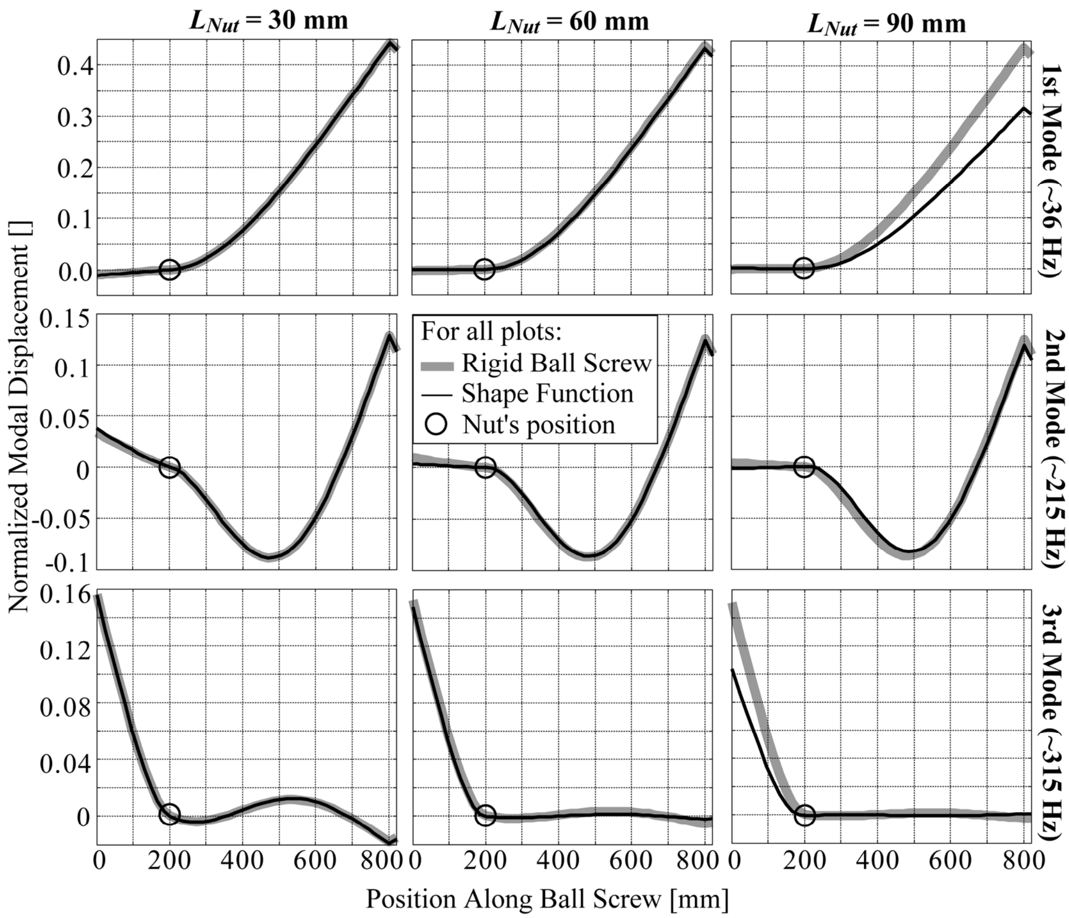


**Figure B.5: Simulated Shapes of Ball Screw for the Three Modes Observed in the Simulated Lateral FRFs**

### B.4 Conclusion of Study

This short study has helped to show, through simulations, that there is no significant difference between the Rigid Ball Screw and Shape Function methods for modes occurring in the axial and torsional directions, irrespective of the length of nut. However, in the lateral direction, significant differences in natural frequency and mode shapes begin to arise between the predictions of the two models as the length of the nut increases. This is as a result of the stricter constraint imposed by the nut on the screw in the Shape Function method compared with the Rigid Ball Screw method. Experiments have not been conducted to ascertain which of the methods is more accurate for longer nuts but based on sheer intuition, the predictions of the Shape Function method seem to be more realistic. A more detailed study involving experiments is needed to confirm this hypothesis. One conclusion that can however be made from this study is that the two methods give almost identical results for short nuts. Therefore, the simpler of the two methods (i.e. the Rigid Ball Screw method) is better for use with short nuts, as in the case of the test bed of Chapter 3.